UNIVERSITY OF OKLAHOMA

GRADUATE COLLEGE

IMPROVING THE THERMAL CONDUCTIVITY OF NANOTUBE COMPOSITES VIA END FUNCTIONALIZATON: RANDOM WALKS AND MOLECULAR DYNAMICS

A THESIS

SUBMITTED TO THE GRADUATE FACULTY

in partial fulfillment of the requirements for the

Degree of

MASTER OF SCIENCE

By

TIMOTHY ALEXANDER BURT
Norman, Oklahoma
2017

IMPROVING THE THERMAL CONDUCTIVITY OF NANOTUBE COMPOSITES VIA END FUNCTIONALIZATON: RANDOM WALKS AND MOLECULAR DYNAMICS

A THESIS APPROVED FOR THE
DEPARTMENT OF ENGINEERING PHYSICS

BY

_____
Dr. Kieran Mullen, Chair

_____
Dr. Daniel Glatzhofer

_____
Dr. Bin Wang

I would like to dedicate this thesis to my mother, who has always been there for me.

Acknowledgements

First I would like to thank my mother for her inspirational (& financial) support while finishing my degree. I would also like to thank my advisor, Dr. Mullen, for all his advice & support, as well as Alex Kerr for his assistance when I have problems with code, research questions, and anything else I've bombarded him with over email. Lastly I would like to thank Dr. Glatzhofer's group, notably Matthew Houck, for their experimental work & results. These last few years while working on my Master's degree have been very challenging & stressful for me, and so I'd like to thank friends & family who've I've relied on for support as well.

Table of Contents

List of Figures

Abstract

The high thermal conductivity of carbon nanotubes (CNTs) has promise for improving the thermal conductivity of nano composites. However, their large Kapitza resistance has frustrated this effect. One solution is to functionalize the ends of the CNT matching their vibration spectrum better to the surrounding medium. In this thesis we simulate cases in which the CNT ends are either well coupled or not well coupled to the surrounding medium. Our findings indicate a notable improvement of the thermal conductivity of functionalized CNTs versus pristine CNTs. The effects of excluded volume or sterics on the thermal conductivity is also examined. The necessary mathematics and physics are given along the way, as well as intuitive examples to make the concepts easier to understand. A random walk method is used to calculate the thermal conductivity of end-functionalized CNT composite materials, as well as molecular dynamics (MD) simulations that do the same.

Chapter 1: Introduction

1.1 The problem of interfacial (Kapitza) resistance

Thermal conductivity is an important property of materials. Materials with a high thermal conductivity[1] such as metals allow heat to flow easily, while ones with a low thermal conductivity such as ceramics like AlN are resistant to heat flow. Thus depending on what the material is used for, high thermal conductivity is desired for objects like heatsinks while low thermal conductivity is desired for fire-resistant heatshields. Thermal conductivity and thermal resistance are inversely related just as their electrical counterparts.

It is obvious to ask what is responsible for the transfer of heat in solids. Solids may be crystalline, amorphous, or random with respect to the arrangement of their atoms [1]. Order and disorder describe the presence or lack of symmetries or correlations in a many-atom system. If atoms repeat themselves and are translationally invariant in space (crystalline), we say the material has long-range order.

This long-range order allows for wave-like excitations to travel freely. These waves might be the motion of electrons in conductors or vibrations of the lattice in conductors or insulators. Such lattice waves are called “phonons”.

Electrons and phonons can still be used to discuss transport in disordered systems such as plastics. However in disordered systems waves are localized & transport is hindered. It is tempting therefore incorporate a periodic material such as

[1] Has units of W/(m*K) in SI and is generally denoted by the letter k

carbon nanotubes to form a composite.

Carbon nanotubes, or CNTs, were first investigated for their unusual yet useful properties after the discovery of fullerenes (C_{60} or "buckyballs") in 1985 at Rice University by Smalley, Curl, and Kroto. However, there is reason to believe materials like CNTs have existed in nature long before their discovery by scientists [2]. CNTs and other allotropes of carbon appear in small quantities in materials such as soot and charcoal, so Neanderthals likely generated them with their fires. Sumio Iijima is generally credited with the discovery in 1991, categorizing their crystal structure. Their interesting properties include excellent thermal conductivity, strength, and hardness as well as being lightweight. They are in the early stages of being used in consumer products, and their use in electrical and optical devices is an active area of interdisciplinary research, including in solid state devices (SSDs). Their thermal conductivity has been measured to be between 1750-6000 W/(mK) for single-walled carbon nanotubes (SWCNTs) at room temperature [3], and around 3000 W/(mK) for multi-walled carbon nanotubes (MWCNTs) [4].

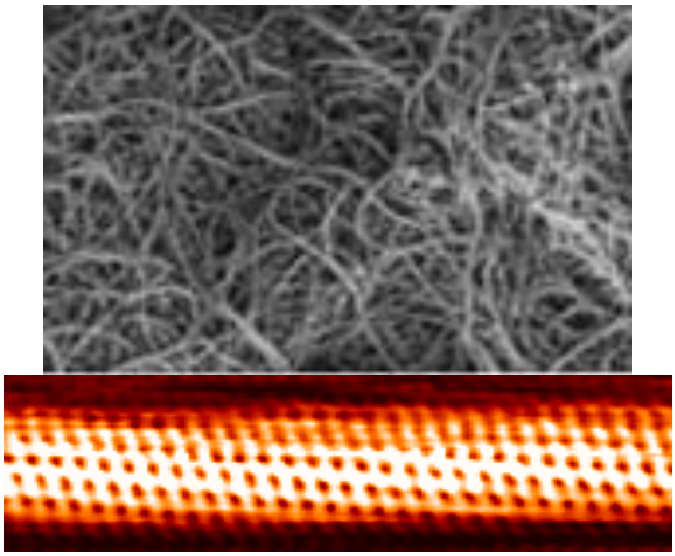

Figure 1: Above - Scanning electron microscopy image of purified SWCNTs [5]**. Below - Scanning tunneling microscopy image of a single-walled carbon nanotube** [6]**.**

Interfacial thermal resistance was first discovered in 1941 by P.L. Kapitza in his study of heat transfer & the super fluidity of Helium II [7]. To this day, Kapitza resistance is still not well understood, with differences between models as large as an order of magnitude in some cases. A diagram depicting the effect is given in Figure 2.

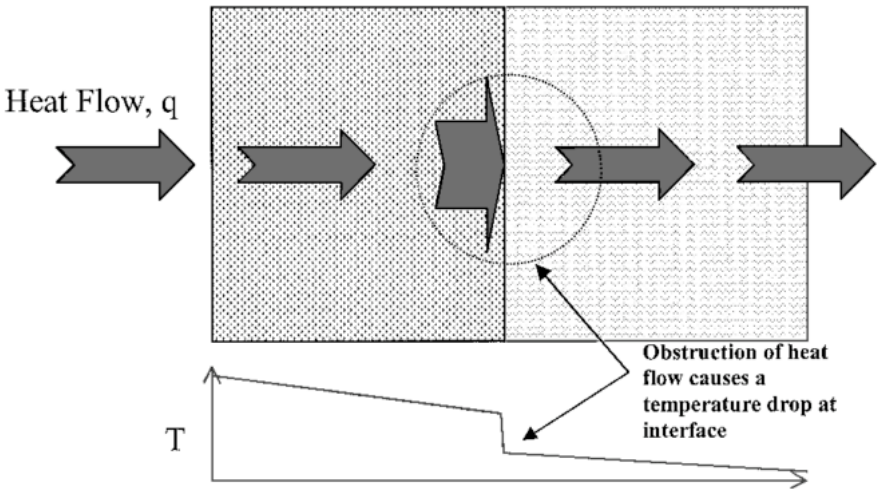

Figure 2: Kapitza (thermal boundary resistance) between two materials [8]**.**

Although Kapitza resistance has historically referred to solid-liquid helium interfaces, and interfacial or thermal boundary resistance is the general term, I use both interchangeably as my research does not concern liquid helium interfaces.

1.2 Thermal applications of carbon nanotubes

Since 1965, Moore's Law has predicted the dimensions of integrated circuit (IC) components will decrease by a factor of two approximately every two years [9]. However, entering the sub-22 nm dimension as mainstream IC manufacturers have around 2009 has posed serious problems and challenges, from device fabrication to heat dissipation.

Quantum effects including limits on tunneling become more and more important to consider as well as materials that are better suited to work in this regime. CNTs can overcome many of these problems, including device defects, passive power dissipation, current leakage and heat transport. For CNTS, chirality (n,m) and diameter can be precisely controlled. Also, since they are known as quasi-1D materials, consisting of graphene sheets, only forward and back scattering in those sheets is allowed [9], making the mean free path for elastic scattering much greater than the tube length (on the order of μm). This gives rise to ballistic transport within the tube, where the resistivity is then negligible. Chemically, covalent C-C bonds make the CNTs inert and able to carry large amounts of electrical current for their size. The same argument applies for phonons as well, and therefore they are able to carry large amounts of heat for their size. They can theoretically conduct the same amount of heat as diamonds. These are all excellent reasons why CNT thermal research should be pursued.

CNT composites made with materials like epoxy or PMMA can be used in conjunction with these devices to transport heat away from them in a certain direction as the material has an anisotropic thermal conductivity k. These materials could be lighter and cheaper than conventional heatsink materials. This is formally called thermal interface material (TIM). TIM is any material that is applied between two devices to increase their thermal coupling [10].

Coating or covering IC components that generate a high amount of heat with a heatsink is critical. This may be a metal or CNT polymer radiator-type object or even letting them sit in a container of oil such as running a motherboard in a case of oil in computer overclocking competitions. The feasibility of CNT-containing materials that perform well has been demonstrated many times with many technologies, from fused deposition modeling (FDM, or a common "3D printer") to stereo lithography (SLA) and digital light processing (DLP) technologies, which pull an object out of a resin bath. These printable plastics may be printed or bonded directly to ICs, even along the leads of a circuit board. However solid materials containing CNTs will need to have another TIM between the IC and material, to reduce Kapitza resistance. Figure 3 gives us an example of using CNT-infused plastics with a 3D printer allowing complicated structures to be printed.

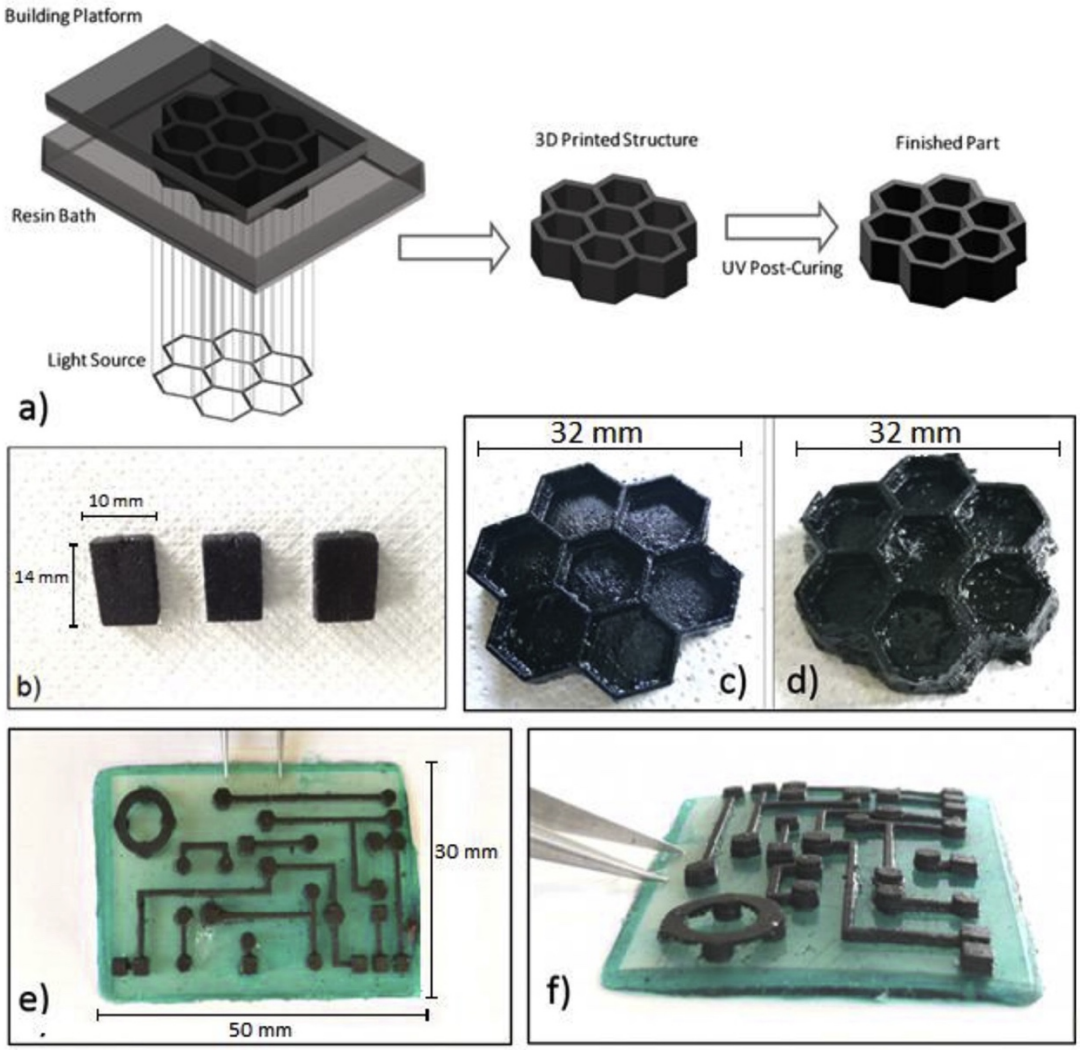

Figure 3: a) DLP 3D printing process for material. b) 3D printed cubes containing 0.3% wt CNTs. c) 3D hexagonal or honeycomb structure. e,f) Circuit-like structure built on an insulating base [11]**.**

If TIM is not present between two solid and smooth interfacing surfaces, roughness can limit actual surface contact to around 1-2% due to air gaps and the low thermal conductivity of air. The total thermal resistance to thermal interface material insertion (θ_{TM}) can be written as [10]

$$\theta_{TIM} = \frac{BLT}{k_{TIM}} + \theta_{c1} + \theta_{c2} \qquad (1)$$

with BLT the bond line thickness, k_{BLT} the thermal conductivity, and θ_{c1} and θ_{c2} represent the thermal resistances of each bonding surface with the TIM.

One might expect that adding pristine, or plain CNTs to an epoxy or paste would increase the thermal conductivity simply because of the magnitude of the CNT's thermal conductivity; however this turns out to not be the case. At the nanoscale, interface quality and thermal excitations or phonons are the determining factors for the material's bulk thermal conductivity, and Kapitza resistance is high at an interface where the speed of sound changes. Chen [12] showed this experimentally in 2013, noting that thermal impedance sharply increases for silicon grease containing pristine CNTs as the weight fraction increases, yet decreases for the grease containing CNTs functionalized (or doped) with COOH (carboxylic acid) (Figure 4).

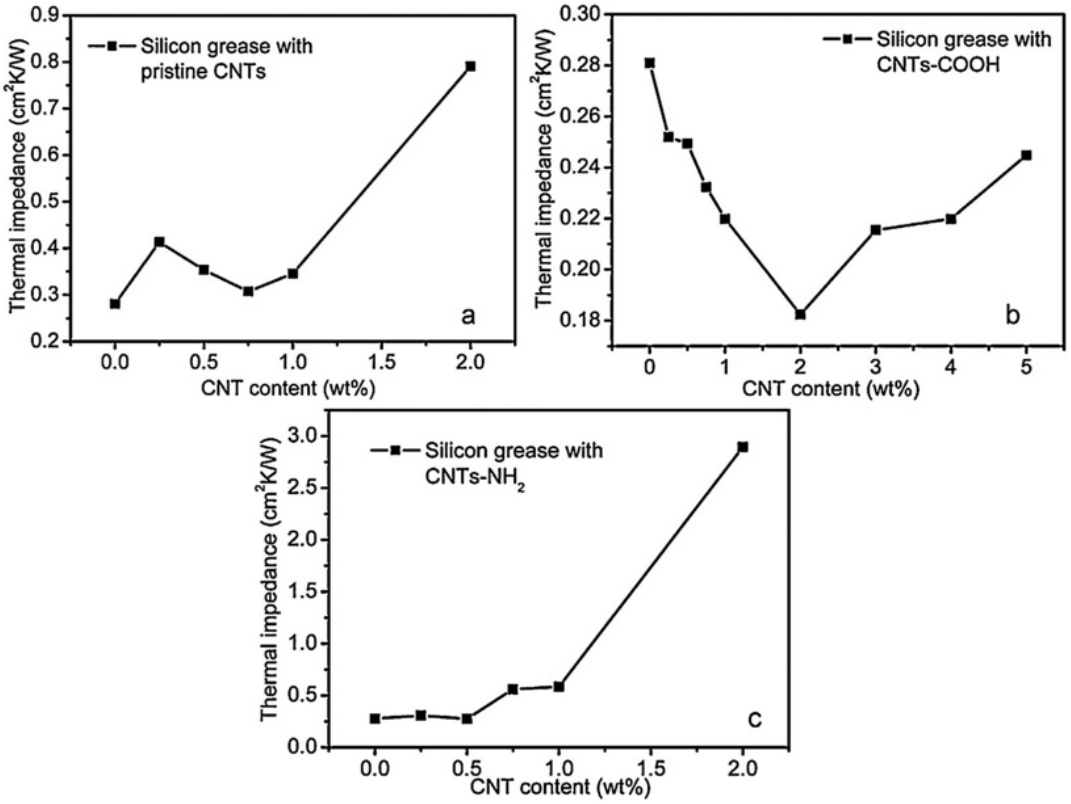

Figure 4: The thermal impedance of silicon grease with pristine CNTs and CNTs doped with carboxylic acid or an amino group [12]**.**

The primary goal of this thesis is to explain theories behind micro/nanoscale heat transport and to present research attempting to improve the thermal conductivity of CNT composites by running simulations based on nanoscale heat transport theory and then compare them to experimental results. Throughout this thesis I denote vectors in **bold** typeset or as $\vec{}$ or $\vec{}$.

The roadmap for the rest of this thesis will be as follows. In Chapter 2: Theory of heat transport I discuss heat transport theory in general. In Chapter 3: Phonon transport theory/Kapitza resistance models I discuss more specifically theories of Kapitza resistance and phonon scattering models. In Chapter 4: Random Walks I discuss random walks and their usefulness in my research, along with the results from

my simulations on end-functionalized nanotube composites using a random walk method on a lattice. In Chapter 5: Molecular Dynamics I connect with research from another graduate student in our group, Alex Kerr, who has written a package to calculate thermal conductivities of these composites with a Green's function method derived in our lab. I simulate these composites with a more exact method using molecular dynamics (MD) *in vacuo.* I also briefly outline the usefulness and mathematics of MD simulations. I conclude with a summary and what's next/unresolved in my research.

Chapter 2: Theory of heat transport

2.1 The Boltzmann transport equation

While complicated heat transport models have been extensively developed, each can be derived (in principle) from the limiting cases of the Boltzmann Transport equation, a nonlinear integro-differential equation governing a non-equilibrium statistical mechanical system derived by Boltzmann in 1872 [13]. This equation is important for understanding the basis for how phonons, or heat excitations, propagate in a material. Let me first present Liouville's equation (equation **(** 1)) as some consider this to be the fundamental non-equilibrium statistical mechanics equation [14].

$$\frac{\partial F_N}{\partial t} + \sum_{i=1}^{N} \left(\frac{\partial F_N}{\partial \boldsymbol{p_i}} \cdot \dot{\boldsymbol{p}}_i + \frac{\partial F_N}{\partial \boldsymbol{q_i}} \cdot \dot{\boldsymbol{q}}_i \right) = 0 \qquad \textbf{(1)}$$

This can be derived from Hamilton's canonical equations, dividing phase space up into volume elements, and assuming the ergodic hypothesis (an ensemble average is equal to the time average of some macroscopic property). We have that F_N is the normalized probability density function (denoting the chance at a certain position, momentum, and time of phase space being occupied by a particle), **p** is the particle's

momentum and **q** is the particle's position, for N particles in the system.

The ensemble average of some macroscopic property G can be written as

$$< G(t) > = \int \prod_{i=1}^{N} d\boldsymbol{q_i} d\boldsymbol{p_i} G(\{\boldsymbol{q}\},\{\boldsymbol{p}\}) F_N(\{\boldsymbol{q}\},\{\boldsymbol{p}\},t) \qquad \textbf{(2)}$$

and (2) can be rewritten in terms of forces using the fact that $\boldsymbol{f_i} = \dot{\boldsymbol{p}}_i$ and

$\boldsymbol{p_i}/_m = \dot{\boldsymbol{q}}_{\boldsymbol{i}}$, where $\mathbf{f_i}$ is the net force acting on particle i. It would be too difficult to obtain these quantities for every atom in a macroscopic system, but by making some assumptions we can obtain a more tractable equation to describe the system. By assuming the net force is derivable from a pairwise potential (a function of $|\boldsymbol{q_i} - \boldsymbol{q_j}|$),

$$\boldsymbol{f_i} = -\sum_{j=1\neq i}^{N} \frac{\partial \Phi_{ij}}{\partial \boldsymbol{q_i}} \qquad \textbf{(3)}$$

we can reduce the degrees of freedom in the system and write an equation for F_R, the reduced normalized probability density function.

$$\frac{\partial F_R}{\partial t} + \sum_{i=1}^{R} \frac{\boldsymbol{p_i}}{m} \cdot \frac{\partial F_R}{\partial \boldsymbol{q_i}} - \sum_{i,j=1} \frac{\partial \Phi_{ij}}{\partial \boldsymbol{q_i}} \cdot \frac{\partial F_R}{\partial \boldsymbol{p_i}} = (N - R) \int d\boldsymbol{x_{R+1}} \sum_{i=1}^{R} \frac{\partial \Phi_{iR+1}}{\partial \boldsymbol{q_i}} \cdot \frac{\partial F_{R+1}}{\partial \boldsymbol{p_i}} \qquad \textbf{(4)}$$

Equation (4) is known as the BBGKY hierarchy of equations [14], named after Bogoliubov, Born, H. S. Green, Kirkwood, and Yvon, who each derived it independently. We see that this equation is not closed, and further work must be done to obtain one equation which is not coupled to the others (the Boltzmann equation).

Writing out the first two hierarchy equations explicitly, we get

$$\frac{\partial F_1}{\partial t} + \frac{\boldsymbol{p_1}}{m} \cdot \frac{\partial F_1}{\partial \boldsymbol{q_1}} = (N-1) \int d\boldsymbol{x_2} \boldsymbol{\Phi'_{12}} \cdot \frac{\partial F_2}{\partial \boldsymbol{p_1}} \qquad \textbf{(5)}$$

$$\begin{aligned} &\frac{\partial F_2}{\partial t} + \frac{\boldsymbol{p_1}}{m} \cdot \frac{\partial F_2}{\partial \boldsymbol{q_1}} + \frac{\boldsymbol{p_2}}{m} \cdot \frac{\partial F_2}{\partial \boldsymbol{q_2}} - \Phi'_{12} \cdot \left(\frac{\partial}{\partial \boldsymbol{p_1}} - \frac{\partial}{\partial \boldsymbol{p_2}} \right) F_2 \\ &= (N-2) \int d\boldsymbol{x_3} \left\{ \boldsymbol{\Phi'_{13}} \cdot \left(\frac{\partial}{\partial \boldsymbol{p_1}} - \frac{\partial}{\partial \boldsymbol{p_2}} \right) + \boldsymbol{\Phi'_{23}} \cdot \left(\frac{\partial}{\partial \boldsymbol{p_2}} - \frac{\partial}{\partial \boldsymbol{p_3}} \right) \right\} \end{aligned} \qquad \textbf{(6)}$$

The applicability of equation (5) relies on three properties of the system (which are doubtful in solids): the density is low enough so that binary collisions only must be considered, the spatial dependence of the gas properties is slow enough that collisions are “local” in space, and the inter particle potential has a short enough range that the first statement is true. This is the Boltzmann gas limit (BGL). Mathematically it corresponds to the following limits:

$$\begin{gathered} N \to \infty \\ m \to 0 \\ \sigma \to 0 \\ N\sigma^2 = constant \\ Nm = constant \end{gathered} \qquad \textbf{(7)}$$

where N is the number of particles in the system, m is the mass of each particle, and σ is a term that defines the range of the inter particle forces.

Taking a step backward, equation (8) is simply a force balance for the net force

on each particle f_i, and $\mathbf{F}(\mathbf{r},t)$ represents the force field which acts on the particles.

$$\frac{\partial f_i}{\partial t} + \mathbf{F} \cdot \frac{\partial \mathrm{f_i}}{\partial \mathbf{p_i}} = \left(\frac{\partial \mathrm{f_i}}{\partial \mathrm{t}}\right)_{\mathrm{coll}} \qquad (8)$$

The left term accounts for the external forces (no mass transport for the case of phonons), and the right term accounts for the collision effects. If we set the collision term equal to 0 the equation becomes the Vlasov equation.

Boltzmann derived a form for the collision term assuming two-body collisions to be uncorrelated (the "*Stosszahlansantz"*), giving us the expression

$$\left(\frac{\partial f_i}{\partial t}\right)_{coll} = \sum_{j=1}^{N} \iint g_{ij} I_{ij}(g_{ij}, \Omega) \left| f_i' f_j' - f_i f_j \right| d\Omega d^3 \boldsymbol{p}' \qquad (9)$$

with $f' = f'(\boldsymbol{p_i'}, t)$ and the relative momenta magnitude given by

$$\boldsymbol{g_{ij}} = \left|\boldsymbol{p}_i - \boldsymbol{p}_j\right| = \left|\boldsymbol{p'}_i - \boldsymbol{p'}_j\right| \qquad (10)$$

and I_{ij} is the differential cross section.

Replacing the right hand side of equation (8) with equation (9), and rewriting in a similar form gives [14]

$$\frac{\partial f}{\partial t} + \mathbf{v_1} \cdot \frac{\partial \mathrm{f}}{\partial \mathbf{q_1}} = \frac{1}{m} \int d\omega d\boldsymbol{v_2}\, V[f(\boldsymbol{q_1}, \overline{v_1}, t) f(\boldsymbol{q_1}, \overline{v_2}, t) - f(\boldsymbol{q_1}, \boldsymbol{v_1}, t) f(\boldsymbol{q_1}, \boldsymbol{v_2}, t)] \qquad (11)$$

The one and two indices are the respective quantities assuming only two particles, 1 and 2. The barred velocities indicate the initial velocities of the particles before the collision occurs. Error of the collision term is of order σ, the distance between the two particles

and f is the force on particle 1.

Equation (8) (or equation (11)) is the Boltzmann equation. In general it is a set of N coupled nonlinear integro-differential equations for N particles in the system and described as a "beast" by some authors [14]. It is the fundamental equation for non-equilibrium thermodynamics and Fourier's Law as well as other fundamental fluid mechanics formulas can be derived from it.

Most solutions to this equation involve a linearization procedure, and they are known as Hilbert-type solutions. These solutions reside in Hilbert space and so have simplifying properties, and by introducing the quantity where the linear operator would be,

$$\delta = \lambda \mathfrak{Q}^{-1} \equiv K_n \qquad \textbf{(12)}$$

we can see that where the system behaves as a continuum, δ, is small. This term K is called the Knudsen number and these linear solutions are only valid for systems with small Knudsen numbers.

Chapman & Enskog independently derived solutions more general than Hilbert, and these solutions allow transport coefficients to be computed, such as the thermal conductivity and the viscosity. Macroscopic equations such as the Navier-Stokes equation cannot tell us those in this regime due to the continuum hypothesis. Grad developed a solution in terms of Hermite tensor polynomials, assuming the particles are

Maxwell particles, or hard-sphere scattering. Specific solutions also exist, such as for the plane Poiseuille flow problem in fluid mechanics. I will leave the Boltzmann equation discussion where it is for now and continue discussing interfacial resistance in general.

While this framework was developed for atoms & molecules, we can also use it to describe the probability distribution of phonons, treating these excitations as the particles in our system. The collision term represents phonon-phonon scattering due to anharmonicity as well as phonon impurity scattering.

Regardless of the model, a mismatch of material properties is responsible for interfacial resistance, specifically the differences between the speed of sound v_D and the specific heat C_V between two materials. Starting with Fourier's Law of Heat Conduction, we have $q = -\overleftrightarrow{k}\nabla T$, where in general k is a tensor of rank two. If we assume there is a constant heat flux q across this interface, we have

$$q = {}^{\Delta T}/_{R} \qquad \textbf{(13)}$$

with ΔT the temperature difference across the interface and R the Kapitza resistance. Some of the heat carriers will scatter and some will pass, depending on R. This is important to understand because of how important heat dissipation is at the nanoscale level. If we can control R, we can design metamaterials with properties better than Nature has given us.

Also relevant is the concept of heat diffusivity[2], which tells us if an object is

[2] SI units of m^2/s

"cold to the touch" [15]. It is given by

$$\alpha = k/\rho c_P, \frac{\partial T}{\partial t} = \alpha \Delta T \quad \textbf{(14)}$$

with k the thermal conductivity, ρ the density of the material and c_P its specific heat. I show the heat equation alongside it to show how it simplifies the expression.

CNTs are essentially rolled up sheets of graphene, a 2D sheet of carbon in a honeycomb structure [16]. The way the sheets are rolled determine their lattice structure. The common way to do this is with indices (n,m), where n & m are the two unit vectors of graphene, detailing how many unit vectors to step in each direction during the rollup. These two unit vectors together are called the lattice, or chiral vector. Names given to these indices are zigzag (n,0), armchair (n,n), and chiral (n,m). These are referred to as single-walled CNTs, and have typical diameters of 1-10 nm and lengths of several micrometers, making large L/d ratios possible. Their thermal conductivity has been found to be approximately 3000 W/mK for isolated multi-walled CNTs (MWCNTs) and between 1750 and 6600 W/mK for single-walled CNTs (SWCNTs) at room temperature [17][18][3].

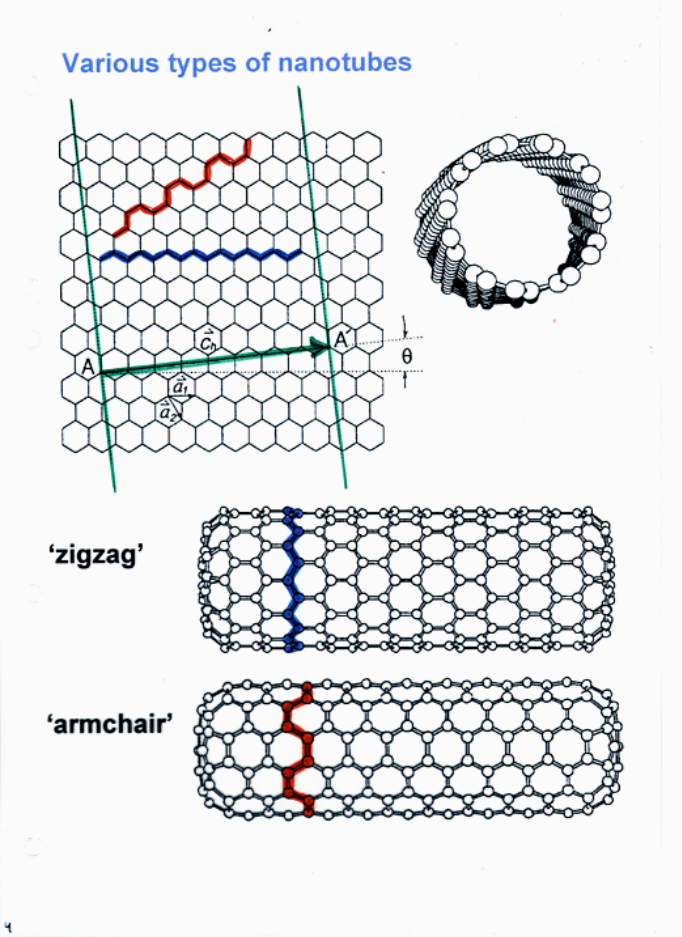

Figure 5: Rolling the carbon nanotube in the direction of the unit vector (a,b,c) determines the type and properties of the CNT [19]**.**

Electrically, CNTs can act as either metallic or semiconducting depending on how they are rolled. A third of all possible single-walled carbon nanotubes (SWCNTs) are metallic, where the electronic density of states (DOS) is not zero at the Fermi energy, and two-thirds are semiconducting with zero DOS at the Fermi energy [20]. Multi-walled carbon nanotubes (MWCNTs) are also possible and usually are comprised of alternating metallic and semiconducting SWCNTs of different radii.

n = m implies a metallic tube, (n-m)mod(3) = 0 a small bandgap semiconductor, and any other possibility is a moderate semiconductor. In either case, the CNT acts as a p-type semiconductor when undoped. The diameter of the tube affects the bandgap,

which is direct. CNTs also have many interesting optical properties, but most of these will not be discussed to focus on semiconductor-based devices instead of optoelectronic devices.

2.2 Tight binding model

There are two common models for understanding CNT lattice dynamics, a force-constant approach where a Hamiltonian is constructed using the adiabatic approximation, or a tight-binding approach directly from the Schrödinger equation. The important thing they both depend on is the screw symmetry in CNTs. This includes three types of symmetry: translational, helical, and rotational. These symmetries translate into reciprocal space in the Brillouin zone. Since SWCNTs are graphene sheets rolled into a cylinder, high symmetry points for the graphene lattice translate to CNTs.

For instance, the tight-binding approximation considers the wave function as a Linear Combination of Atomic Orbitals (LCAO) [21]. The electron energy in a solid can be estimated from Schrödinger's equation

$$\left[-\frac{\hbar}{2m}\nabla^2 + V(\boldsymbol{r})\right]\psi_k(\boldsymbol{r}) = E\psi_k(\boldsymbol{r}) \qquad \textbf{(15)}$$

Symmetry gives us the condition

$$u_{\boldsymbol{k}}(\boldsymbol{r})e^{i\boldsymbol{k}\cdot(\boldsymbol{r})} = u_k(\boldsymbol{r})e^{i\boldsymbol{k}\cdot(\boldsymbol{r}+\boldsymbol{C})} \qquad \textbf{(16)}$$

where u_k is a periodic function defined by the crystal lattice, and **C** is the lattice vector. Solutions to the Schrödinger equation in this model must be of the form shown in equation (16). Then $\boldsymbol{k}\cdot\boldsymbol{C} = 2\pi l$, with **k** the wave vector and l an arbitrary integer. This is a boundary condition known as the "Born-von Karman" condition, which states the Brillouin zone is quantized.

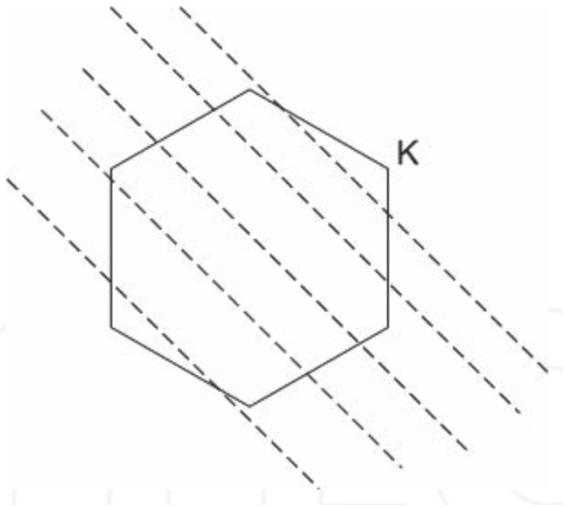

Figure 6: High symmetry in graphene quantizes the Brillouin zone of CNTs in the tight-binding model due to the "Born-von Karman" condition [21]**.**

By "tight-binding" or considering only nearest neighbor interactions (π-TB), we can solve for the band structure of the CNT.

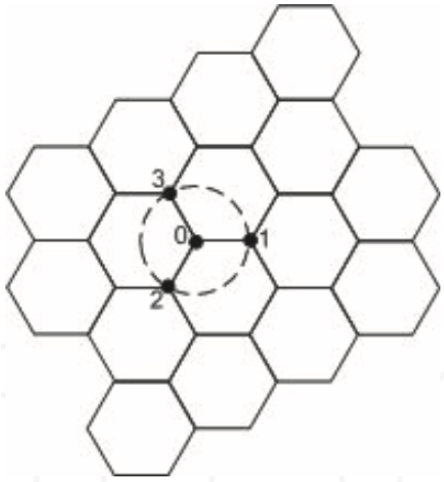

Figure 7: Only the atomic orbitals of an atom's nearest neighbors are considered in the π tight-binding model [21]**.**

ψ_k is written as $\psi_k(\boldsymbol{r}) = \sum_r c_{kr}\varphi_{kr}(\boldsymbol{r})$, with the φ_{kr}'s acting as basis functions of the atomic orbitals

$$\varphi_{kr}(\boldsymbol{r}) = \frac{1}{\sqrt{N_t}} \sum_{unit\ cells} e^{i\boldsymbol{k}\cdot\boldsymbol{R}} \chi_r(\boldsymbol{R} - \boldsymbol{r}) \quad \textbf{(17)}$$

and N_t is the total number of unit cells in this system. Only the $2p_z$ orbitals of the carbon atoms are considered since they dominate the structure of the energy states. With $|\psi\rangle = c_1|\psi_1\rangle + c_2|\psi_2\rangle$,

$$H|\psi\rangle = c_1 H|\varphi_1\rangle + c_2 H|\varphi_2\rangle = c_1 E|\varphi_1\rangle + c_2 E|\varphi_2\rangle \quad \textbf{(18)}$$

$$c_1\langle\varphi_1|H|\varphi_1\rangle + c_2\langle\varphi_1|H|\varphi_2\rangle = c_1 E\langle\varphi_1|\varphi_1\rangle + c_2 E\langle\varphi_1|\varphi_2\rangle \quad \textbf{(19)}$$

$$c_1\langle\varphi_2|H|\varphi_1\rangle + c_2\langle\varphi_2|H|\varphi_2\rangle = c_1 E\langle\varphi_2|\varphi_1\rangle + c_2 E\langle\varphi_2|\varphi_2\rangle \quad \textbf{(20)}$$

To simplify, we can define

$$H_{AA} = \langle\varphi_1|H|\varphi_1\rangle, H_{AB} = \langle\varphi_1|H|\varphi_2\rangle, S_{AA} = \langle\varphi_1|\varphi_1\rangle, S_{AB} = \langle\varphi_1|\varphi_2\rangle \quad \textbf{(21)}$$

Then equation (21) becomes

$$c_1(H_{AA} - ES_{AA}) + c_2(H_{AB} - ES_{AB}) = 0 \quad \textbf{(22)}$$

with

$$|\boldsymbol{\varphi_1}\rangle = \frac{1}{\sqrt{N_t}} \sum_{lattice\ site\ A} e^{i\boldsymbol{k}\cdot\boldsymbol{R_A}} \chi_r(\boldsymbol{r} - \boldsymbol{R_A}) \quad \textbf{(23)}$$

$$|\boldsymbol{\varphi_2}\rangle = \frac{1}{\sqrt{N_t}} \sum_{lattice\ site\ B} e^{i\boldsymbol{k}\cdot\boldsymbol{R_B}} \chi_r(\boldsymbol{r} - \boldsymbol{R_B}) \quad \textbf{(24)}$$

By substituting equations (23) & (24) into equation (22), the equation reduces using the properties of Hilbert space and the linearity of exponentials. This gives us

$$c_1(H_{AB}^* - ES_{AB}^*) + c_2(H_{AA} - ES_{AA}) = 0 \quad \textbf{(25)}$$

Then a non-trivial solution exists for c_1 and c_2; in the form of a determinant

$$\begin{vmatrix} H_{AA} - ES_{AA} & H_{AB} - ES_{AB} \\ H_{AB}^{*} - ES_{AB}^{*} & H_{AA} - ES_{AA} \end{vmatrix} = 0 \quad \textbf{(26)}$$

Solving for E, we get

$$E(\boldsymbol{k})^{\pm} = \frac{-(-2E_0+E_1)\pm\sqrt{(-2E_0+E_1)^2-4E_2E_3}}{2E_3} \quad \textbf{(27)}$$

with

$$E_0 = H_{AA}S_{AA},\ E_1 = S_{AB}H_{AB}^{*} + H_{AB}S_{AB}^{*},\ E_2 = H_{AA}^2 - H_{AB}H_{AB}^{*},\ E_3 = S_{AA}^2 - S_{AB}S_{AB}^{*} \quad \textbf{(28)}$$

If we neglect any overlap of the $2p_z$ orbitals with their neighbors, we have equation (28), which along with the "Born-von Karman" condition, we can compute the band structures.

$$E(\boldsymbol{k})^{\pm} = \pm V_{pp\pi}\sqrt{3 + 2cos(\boldsymbol{k}\cdot\boldsymbol{a_1}) + 2cos(\boldsymbol{k}\cdot\boldsymbol{a_2}) + 2cos(\boldsymbol{k}\cdot(\boldsymbol{a_1}-\boldsymbol{a_2}))} \quad \textbf{(29)}$$

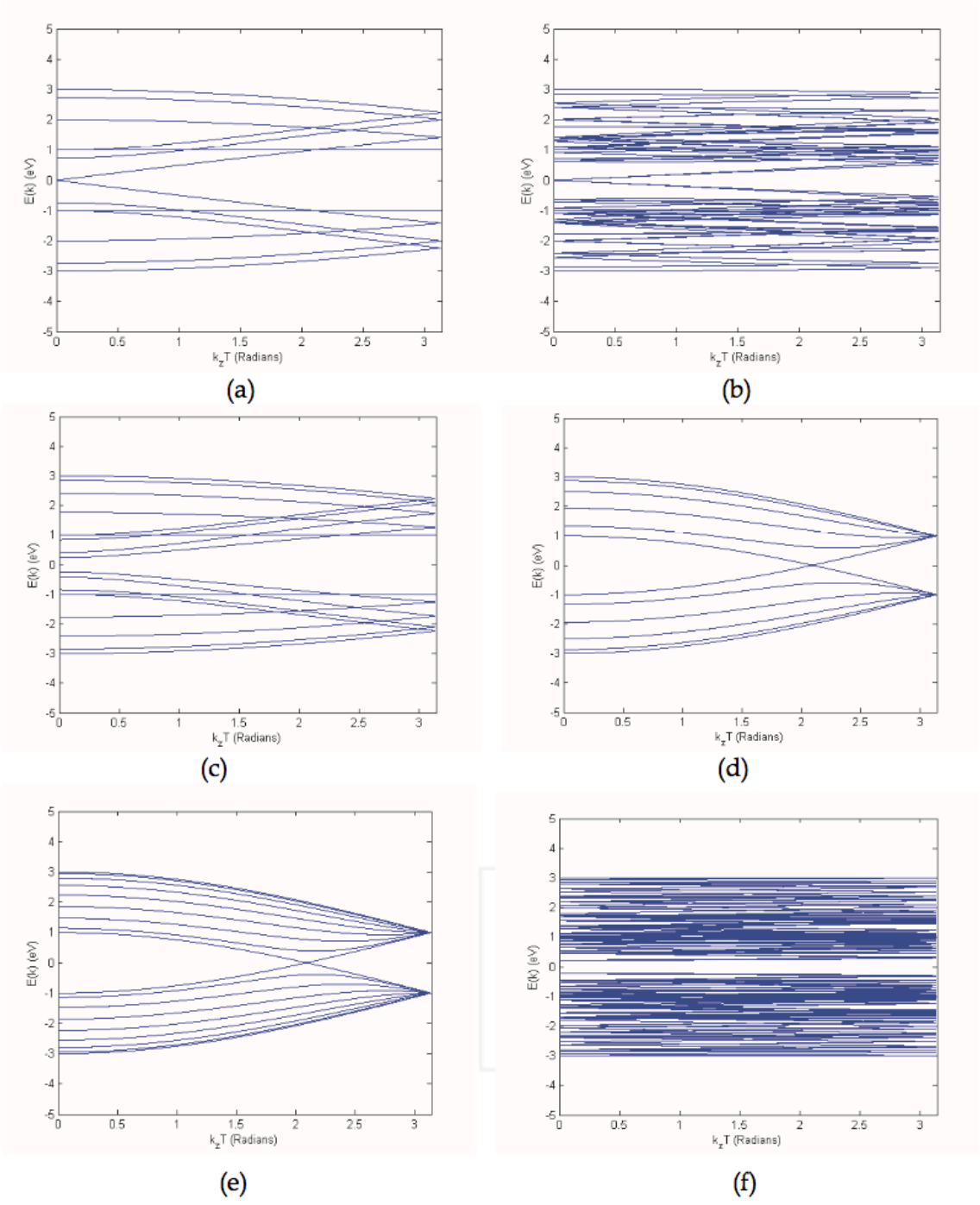

Figure 8: Electronic band structures of different SWCNTs calculated using the π-tight binding model, with chiral vectors (n,m) a) (6,0) b) (6,3) c) (8,0) d) (5,5) e) (8,8) f) (5,4) [21]**.**

Chapter 3: Phonon transport theory/Kapitza resistance models

In this chapter I discuss one of the first theories that predicted the heat capacity of a dielectric solid – the Debye model. Then in order to discuss Kapitza resistance which occurs at the interface between materials, I explain two limiting case models for phonon scattering, the acoustic mismatch model (AMM) and the diffusive mismatch model (DMM).

3.1 Debye model for phonons

Boundary resistance can occur electrically and thermally [22]. For the thermal case, a mismatch of the two density vibrational states (given by the Debye model in this case) cause thermal boundary resistance, specifically the differences between the speed of sound v_D and the specific heat C_V. First I will discuss the Debye model, applying within only one material. The Debye model (acoustic phonon modes) treats atomic vibrations as phonons in a box, and is very similar to the treatment of an EM field as a gas of photons in a box [23]. It predicts the correct heat capacity in a solid and that $C \propto T^3$. This model contrasts the Einstein model (optical phonon modes), which treats the solid as several non-interacting quantum harmonic oscillators.

We will start from the dispersion relation

$$\varepsilon = \hbar\omega,\ \omega = v_s|\vec{q}| \qquad (30)$$

with the phonon energy ϵ, reduced Planck's constant $\hbar$, phonon frequency ω, and the sound wave velocity v_s. Phonons obey Bose-Einstein statistics, and the expectation number of bosons in some state with frequency ω is then given by

$$n(\omega) = \frac{1}{e^{\hbar\omega/k_BT} - 1} \qquad (31)$$

with k_B the Boltzmann's constant [3]. Phonons cannot have infinite frequency and there are N primitive cells then there exists N phonon modes. The wave vector volume is

$$\left(\frac{2\pi}{3}\right)^3 = \frac{8\pi^3}{V} \quad \textbf{(32)}$$

We assume that there is an isotropic cut-off vector $\boldsymbol{q_D} = \boldsymbol{\omega_D}/\boldsymbol{v_s}$ terminating the density of states. Substituting, we can write this cut-off Debye frequency as

$$\omega_D = (6\pi^2 \frac{N}{V})^{1/3} v_s \quad \textbf{(33)}$$

and the Debye temperature corresponding to this frequency is given by

$$T_D = \hbar\omega_D/k_B \quad \textbf{(34)}$$

Next I will derive the specific heat of the material. The speed of sound in the material is assumed constant (Debye approximation), therefore we can write the density of states as

$$D(\omega) = \frac{dN}{d\omega} = \frac{V\omega^4}{2\pi^2 v_s^3} \quad \textbf{(35)}$$

For each type of polarization the thermal energy U is given by

$$U = \int d\omega D(\omega) n(\omega) \hbar\omega = \int_0^{\omega_D} \frac{V\omega^4}{2\pi^2 v_s^3} \frac{1}{e^{\hbar\omega/k_B T} - 1} \quad \textbf{(36)}$$

There are 2 transverse and 1 longitudinal types of polarization. If we further assume the phonon velocity is independent of this, we have

$$U = \frac{3Vk_B^4 T^4}{2\pi^2 v_s^3 \hbar^3} \int_0^{x_D} dx \frac{x^3}{e^x - 1} = 9Nk_B T \left(\frac{T}{T^D}\right)^3 \int_0^{x_D} \frac{x^4 e^x}{(e^x - 1)^2} \quad \textbf{(37)}$$

with $x \equiv \frac{\hbar\omega}{k_B T}$ and $x_D \equiv \frac{T_D}{T}$. Heat capacity is then

$$C_V = \frac{\partial U}{\partial T} = 9Nk_B \left(\frac{T}{T^D}\right)^3 \int_0^{x_D} \frac{x^4 e^x}{(e^x - 1)^2} \quad \textbf{(38)}$$

[3] $k_B = 1.38 \times 10^{-23}$ J/K

Equation (38) does not have a closed form solution. We can approximate this in the low and high temperature limits. In the high temperature limit, $T \gg T_D$, so $e^x = 1 + x$ and we have

$$U = 9Nk_BT\left(\frac{T}{T^D}\right)^3 \int_0^{x_D} x^2 dx = 3Nk_BT, C_V = 3Nk_B \qquad \textbf{(39)}$$

the classical Dulong and Petit Law derived in 1819. In the low temperature limit, $T \ll T_D$, long wavelength acoustic modes only contribute. Then take $x_D \equiv \frac{T_D}{T}$, and from integral tables we have the result

$$\int_0^{\infty} dx \frac{x^3}{e^x - 1} = \frac{\pi^4}{15} \qquad \textbf{(40)}$$

Then finally we have

$$U = 3\pi^4 Nk_BT^4/5T_D^3, C_V = 12\pi^4 Nk_BT^5/5T_D^3 \cong 324Nk_B\frac{T}{T^3} \qquad \textbf{(41)}$$

A plot showing specific heat vs. temperature for a semiconductor vs. conductor is in Figure 9. Note the differences between the two materials.

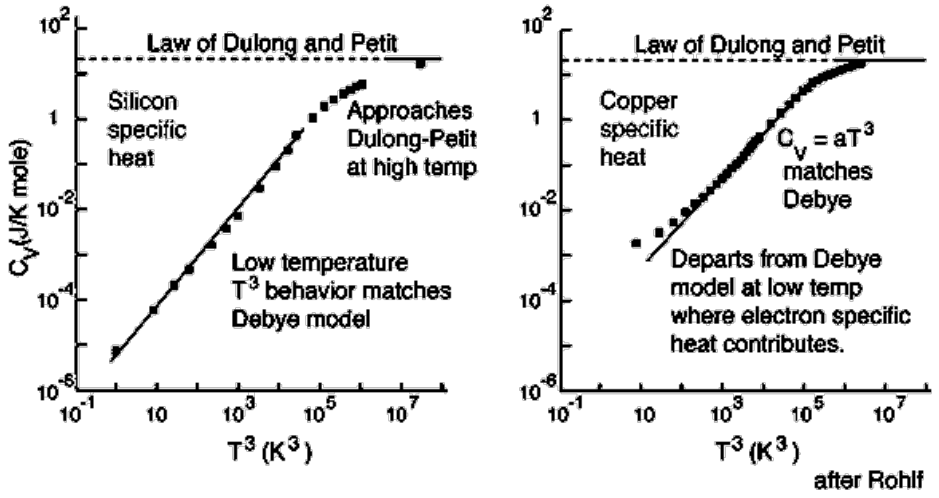

Figure 9: Specific heat vs. Temperature log plot for Si and Cu in the Debye model [24]**.**

For semiconductors, at low temperature their behavior agrees with the Debye model, while for conductors, it does not agree due to the electron contributions. A more complete expression for the specific heat is

$$C_{metal} = C_{electron} + C_{phonon} = \frac{\pi^4 N k^2}{2E_f} + \frac{12\pi^4 N k_B}{5T_D^3} T^3 \qquad (42)$$

incorporating the Einstein model to form the Einstein-Debye specific heat.

This model can be useful for computing thermodynamic properties of carbon nanotubes. Quantities such as the bulk modulus K, a measure of the CNT's resistance to compression, or the shear modulus (resistance to shear stress) or Young's modulus (response to linear stress) [25] can also be calculated. To compute the CNTs specific heat within the tight-binding model, we can use the expression

$$C_V(T) = k_B \int_0^\infty \frac{\left(\frac{\hbar\omega}{k_B T}\right)^2 exp\left(\frac{\hbar\omega}{k_B T}\right)}{\left[exp\left(\frac{\hbar\omega}{k_B T}\right) - 1\right]^2} D(\omega) d\omega \qquad (43)$$

with D(ω) the phonon density of states. This is derived from the dispersion relation which relates energy and frequency/wavenumber as well as results from the Debye model.

$$C_v = \frac{\partial U}{\partial T} = \frac{\partial}{\partial T} \int \epsilon(\omega)\, n(\omega)\, D(\omega)\, d\omega \qquad (44)$$

At high temperatures equation (44) approaches the classical limit $2\, k_B/m$. In the low temperature limit, around 1 K, it is determined by the dispersion of the lowest-energy acoustic branches [20].

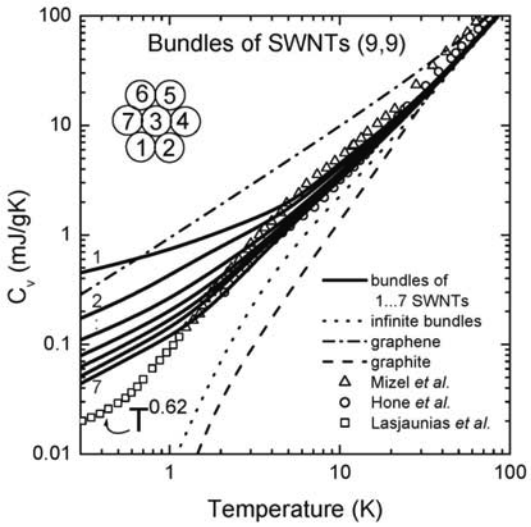

Figure 10: Specific heat of SWNTs and ropes of SWNTs, calculated within a force constant model in comparison with that of graphene and graphite, and available experimental data [20]**.**

I have discussed a model to compute important thermodynamic properties for some materials. However, this model only works within one material. The big question is what happens at the interface between a dielectric, such as some industrial epoxies, and a semiconducting CNT? We need a model to compute the Kapitza resistance at this boundary so we can calculate the thermal conductivity. The two most common models are the Acoustic Mismatch Model (AMM) and the Diffusive Mismatch Model (DMM).

3.2 Phonon scattering models

Before I can discuss those models, I need to discuss phonon transport in general. As explained in chapter 1, the Boltzmann equation (equation (45)) can be used to model phonon transport; however this is not a trivial task. It was said by Ziman in 1960 [26] “The Boltzmann equation is so exceedingly complex that it seems hopeless to expect to generate a solution from it directly”. The Peierls-Boltzmann equation is another name for the form describing phonon transport. Only recently has

computational power and experimental ingenuity allowed for solving this equation directly for a system.

$$\frac{\partial f}{\partial t} + \mathbf{F} \cdot \frac{\partial \mathrm{f}}{\partial \mathbf{p}} = \left(\frac{\partial \mathrm{f}}{\partial \mathrm{t}}\right)_{\mathrm{coll}} \qquad (45)$$

For systems in equilibrium, f (or f_0) is the standard Bose-Einstein distribution,

$$f_0 = \frac{\mathbf{1}}{\boldsymbol{A e^{\hbar\omega/k_B T} - 1}} \qquad (46)$$

However in order to model phonon scattering, some assumptions have to be made. The relaxation time approximation [27] is commonly used to solve the Boltzmann equation, especially when fitting theoretical thermal conductivities to experimental data. The collision term is then linearized assuming the phonon collisions can be represented by a relaxation time and the system in question is subjected to a thermal gradient.

$$-v_p(\boldsymbol{q}) \cdot \nabla T \frac{\partial f_{qp}}{\partial T} + \frac{\partial f_{qp}}{\partial t}|_{scatt} = 0 \qquad (47)$$

Here v_p is the group velocity of phonon (**q**,p), f_{qp} is a non-equilibrium distribution of phonons in state (**q**,p) at a position r, time t, and temperature T, with **q** is wave number and p the polarization. Equation (47) is the general Boltzmann equation for phonons being acting on by a thermal gradient, and is still a integro-differential equation due to the scattering term. Setting the equation equal to 0 is the stationary condition.

Since no mass transfer takes place, phonon momentum is a "quasi momentum". That being said, this quasi momentum transfers the heat energy in the lattice, and this process can be represented as a *normal* process or as an "*umklapp"* process [28] (German meaning to "flip over"), and both are three phonon scattering processes. Conservation of momentum/energy for a normal phonon-phonon scattering event can be

expressed with the equations

$$\boldsymbol{k_1 + k_2 - k_3 = 0}\,, \hbar\omega_1 + \hbar\omega_2 - \hbar\omega_3 = 0 \qquad \textbf{(48)}$$

and total phonon quasi momentum is conserved. Conservation of momentum for an *umklapp* process can be expressed with the equation

$$\boldsymbol{k_1 + k_2 - k_3 = G} \qquad \textbf{(49)}$$

where **G** is a nonzero reciprocal lattice vector responsible for redirecting the phonon's quasi momentum. This can also be expressed pictorially using scattering diagrams.

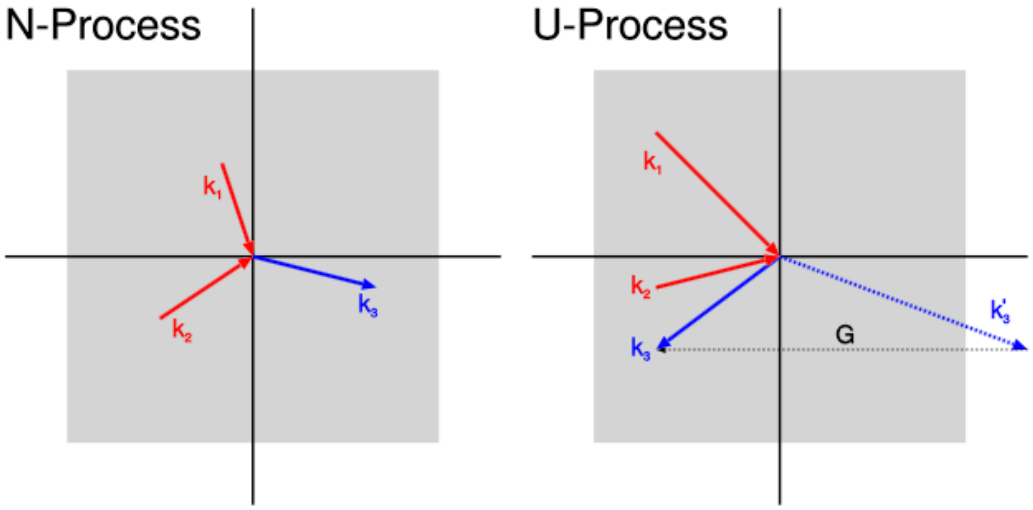

Figure 11: Diagram showing conservation of momentum in reciprocal space for normal (left) and *umklapp* (right) phonon-phonon scattering processes [29]**.**

Umklapp scattering is one factor responsible for limiting the thermal conductivity of a crystalline material, along with crystal defects, surface imperfections, and isotope scattering [29]. They are also not modeled in the standard Debye model I just discussed; however it can be modified to include them (allowing for anharmonic interactions or separate longitudinal and transverse acoustic branches) [28].

In the relaxation time approximation (RTA), the thermal conductivity is given

by

$$\lambda = \frac{1}{3}\frac{1}{(2\pi)^3}\int C_{\boldsymbol{k}} v_g^2 \tau_{RTA} d^3\boldsymbol{k} \qquad \textbf{(50)}$$

with C_k the phonon mode specific heat and τ_{RTA} is the single-mode relaxation time, summing over all branches [28]. This equation has been found to hold experimentally for Ge and Si above 100 K in 2010 by Ward & Broido [30], with the relaxation time defined as

$$\frac{\mathbf{1}}{\boldsymbol{\tau_{RTA}}} = \frac{\mathbf{1}}{\boldsymbol{\tau_N}} + \frac{\mathbf{1}}{\boldsymbol{\tau_U}} \qquad \textbf{(51)}$$

giving the normal and *umklapp* scattering rates.

Equation (50) comes from Callaway's theory for thermal conductivity, first proposed in 1959 [31]. From equation (47), Callaway defined a term from the difference in a distribution having a temperature gradient from that of the equilibrium Bose-Einstein distribution f_0 as

$$f_{\boldsymbol{q}p} - f_0 = -\tau(\boldsymbol{q}, p) v_{\boldsymbol{q}p} \cdot \nabla T \frac{\hbar\omega}{k_B T^2} \frac{e^x}{(e^x-1)^2} \qquad \textbf{(52)}$$

with $x = \hbar\omega_{qp}/k_B T$. If we assume an isotropic solid and $\tau(q) = Aq^{-n}$, we obtain the following proportionality relation for the thermal conductivity:

$$\kappa \propto T^{3-n} \int_0^{\Theta/T} \frac{x^{4-n} e^x}{(e^x-1)^2} dx \qquad \textbf{(53)}$$

with Θ the Debye temperature.

For a more in-depth derivation, see Sparavigna [27]. For an excellent review on higher-order phonon scattering, non-linear effects and relevant models, refer to Dreyer et. al. [32]. I will now begin discussing phonon scattering specifically at an interface as opposed to the general case.

The two models I am about to discuss involve phonon transmission at non ideal surfaces, responsible for heat transfer. They can be derived from considering limiting cases of the Boltzmann equation. The acoustic mismatch model (AMM) is the limiting case which is specular, meaning the wave vector parallel to the interface is conserved. This happens in a crystal when the mean free path (lattice constant a) is much shorter than the wavelength, and no scattering occurs at the interface. It was first developed by Khalatnikov in 1952 [33] following Kapitza's hypothesis of interfacial resistance. This is the model that I assume in my research.

The diffusive mismatch model (DMM) is the case that applies at very rough surfaces where nearly all heat energy is backscattered. This was heavily developed by Swartz and Pohl in 1989 [34].

3.3 Acoustic Mismatch Model (AMM)

Thermal boundary resistance is normally discussed in an elasticity theory formalism. However, I will discuss it here analogous to the reflection and transmission of photons at an interface where the speed of light changes. Since a phonon is either transmitted or reflected, we can write a transmission coefficient $\alpha(\omega,\theta,j)$ that depends on the phonon frequency ω, angle of incidence θ, and phonon mode j (assume constant temperature on both sides) [34]. For acoustic mode phonons, there exist two transverse modes and one longitudinal mode (motion towards/away from each other). Even with the linear approximation we can see the problem is quite a bit more complicated than just Snell's Law. We will also assume a solid-solid interface and that the phonons act as plane waves (continuum acoustics) or that the phonon sees no crystal lattice.

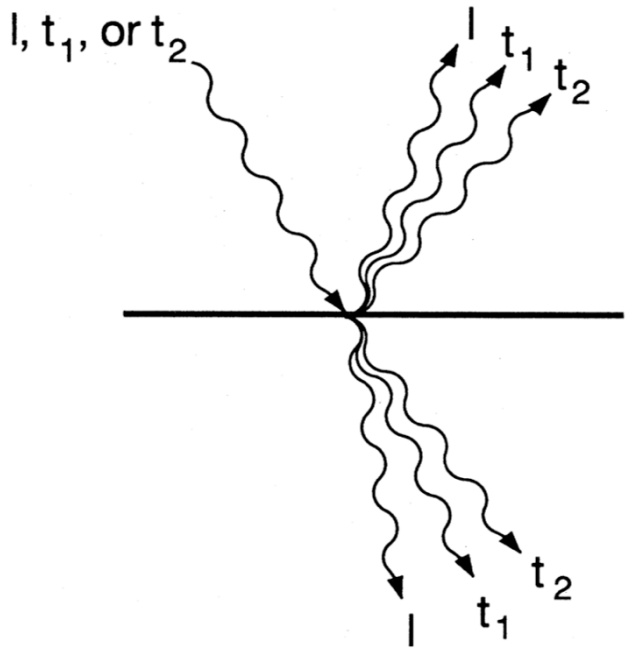

Figure 12: Example schematic of the many different possibilities that exist in the acoustic mismatch model for phonons at an interface [34]**.**

The total heat current density from side one to two (from Fourier's law) is $[\frac{1}{A}]\dot{Q}_{1\to 2}^{tot}(T)$, and this must be summed over all frequencies and angles of incidence of the number of phonons at a certain frequency and angles θ, φ on a unit area A per unit time times the phonon energy $\hbar\omega = \hbar c_{1,j}k$. In this formula j is the phonon mode, c is the phonon velocity in side one with mode j, and ω is the phonon frequency. Let φ be the azimuthal angle of incidence and θ the angle between the phonon's wave vector and the normal vector to the interface. Then $c_{1,j}\cos(\theta)$ is the normal component of velocity, the solid angle is $d\Omega = d\varphi \sin(\theta)\, d\theta$, and $N_{1,j}(\omega, T)$ is the density of the phonon states at the given angles times the Bose occupation (degeneracy) factor. Putting this all together, we have the expression

$$\left[\frac{1}{4\pi}\right] N_{1,j}(\omega, T) d\Omega c_{1,j} cos(\theta) \qquad \textbf{(54)}$$

Integrating this over all angles gives us $c_{1,j}N_{1,j}(\omega,T)$. Now we can write the total heat current as (pulling out the 2π)

$$\left[\frac{1}{A}\right]\dot{Q}^{tot}_{1\to 2}(T) = \frac{1}{2}\sum_j \int_0^{\omega_1^{max}} \int_0^{\pi/2} N_{1,j}(\omega,T)\hbar\omega c_{1,j}\alpha_{1\to 2}(\theta,\omega.j)\cos(\theta)\sin(\theta)d\theta d\omega \quad \textbf{(55)}$$

ω_1^{max} is the maximum phonon frequency on side one. If we assume a small reduced temperature difference $(T_2 - T_1)/T_2$, one can solve for the thermal boundary conductivity.

$$h_{Bd} = \dot{Q}^{tot}_{1\to 2}(T_2) - \dot{Q}^{tot}_{1\to 2}(T_1)\Big/A(T_2 - T_1) \quad \textbf{(56)}$$

Therefore to calculate the Kapitza resistance in theory we only need to know the transmission probabilities.

Let us assume that the total heat flow from side 1 (T_1) to side 2 (T_2) is the difference between the gross heat flow from side 1 to side 2, when side 1 has a temperature of T_1, and also the difference between the gross heat flow from side 1 to side 2 when side 1 has a temperature of T_2. Then the temperature of side 2 does not need to be considered [34]. This quantity will be T from here on out. Also let us assume the transmission probability (coefficient) to be independent of temperature. This is not required for these models but it makes the explanation simpler.

We can write a more succinct expression for the acoustic impedance $Z_i = c_i\rho_i$ using the mass density ρ and the phonon velocity c. Then the transmission probability can be written as

$$\alpha_{1\to 2} = 4Z_1Z_2/(Z_1+Z_2)^2 \qquad (57)$$

Many times the solids are assumed to isotropic Debye solids as it does not substantially affect the results (longitudinal and transverse speeds of sound are not the same). Many of these formulas will include similarities to those in the Debye model I covered in 3.1 Debye model for phonons. For frequencies that are below the Debye cutoff frequency, denoted by ω_i^{Debye},

$$N_{1,j}^{Debye}(\omega,T)d\omega = \frac{\omega^2 d\omega}{2\pi^2 c_{1,j}^3[exp\left(\frac{\hbar\omega}{k_BT}\right)-1]} \qquad (58)$$

Now I will define the following quantity $\Gamma_{1,j}$,

$$\Gamma_{1,j} = \int_0^{\pi/2} \alpha_{1\to 2}(\theta,j)cos(\theta)sin(\theta)d\theta \qquad (59)$$

These polynomial integrals can be looked up in tables or computed. Then from equations (58) and (59) a simplified expression for the thermal boundary conductance can be written,

$$h_{Bd} = \frac{1}{2}\sum_j c_{1,j}\Gamma_{1,j}\int_0^{\omega_1^{Debye}} \hbar\omega \left[{dN_{1,j}(\omega,T)}/{dT}\right] d\omega \qquad (60)$$

In the low temperature limit, the upper frequency limit can be taken as infinity, and we have the analytical solution

$$R_{Bd} = \left[\frac{\pi^2}{15}\frac{k_B^4}{\hbar^3}\left[\sum_j c_{1,j}^{-2}\Gamma_{1,j}\right]\right]^{-1} T^{-3} = \left[2.04X10^{10}\left[\sum_j c_{1,j}^{-2}\Gamma_{1,j}\right]\right]^{-1} T^{-3}\left[\frac{sec^2}{cm^2}K^3\frac{K}{W/cm^2}\right] \qquad (61)$$

Also R_{bd} may be approximated (using the Debye model) as $\left[\frac{1}{4}C_v c\alpha\right]^{-1}$, with C_v the Debye specific heat, α an averaged transmission probability, and c the Debye phonon

velocity. Let us look at the special case where the material is the same on both sides of the interface. The Γ's are all 0.5 and the α's are all 1. Then equation (61) becomes

$$R_{Bd} = \left[1.02x10^{10}\left[\sum_{j} c_{1,j}^{-2}\right]\right]^{-1} T^{-3}\left[\frac{sec^2}{cm^2}K^3\frac{K}{W/cm^2}\right] \qquad \textbf{(62)}$$

We see the thermal boundary resistance does not disappear even at these types of interfaces where the material is the same. The first part of equation (62) basically tells us a rate of propagation from the harmonic mean of all phonon modes. This model can give a lower limit to the thermal boundary resistance by assuming the transmission probability α is 1.

3.4 Diffusive Mismatch Model (DMM)

This model relies more on phonon scattering or "diffusing" at an interface. It can give an upper limit for how much diffusive scattering may affect the thermal boundary resistance [34]. In this model, at a typical solid-solid interface with a small difference in their acoustical properties, around 50% of the phonons scattered at the interface are transmitted. That means that the effect of diffuse scattering at these interfaces is relatively small ($< \pm 30\%$) [34].

To derive this model, the only quantity that must be changed from the AMM derivation is the transmission probability. We must also assume the principle of detailed balance, and define mathematically what diffuse scattering is at the interface. We say that a phonon is diffusively scattered if the final phonon's wave vector $\boldsymbol{k_f}$ and mode j_f are independent of $\boldsymbol{k_i}$ and j_i. This is also called the memoryless, or Markovian property. We also will assume that every scattering event is elastic ($\hbar\omega_i = \hbar\omega_f$). By doing this,

no correlations between the incoming and outgoing phonons except those of energy are accounted for, and the structure of the scattered particles are not accounted for either.

Therefore a phonon's transmission probability is also independent of its mode and wave vector ($\alpha_{i,j}(\omega, \boldsymbol{k}) = \alpha_i(\omega)$). Now an equation that describes the principle of detailed balance can be written[4].

$$\alpha_i(\omega) = 1 - \alpha_{opp\ i-i}(\omega) \qquad \textbf{(63)}$$

Equation (63) states that the transmission probability on one side must equal the reflection probability on the other.

Similarly from Chapter 3.2 Phonon scattering models, an equation for the number of phonons with an energy $\hbar\omega$ that leave side i per unit area per unit time is

$$\sum_j \int_0^{2\pi} \int_0^{\pi/2} d\theta cos(\theta) d\phi N_{i,j}(\omega, T) c_{i,j} \alpha_i(\omega) \qquad \textbf{(64)}$$

These integrals over the angles immediately give us ¼, and substituting equation (63) (principle of detailed balance) results in

$$\sum_j c_{i,j} N_{i,j}(\omega, T) \alpha_i(\omega) = \sum_j c_{opp\ i-i,j} N_{opp\ i-ij}(\omega, T)[1 - \alpha_i(\omega)]] \qquad \textbf{(65)}$$

Solving for the transmission probabilities, we get

$$\alpha_i(\omega) = \sum_j c_{opp\ i-i,j} N_{opp\ i-i,j}(\omega, T) \Big/ \sum_{i,j} c_{i,j} N_{i,j}(\omega, T) \qquad \textbf{(66)}$$

[4] $\alpha_{opp\ i\text{-}I}$ denotes the side of the interface i and its opposite side

With this formula we can calculate the total heat flux and therefore Kapitza resistance in the DMM. Making the generalized Debye approximation as in Chapter 3.2 Phonon scattering models, we obtain

$$\alpha_i(\omega) = \sum_j c_{opp\ i-i,j}^{-2} / \sum_{i,j} c_{i,j}^{-2} \qquad \textbf{(67)}$$

To obtain the thermal boundary resistance, we will use equations (58) & (59) from the previous section. Substituting equation (67) gives

$$\Gamma_{i,j} = \int_0^{\frac{\pi}{2}} \frac{\sum_j c_{opp\ i-i,j}^{-2}}{\sum_{i,j} c_{i,j}^{-2}} cos(\theta) sin(\theta) d\theta = \frac{1}{2} \frac{\sum_j c_{opp\ i-i,j}^{-2}}{\sum_{i,j} c_{i,j}^{-2}} \qquad \textbf{(68)}$$

These results tell us that

$$\left[\sum_j \boldsymbol{c_{i,j}^{-2} \Gamma_{i,j}}\right] = \frac{\mathbf{1}}{\mathbf{2}} \frac{\left(\sum_j c_{i,j}^{-2}\right)\left(\sum_j c_{opp\ i-i,j}^{-2}\right)}{\sum_{i,j} c_{i,j}^{-2}} \qquad \textbf{(69)}$$

These sums are over all phonon modes for every phonon velocity. Similarly to the expression for thermal boundary resistance in the AMM, we now can write a similar expression for the DMM.

$$\begin{aligned} R_{Bd} &= \left[\frac{\pi^2}{15}\frac{k_B^4}{\hbar^3}\frac{1}{2}\left[\sum_j c_{1,j}^{-2}\Gamma_{1,j}\right]\right]^{-1} T^{-3} \\ &= \left[1.02X10^{10}\left[\sum_j c_{1,j}^{-2}\Gamma_{1,j}\right]\right]^{-1} T^{-3}\left[\frac{sec^2}{cm^2}K^3\frac{K}{W/cm^2}\right] \end{aligned} \qquad \textbf{(70)}$$

We obtain exactly half as expected from equation (62). It is interesting to compare the models to each other; I will look at the low temperature limit in order to do this. Writing an expression for the ratio of the Kapitza resistance in the DMM to the AMM, we obtain

$$R_{DMM}/R_{AMM} = 2\frac{\left(\sum_j c_{i,j}^{-2}\Gamma_{i,j}\right)\left(\sum_{i,j} c_{i,j}^{-2}\right)}{\left(\sum_j c_{i,j}^{-2}\right)\left(\sum_j c_{opp\ i-i,j}^{-2}\right)} \quad (71)$$

If we assume the acoustical properties on both sides are the same as before, we get $R_{DMM}/R_{AMM} = 2$.

3.5 Physical explanation of thermal boundary resistance

Now that I have covered the mathematics of the AMM and DMM, it is important to give an intuitive explanation of the practicality of both models.

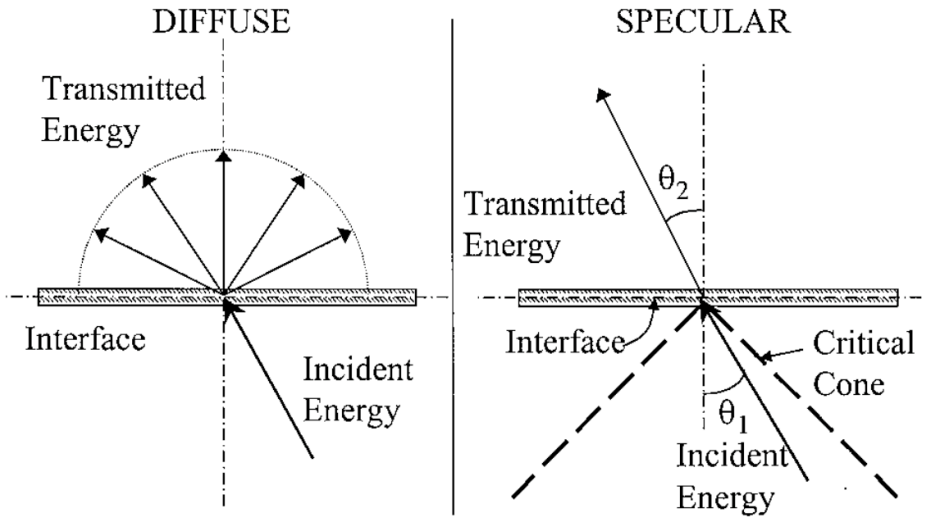

Figure 13: Diffuse (DMM) vs. specular (AMM) transmission at an interface. The critical cone gives limits for the incoming phonon's angle assuming transmission [8]**.**

As one can see from Figure 13, both models depend on the transmission coefficient α at the interface. The AMM computes this coefficient based on continuum acoustics and the mismatch of the acoustical properties between the materials at the interface [8]. The DMM computes this coefficient assuming elastic diffusive scattering at the interface.

Both use the Debye density of states (DOS), which makes several unrealistic simplifications, and some have suggested using a more realistic DOS [35].

The DMM is more of a high-temperature model as it relies on the scattering of phonons at the interface. The "roughness" of an interface from the point of view of a phonon has to do with its wavelength compared to the average spatial variation of the boundary. At low temperatures, the AMM is more suited since the interface appears more perfect and smooth. For solid-solid interfaces at high temperatures, both models predict almost the same results for R_b, once again given by

$$R_b = \Delta T / q_{net} \qquad \textbf{(72)}$$

with ΔT the temperature difference across the interface, and q_{net} the total heat transfer per unit area.

The problem of Kapitza resistance is still an active area of research as can be seen from Figure 14. For interfaces such as that of solid Helium III and copper, the effects of phonon (especially Rayleigh) scattering cause both models to be off by orders of magnitude. A "fractal" based model by Majumdar [36] agrees well with experiment for this case. Both models are very dependent on temperature, and can be used as limits when estimating R_b for an experiment. In the next chapter I will apply the AMM to my research.

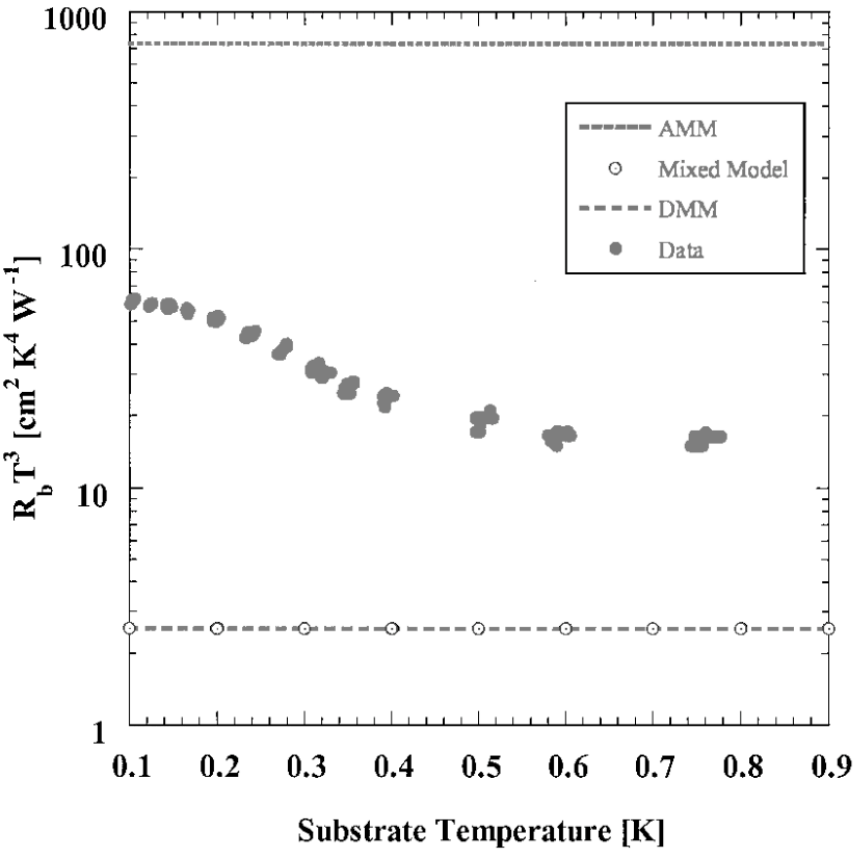

Figure 14: Experimental comparison of R_b's for a He-III/Cu interface by the AMM, DMM, and a mixed "fractal" model [37].

Chapter 4: Random Walks

4.1 Review of method

In this chapter I will discuss the random walk method used to calculate the thermal conductivity k of a CNT-polymer matrix, along with how I specifically implement this in my code package and my results.

Interfacial or Kapitza thermal resistance occurs at an interface between two materials, due to the differences in the material's properties such as the speed of sound in the material and its specific heat [7]. The fact that CNTs have a thermal conductivity several orders of magnitude greater than common epoxy-like dielectric matrix materials is a direct cause of that as well. Functionalizing the ends of a CNT allows for improved coupling of the vibration spectrum between the CNT and its polymer matrix, thereby reducing the Kapitza resistance. However, functionalizing the sides of a CNT may increase the Kapitza resistance as ballistic transport takes place along the direction of the CNT. Aligning the CNTs in the direction of heat flow can improve the thermal conductivity even greater, exploiting their anisotropic thermal conductivity. This can be done using a method called electrophoresis, which can take advantage of the dipole moment inherent in CNTs, causing a torque to be applied and thus aligning them [38] [39]. The goal of this would be to develop a cost-effective alternative to metals for heatsinks and thermal interface materials (TIM) that conduct heat in one direction and are light and durable.

Many experiments have been carried out investigating if CNT-polymer based nano composites have potential. The chemical interaction between a functionalized

CNT and its polymer matrix is significantly greater than between a pristine CNT and its matrix, as well as having an increased Vickers hardness [40]. Bonnet et. al. found an increase of 55% for a 7% volume fraction SWCNT-polymethylmetacrylate (PMMA) polymer composite [41], while Bryning et. al. found that SWCNTs prepared in a suspension of N-N-Dimethylformamide (DMF) allows for greater loading and for a higher thermal conductivity [42]. Chen et. al. found that functionalizing a CNT with carboxylic acid (COOH) inside of a silicon grease matrix decreases the thermal impedance almost two-fold at 2% weight fraction, but then begins to increase at higher concentrations [12]. Lee et. al. demonstrated an experimental method to asymmetrically end-functionalize MWCNTs [43]. Many molecular dynamics simulations have been researched as well on these nano composites [44] [45] [46] [47].

In order to understand the maximum possible improvement in thermal conductivity obtained by functionalizing the ends of CNTs, we simulated the heat flux through a toy model of a nanocomposite. The computational model that is used is an on-lattice random walk method, which is similar to other papers [48]–[50] that have used an off-lattice Monte Carlo method. However, the key difference is that we model the effects of both end-functionalized carbon nanotubes and pristine carbon nanotubes and investigate the expected increase in thermal conductivity due to a CNT's functionalized ends. This is a general model as we do not model specific groups of candidates to functionalize their ends with, but we investigate their effects.

This type of motion in a material is known as Brownian motion, which may be described as a normal distribution with zero mean and a standard deviation which depends on D_m, the matrix thermal diffusivity. In each spatial dimension, the standard

deviation of the distribution is $\sigma = \sqrt{2D_m \Delta t}$, with Δt the time step. D_m is set to 1 for these simulations for convenience.

In our model we treat CNT thermal conductivity as being infinite, allowing us to not model random walks inside the CNTs. The simulation begins by setting up a simulation box with CNTs randomly dispersed throughout the polymer matrix material and aligned either horizontally (parallel to heat flow), vertically (perpendicular to heat flow), or randomly with respect to the heat flow. The heat flux remains constant throughout the simulation. An example of the setup is given in Figure 19. Random walkers (phonons) spawn at a constant rate at x=0 (hot walkers) and x=100 (cold walkers) and take an on-lattice random walk throughout the material. In the X direction we have reflective boundary conditions (isothermal), thereby fixing the heat flux in the system, and periodic boundary conditions in the Y and Z directions (constant flux). As the heat flux is constant, a non-equilibrium steady state occurs once the simulation has converged and the profile dT/dx is linear. Fourier's law of heat conduction can then be used to find the thermal conductivity ($q = -k\frac{dT}{dx}$). The temperature is computed by histogramming the locations of the walkers; hot walkers add to the temperature and cold walkers subtract from the temperature. The simulation box size is 100x100x100 and 210000 total walkers & 35000 timesteps were used. Three different tube lengths were investigated: 10, 15, and 20 in units of the simulation box. The paths these walkers are allowed to take are shown below in Figure 15 (2D) and Figure 16 (3D)

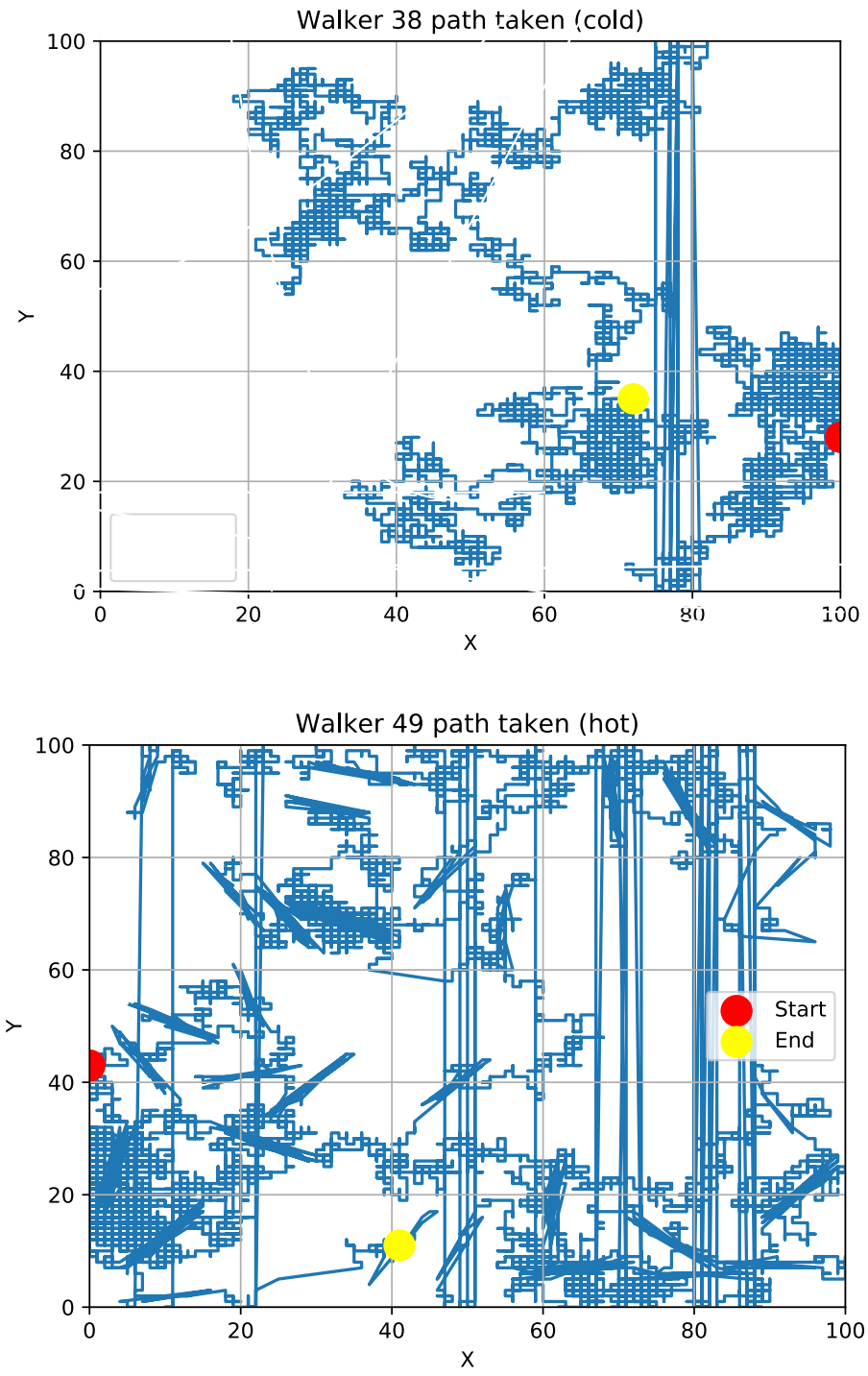

Figure 15: Example random walk paths in 2D, D=1 (steps per timestep). Above-normal random walk (without CNTs). Below-Kapitza/tunneling model type random walk (with CNTs). Periodic boundary conditions are also visible as lines across the box.

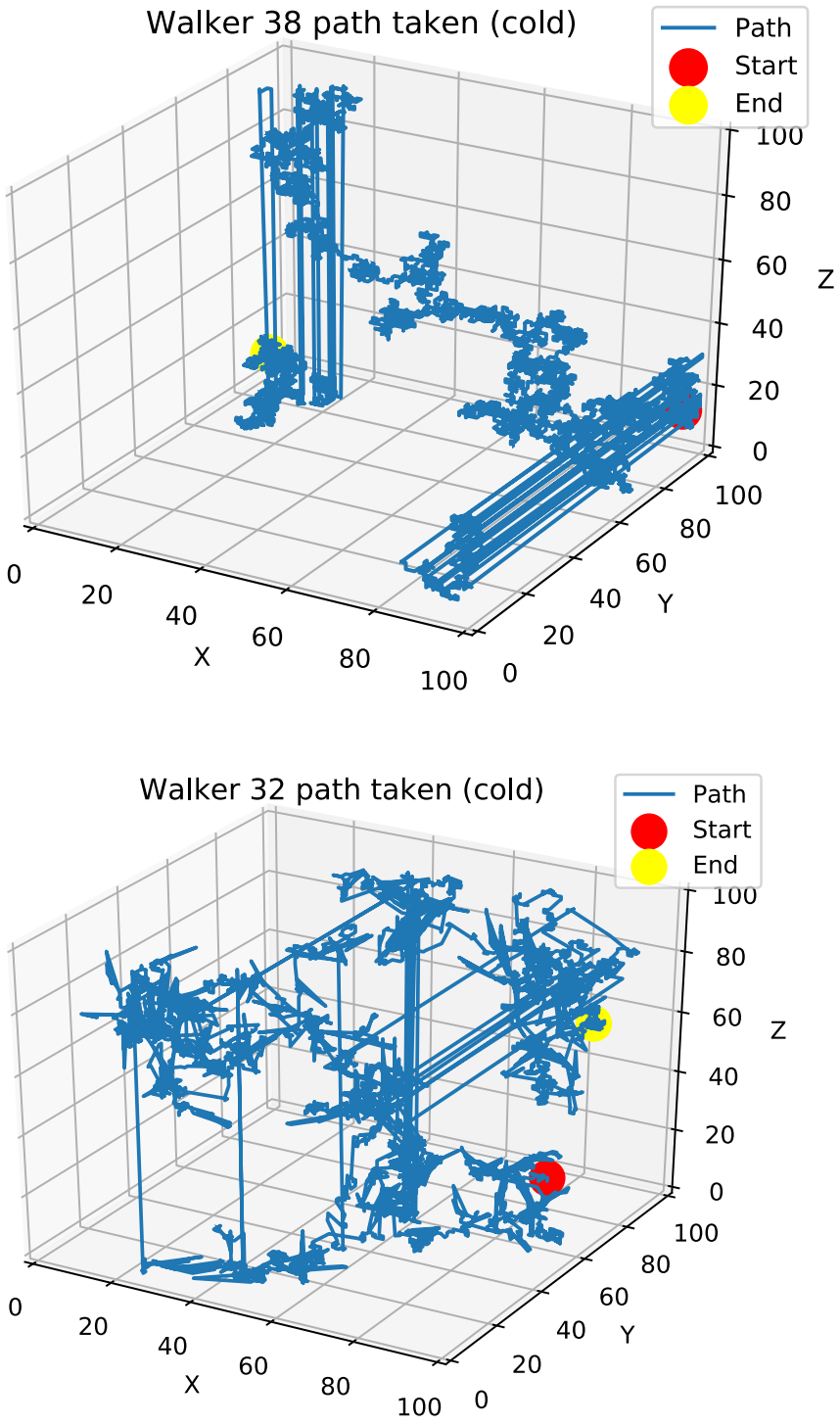

Figure 16: Example random walk paths in 3D, D=1 (steps per timestep). Above-normal random walk (without CNTs). Below-Kapitza/tunneling model type random walk (with CNTs). Periodic boundary conditions are also visible as lines across the box.

We looked at four types of models which govern the rules of the simulation:

- *Tunneling without volume*. In this model if a walker lands on either CNT end it can only walk off or jump to the other end. This models the very high k values on the functionalized ends only. However, CNTs are allowed to cross each other in space and the excluded volume of the CNT itself is not modeled. While not physical, it gives intuition and may be useful in areas that involve networks, such as friend networks on Facebook or the World Wide Web (WWW).

- *Tunneling with volume*. This model is identical to the first case however the CNTs have volume & are not allowed to intersect. This is the limit of infinite Kapitza resistance.

- *Kapitza without end functionalization*. In this model a walker can move around inside a tube (randomly) and has a non-trivial chance of entering/exiting through the sides. When a walker is at a CNT interface, the walker will move into the CNT phase with a probability P_{m-CN} or stay at the previous position in the matrix with a probability $1 - P_{m-CN}$, a constant of the simulation representing the thermal boundary (Kapitza) resistance. If it stays within the CNT its position is randomized to any location in the CNT, reflecting the high thermal conductivity of the CNT. This model prohibits CNT crossings in space and models the excluded volume as well. CNTs are face-connected to ensure detailed balance is upheld.

- *Kapitza with end functionalization*. This model is identical to the previous model except that both ends of the CNT have $P_{m-CN} = 1$ always, meaning that if a walker chooses to land on a CNT end it will enter it with no resistance and move to a random position within the CNT, and at the same time if a walker chooses to land on CNT volume, a generated random number will have to be less than the set value for P_{m-CN} to enter it. This models the Kapitza resistance of the CNT volume pixels and the significantly higher thermal conductivity of the functionalized ends with respect to the matrix/CNT phases. Ideally the phonon modes would be matched using the ends between the matrix and CNT phases.

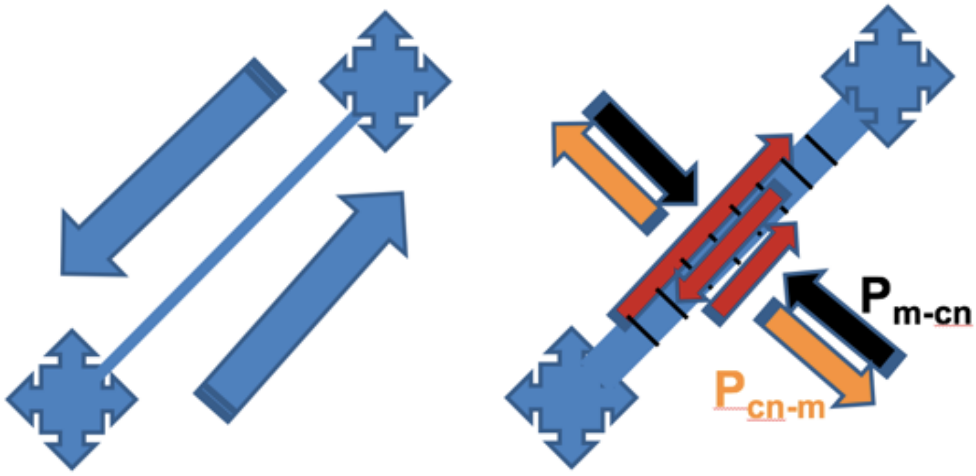

Figure 17: Diagrams of how "walkers" (phonons) propagate in a CNT during a random walk simulation for different models. Left-tunneling model. Right-Kapitza model.

In order to visualize a setup of what the CNTs look like in a simulation box, see the next two figures.

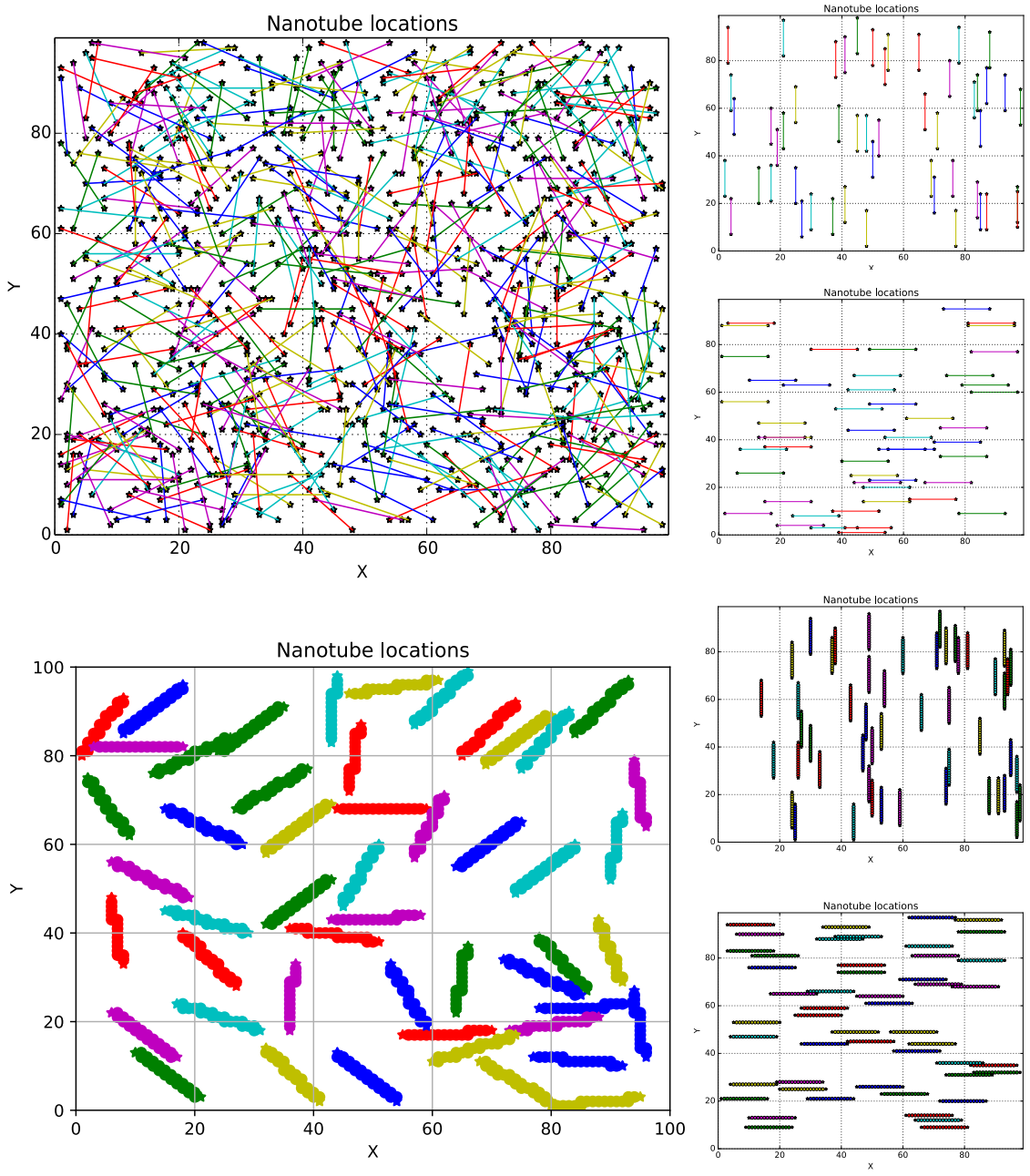

Figure 18: CNTs generated inside a 2D simulation box, where free space is modeled as a polymer matrix (or epoxy-like material). Top-tunneling model. Bottom-Kapitza model. CNT length is 15 units & the volume filling fraction is less than 1% for all plots. Going clockwise, random, vertical (perpendicular to heat flow), and horizontal (parallel to heat flow) orientations are shown. In my random walk package, a similar setup is generated automatically for each simulation run.

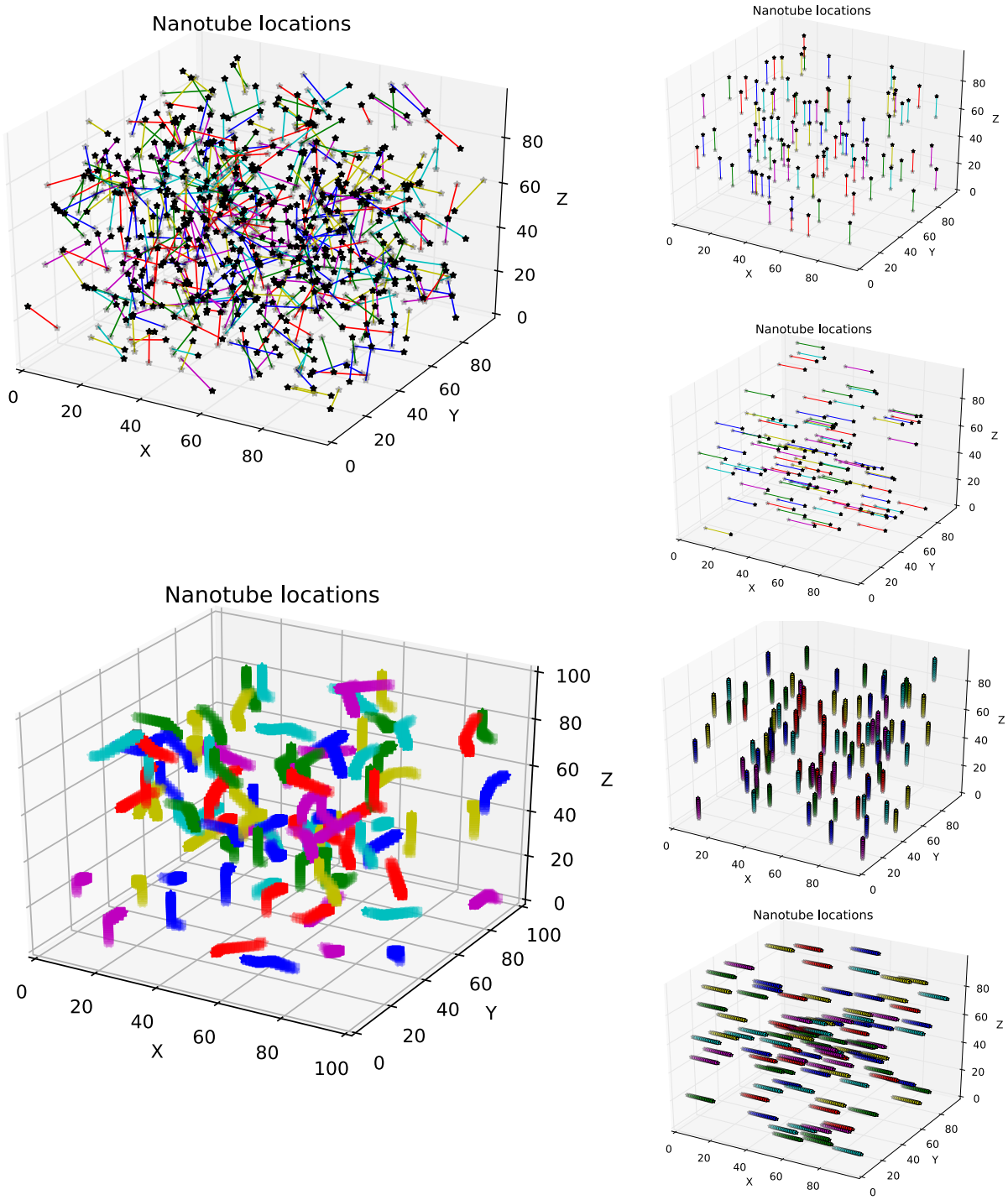

Figure 19: CNTs generated inside a 3D simulation box, where free space is modeled as a polymer matrix (or epoxy-like material). Top-tunneling model. Bottom-Kapitza model. CNT length is 15 units & the volume filling fraction is less than 1% for all plots. Going clockwise, random, vertical (perpendicular to heat flow), and horizontal (parallel to heat flow) orientations are shown. In my random walk package, a similar setup is generated automatically for each simulation run.

There are three phases of material: CNT volume, CNT functionalized ends, and polymer matrix (empty space). Several assumptions are made in this model:

- Walkers distribute uniformly inside the CNTs ($k_{ends} >> k_{CNT} >> k_{matrix}$).
- Collisions between walkers are ignored. The random walk models phonon scattering within the disordered matrix material. Walker-walker collisions would imply that the thermal conductivity depends on the local temperature, and they are ignored.
- The material properties do not change with respect to temperature over the range of the model.
- Thermal resistance for a heat walker entering a CNT from the matrix equals that entering the matrix from a CNT (principle of detailed balance). Indeed, for an on- lattice simulation we find that $P_{m-cn} = P_{cn-m}$.

The code package developed for this simulation is called PRTCNT and is available at https://github.com/tab10/conduction with a MIT license. It is written in Python and MPI and is parallelized for speed to run on any number of cores and on supercomputers.

4.2 Implementation of method

4.2.1 Specific implementation in code package 'PRTCNT'

We start by setting up an empty box for the simulation. Since we are on-lattice, tube points are restricted to integers. Then we generate the positions of the CNTs. I do this by picking a random point in the box and setting it as the left point. I use simple

trigonometry to generate random angles, then get the right endpoint using tube length and those angles. If it is in the box we keep the point, else toss it. I also ensure line or face connection on a lattice for the CNT points.

Once tubes are generated, to calculate volume filling fractions we have

$$\% = \#tubes * \frac{tubelength}{gridsize^{dim}}. \quad \textbf{(73)}$$

I round final right endpoints to make them on lattice, so this formula isn't exact and filling fraction is computed by counting the total squares in simulation which is. I have outlined the rules in detail with charts in Appendix A: Random walk simulation rules.

In my implementation, the first walker runs for the total number of time steps, then only the last position of the walker is histogrammed into an array. Then the next walker runs for the total timesteps-1 and that position is histogrammed. This occurs until there are no time steps or walkers left. This means that the total walkers/2 must be a multiple of the total time steps. It is total walkers/2 as half are treated as "hot" and the other half as "cold". This is done to capture a "snapshot" in time of the particular system, having fixed its heat flux and knowing the simulation box area/volume.

The "hot" walkers are treated as +1 in the histogram and "cold" walkers as -1. This gives a uniform temperature distribution in steady state following Fourier's law of heat conduction. Now the periodic dimensions are collapsed in the histogram (3D or 2D simulations to 1D) by summing. A line is then fit using linear regression to this collapsed histogram, T(x), giving us dT/dx.

Heat flux is fixed in our simulation as mentioned before, following the expression $q = total\ walkers/(total\ timesteps * grid\ size^{dim-1})$. Grid size was set

to 100 for our simulations. Therefore to get thermal conductivity, we have the expression $k = -q/(\frac{dT}{dx})$. Enough walkers and a long enough time interval must be chosen in order for the simulation to converge. In 2D, 50000 walkers and 25000 timesteps was chosen and in 3D, 210000 walkers and 35000 timesteps was chosen.

There are 4 choices to move in 2D and 6 in 3D on-lattice. Because of this fact, we can derive an exact value for the thermal conductivity of the empty boxes. The simulation has dimensionless units, and as k is how easily these walkers flow throughout the box, in the limit we have k=0.50 for 2D and $k = 0.00333\overline{3}$ for 3D. k is defined differently for 2D and 3D in terms of dimensions, so it is important not to compare the two. These values were used as a check to make sure the code is working properly as an empty box yields these values to ±0.001 for 2D and ±0.000001 for 3D with specified simulation settings.

The value for k is very sensitive to the linear fit, and for the simulations I have run I removed the first and last 3 values of T(x) at the edges before the fit. This parameter is fixed in the code and calibrated to give the correct analytical k values in an empty box as given above, and should not be changed without rechecking the vacuum k values and quality of the fit (this plot is auto-generated with a goodness of fit R^2).

In addition to the *random walk* simulation, a *rules test* simulation for any setup can be selected to run instead. This simulation can be run to check the validity of the rules governing the simulation to make sure that the principle of detailed balance is upheld and heat is not being trapped or held anywhere within the simulation.

The value of $P_{cn\text{-}m}$ has not been discussed yet, which is the probability for a walker to exit a CNT into the matrix. Since we are on-lattice, we have that $P_{m\text{-}cn}$=$P_{cn\text{-}m}$

and the two probabilities are equal. From the *rules test* simulations, we can see that detailed balance is upheld and the CNTs or the matrix are not retaining heat; therefore this is correct. If the average walker density within the CNTs during a simulation does not equal the average walker density within the matrix during a simulation, then these two probabilities are not equal and a weighting factor must be applied to uphold detailed balance [48]. A schematic of the computational process is given in Figure 20.

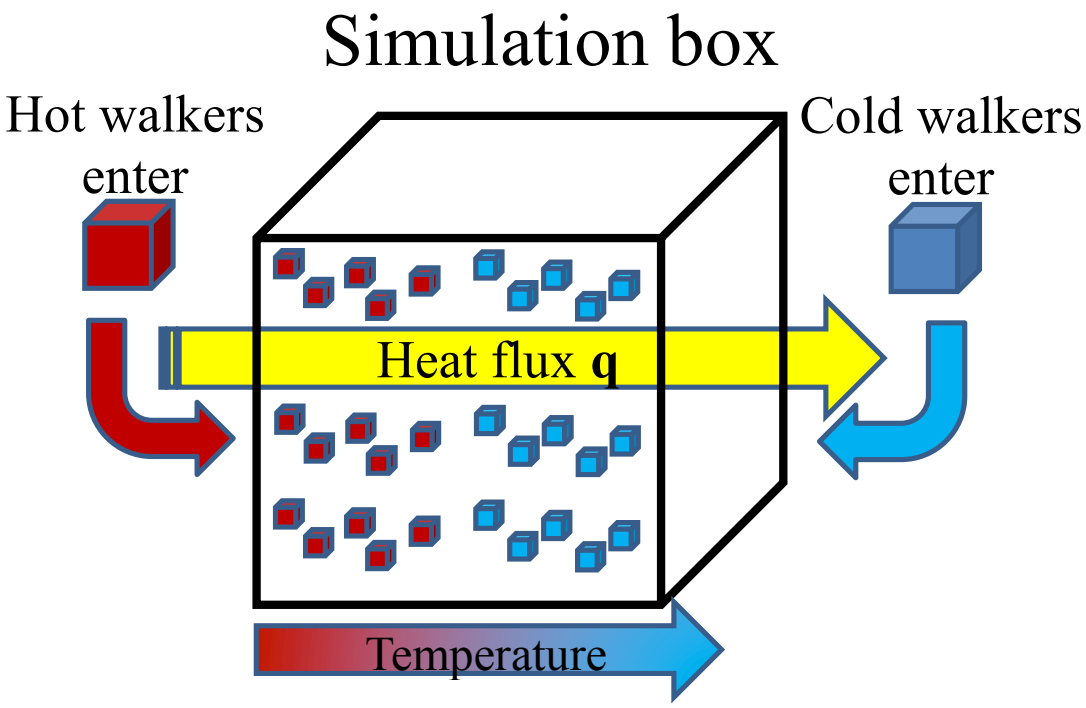

Figure 20: Figure depicting the computational process of running the random walk method for obtaining the thermal conductivities of nanotube composites from simulation.

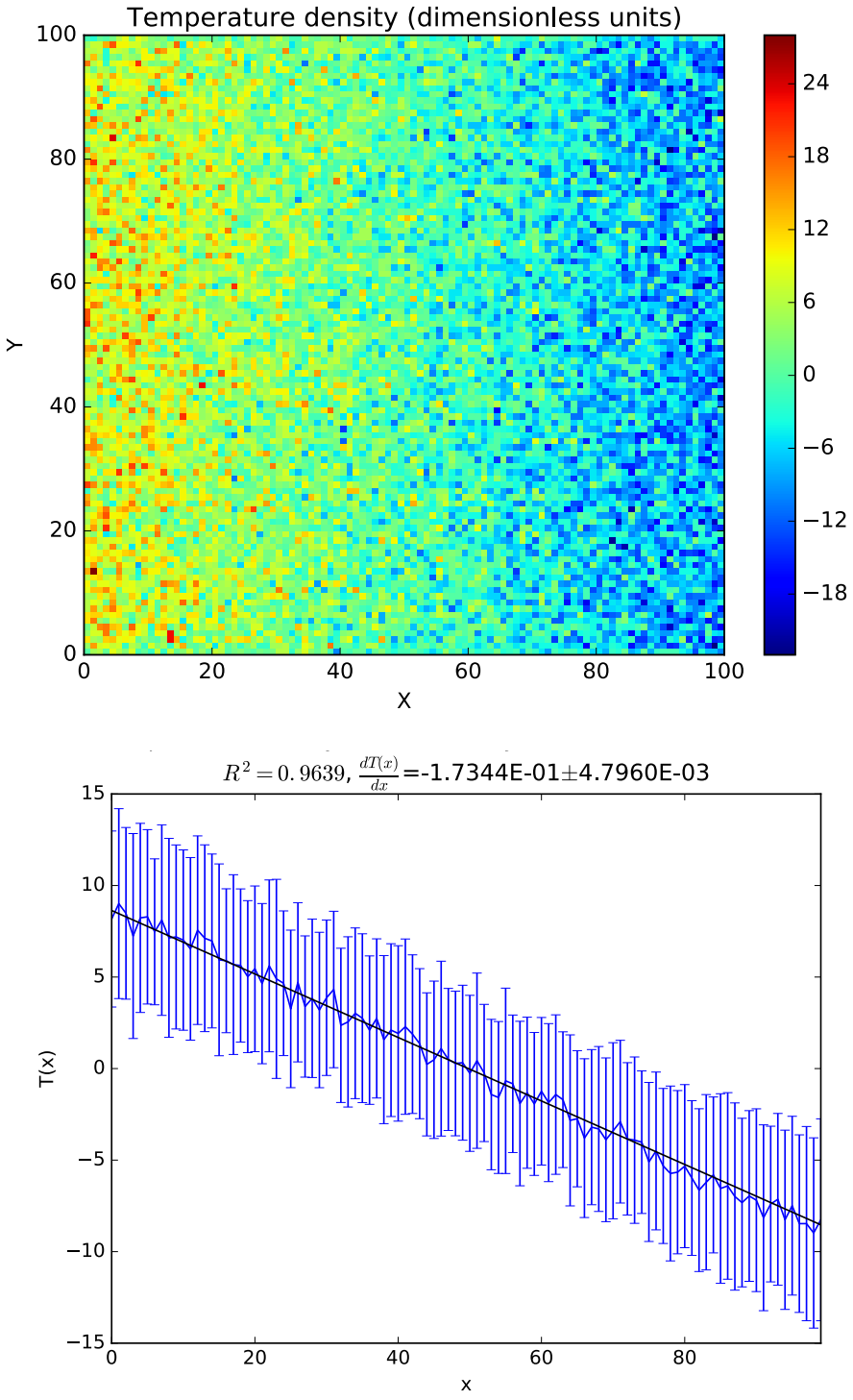

Figure 21: Above-Example of temperature histogram for random walk simulation in 2D. Below-The same histogram collapsed to 1D, with the linear regression applied. The slope is dT/dx, and error bars at each point are shown. As the error bars are roughly the same size, the simulation has converged. This simulation was in 3D, with a box size of 100x100x100.

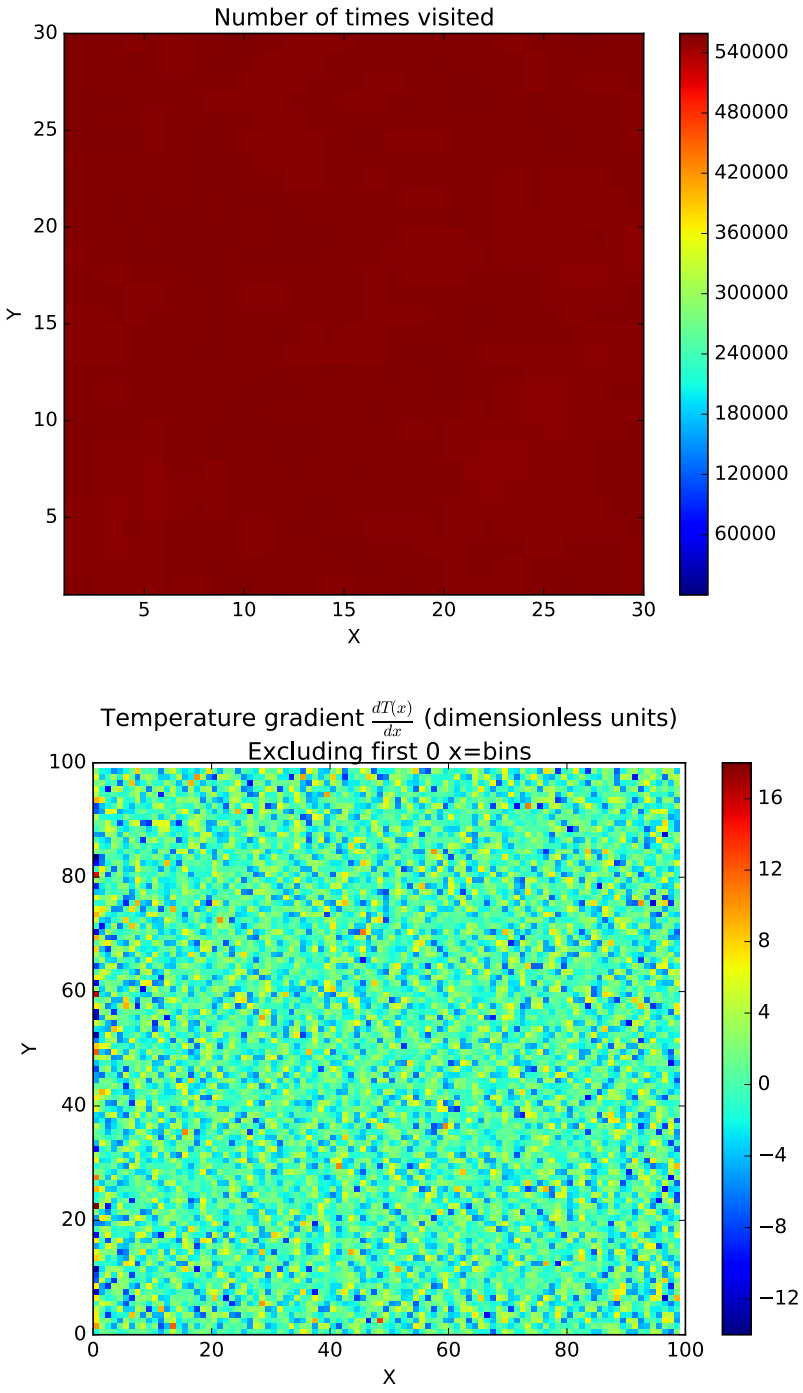

Figure 22: Above-Histogram of walker positions during a 2D *rules test* simulation, illustrating that the walker rules follow the principle of detailed balance, or that all sites are visited equally. This simulation had a box size of 30x30x30, tube length 15, with 4.86×10^8 total walkers used. Below-dT(x)/dx directly from the histogram, which has mean 0.

4.2.2 Coding/computational details about code package 'PRTCNT'

On-lattice random walk simulations are ideal applications for use on multi-core machines such as OU's supercomputer Schooner which was where these simulations were run. Options are given on the command line.

MPI code is run with "mpirun -np X python mpi_run.py" with X the number of cores available. On OU's Schooner, this line must be added to your .profile or specified in the job scheduler (SLURM) submission script: module load OpenMPI mpi4py numpy matplotlib. Those are the dependencies required for Python. MPI4PY should be installed regardless of whether you are using many cores or just one.

Random walks lend themselves to parallelism as each walker is independent and so can be run on its own core. Here's an example of how much of a speedup can be expected. For example, for a 2D run with 100x100 box dimensions with 25000 timesteps and 50000 walkers: Macbook Air with Intel Core i7 serial (1 core) – 160 minutes, Macbook Air with Intel Core i7 parallel (2 cores) – 90 minutes, 80 cores on OU's Schooner – 4 minutes, a 40x speedup.

In order to provide the parallel speedup, I use "barriers" which make unused cores wait, then I run a random walk on each core. I then use "gathers" to collect the data from each core back to the primary core, core 0.

4.3 Results

We will start by defining the reduced thermal conductivity $\frac{k-k_0}{k_0}$, which allows for comparison to experimental data. k_0 is defined as the vacuum thermal conductivity. It can be shown analytically that $k = \frac{1}{300}$ for a 3D symmetric random walk with one reflective and two periodic boundary conditions & within a cube. We also define L/s as

the ratio of the tube length to the box length (100).

First let us look at comparing the results between the non-functionalized and functionalized cases (Figure 23, Figure 24, Figure 25). We can directly observe the improvement from functionalizing the ends at low P_{m-cn} values for both horizontal and random orientations.

Now let us look at the Δk vs. P_{m-cn} plots (Figure 26, Figure 27). These were created by first plotting the reduced thermal conductivity with respect to the CNT volume fraction (0% to 20%). A linear fit was applied to get the slope, as the data was sufficiently linear, and the slopes for the functionalized CNTs was subtracted by the thermal conductivity slope of the pristine CNTs. We will define this as Δk, the change in thermal conductivity slope due to the CNTs. Due to the CNTs, the primary trend is that $k \propto nl$, where n is the number of CNTs in the material and l is the CNT length.

We notice the highest improvement in the horizontally aligned CNTs and a moderate improvement in the randomly aligned CNTs. We see almost no improvement for the vertically aligned CNTs, as expected.

In order to generate the colormap plots (Figure 30), weighted linear fits were applied to the Δk vs. P_{m-cn} plots. These figures offer a succinct picture of the results of this paper; we see that longer tube lengths provide a higher improved thermal conductivity, and the horizontally aligned CNTs show an increase as high as 6 units for L/s=0.2. They also summarize the idea of how much Kapitza resistance impacts the improvement from functionalization. As P_{m-cn} approaches zero, we see that

functionalizing the ends leads to a substantially increased thermal conductivity, and as P_{m-cn} approaches one, functionalizing the ends makes almost no difference. This should give experimentalists an idea of what they should expect to find in their results.

The results from the tunneling models should not be compared to that of the Kapitza models, as the models are significantly different. However, results between the tunneling with volume and tunneling without volume are shown in Figure 28. We can directly see how much the excluded volume affects the thermal conductivity this way. The inert CNT volume restricts the propagation of the phonons throughout the material, thus hindering the thermal conductivity.

If we define the volume fraction of the tunneling no volume model to be only the two endpoints, then around 20 % filling fraction we begin to see phase transition like behavior. This means we are approaching the percolation threshold of the material. In the given figures the volume fractions are set to the full tube lengths to allow comparison.

For all simulations, 5 different configurations of randomly dispersed CNTs were run & averaged over. 2D results are given in Appendix B. Error bars are generated from the covariance matrix in the case of the bar graphs, and from the standard deviation of the mean between the 5 configurations for the plots of thermal conductivity vs. CNT volume fraction or CNT volume percent.

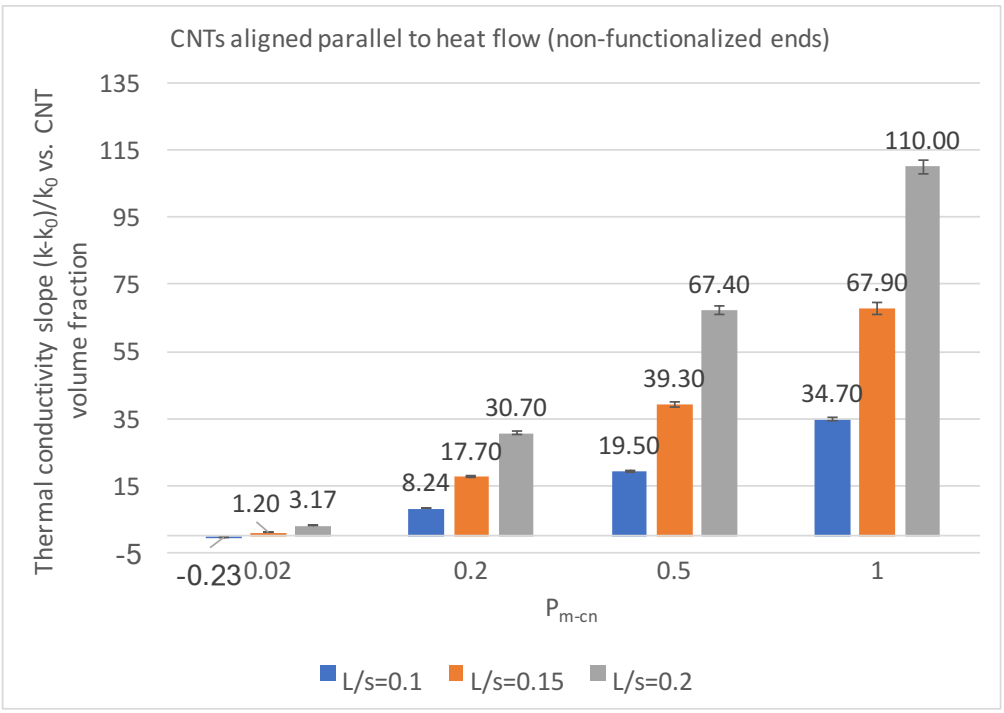

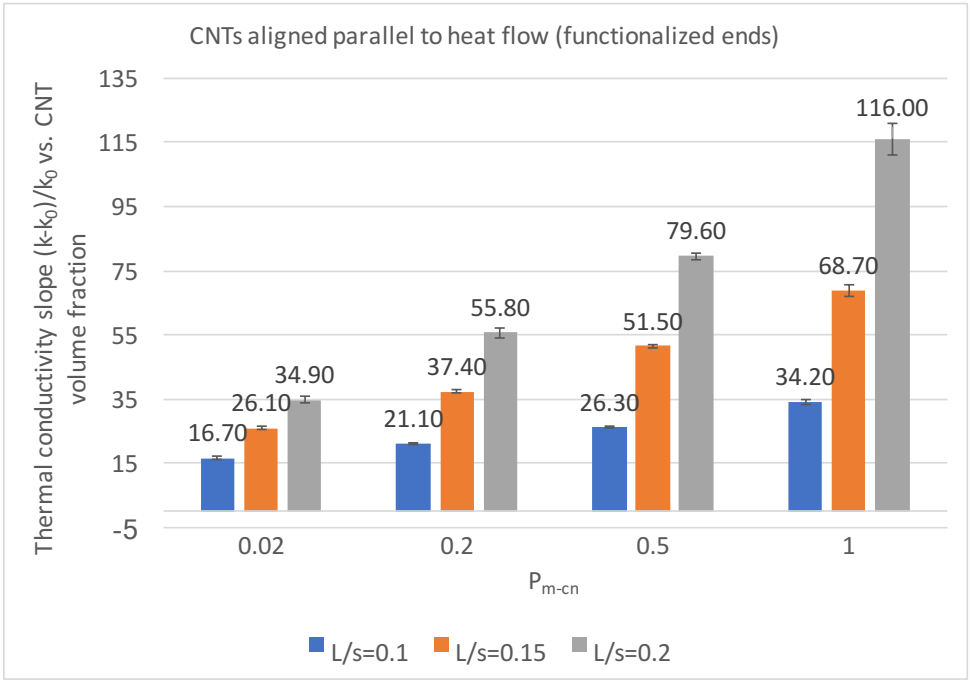

Figure 23: Slopes of linear fits to thermal conductivity (dimensionless) vs. CNT filling fraction plots for CNTs aligned parallel to heat flow (horizontal WRT x-axis) for P_{m-cn}=0.02, 0.2, 0.5, 1.0 and tube lengths 10, 15, 20 in a 100x100x100 3D simulation box. Top-CNTs without end functionalization. Bottom-CNTs with end functionalization.

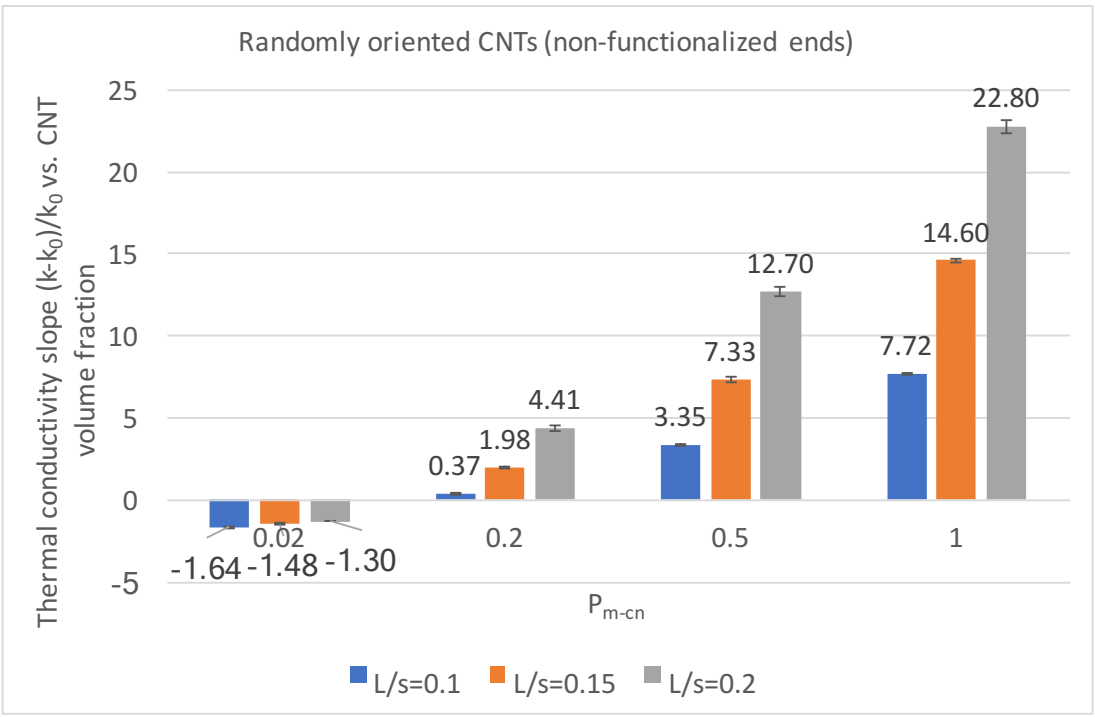

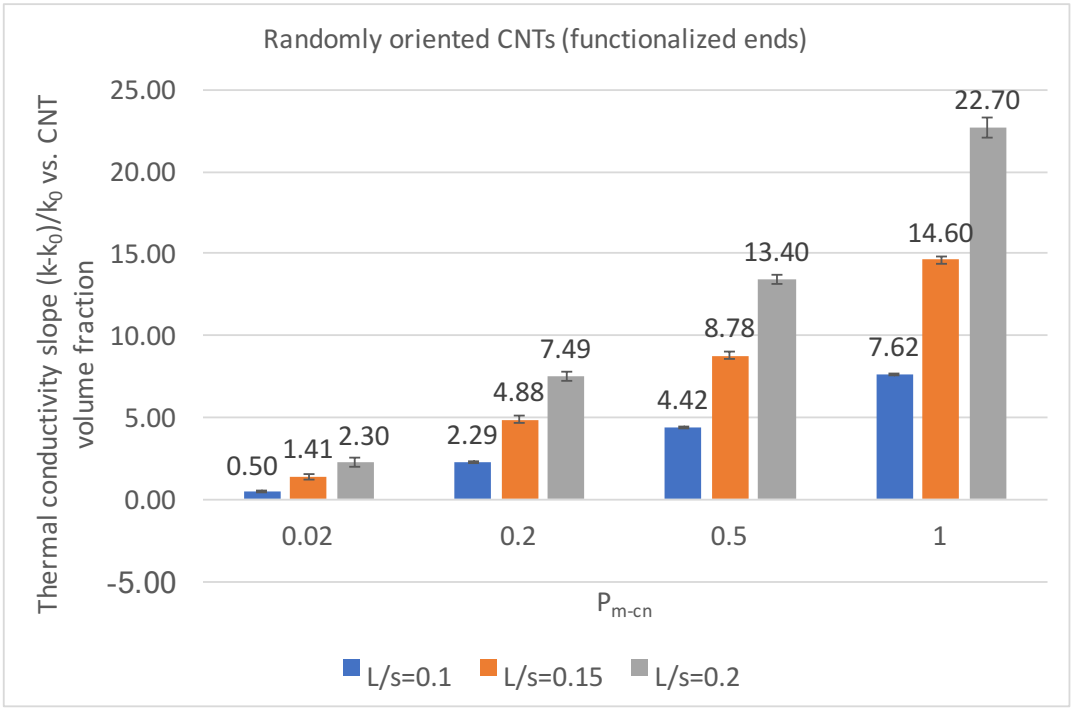

Figure 24: Slopes of linear fits to thermal conductivity (dimensionless) vs. CNT filling fraction plots for CNTs aligned randomly to heat flow for P_{m-cn}=0.02, 0.2, 0.5, 1.0 and tube lengths 10, 15, 20 in a 100x100x100 3D simulation box. Top-CNTs without end functionalization. Bottom-CNTs with end functionalization.

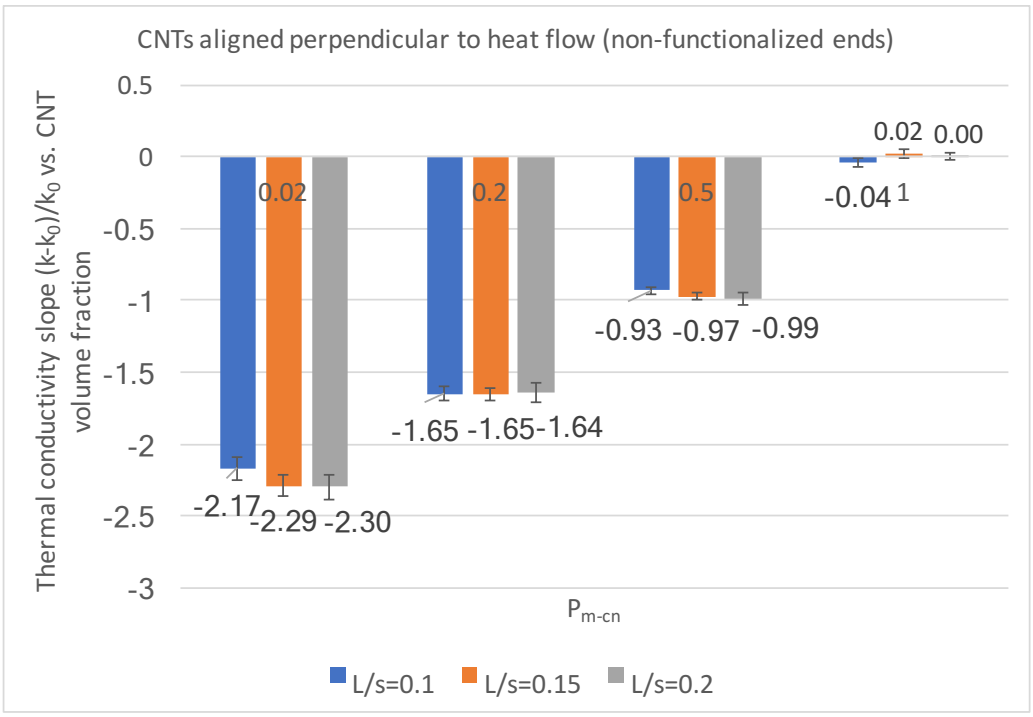

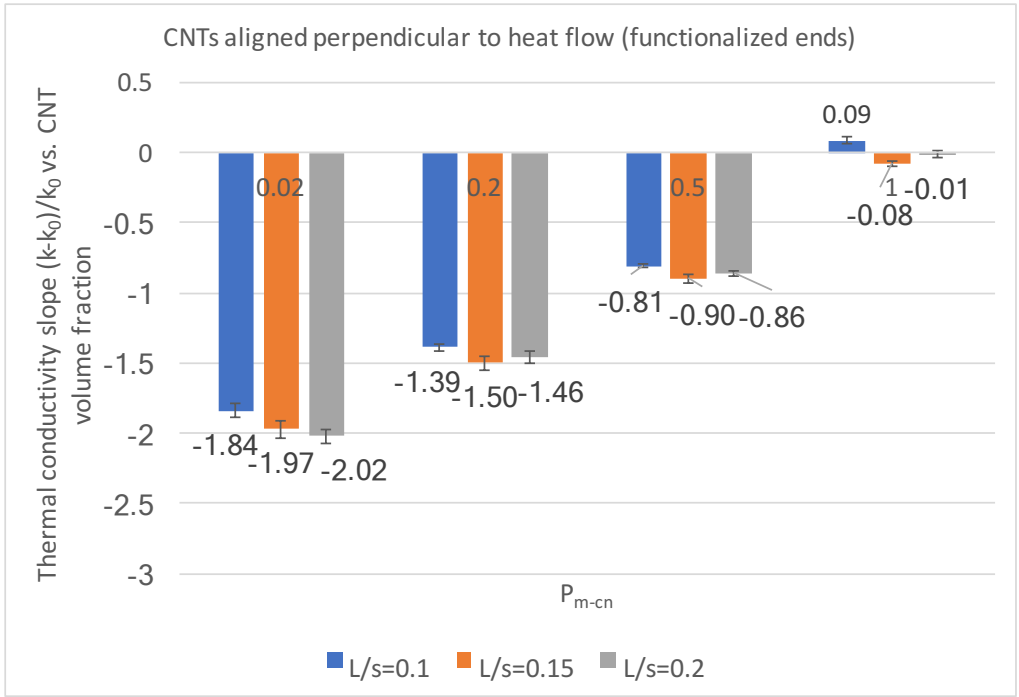

Figure 25: Slopes of linear fits to thermal conductivity (dimensionless units) vs. CNT filling fraction plots for CNTs aligned perpendicular to heat flow (vertical WRT x-axis) for $P_{m\text{-}cn}$=0.02, 0.2, 0.5, 1.0 and tube lengths 10, 15, 20 in a 100x100x100 3D simulation box. Top-CNTs without end functionalization. Bottom-CNTs with end functionalization.

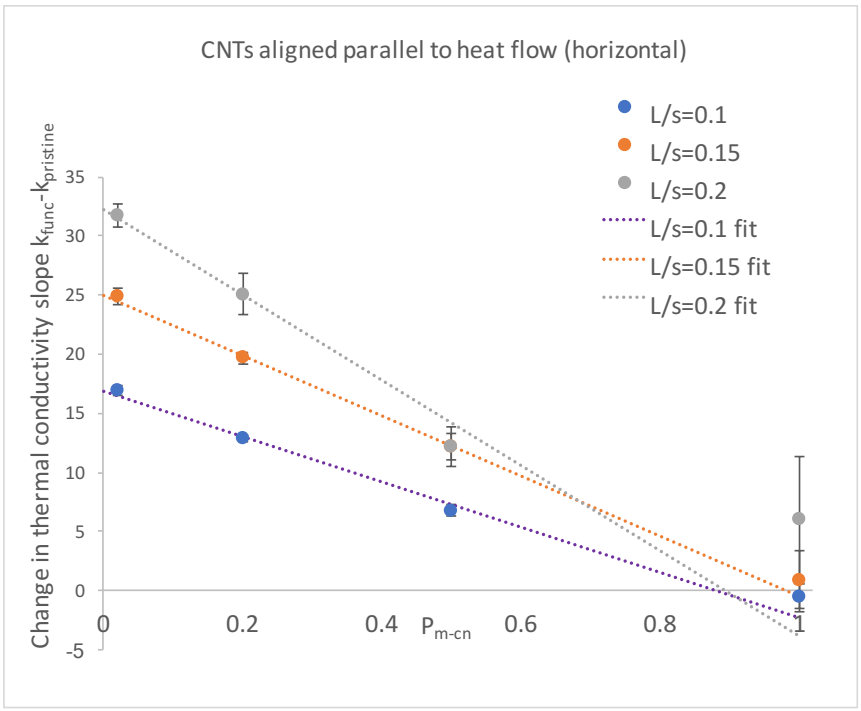

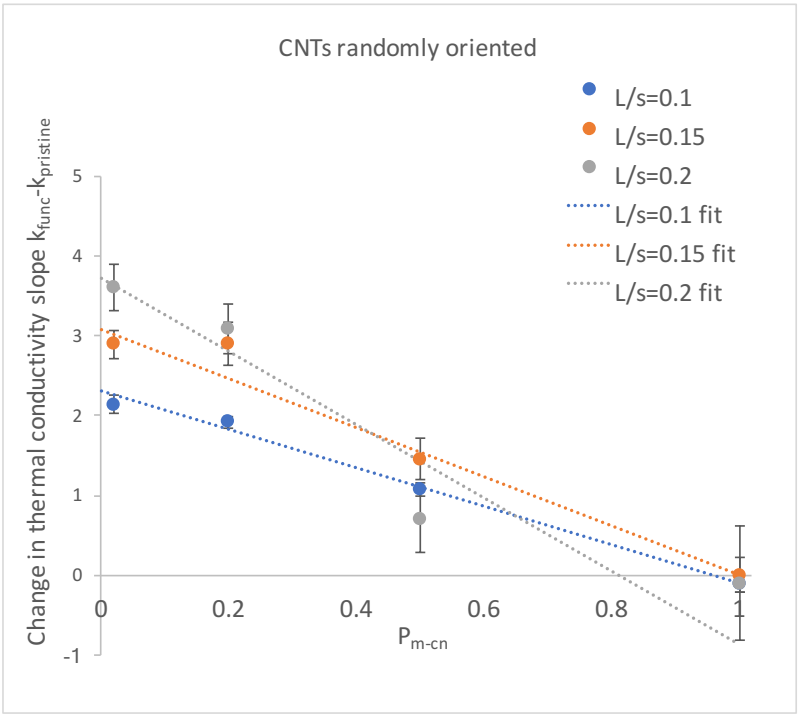

Figure 26: Change in thermal conductivity slope after CNT end functionalization vs. probability for a phonon (walker) to enter a CNT (P_{m-cn}), for tube lengths 10, 15, 20 in a 100x100x100 3D simulation box. Above-CNTs aligned parallel to the heat flow (horizontal WRT x-axis). Below-CNTs aligned randomly to the heat flow.

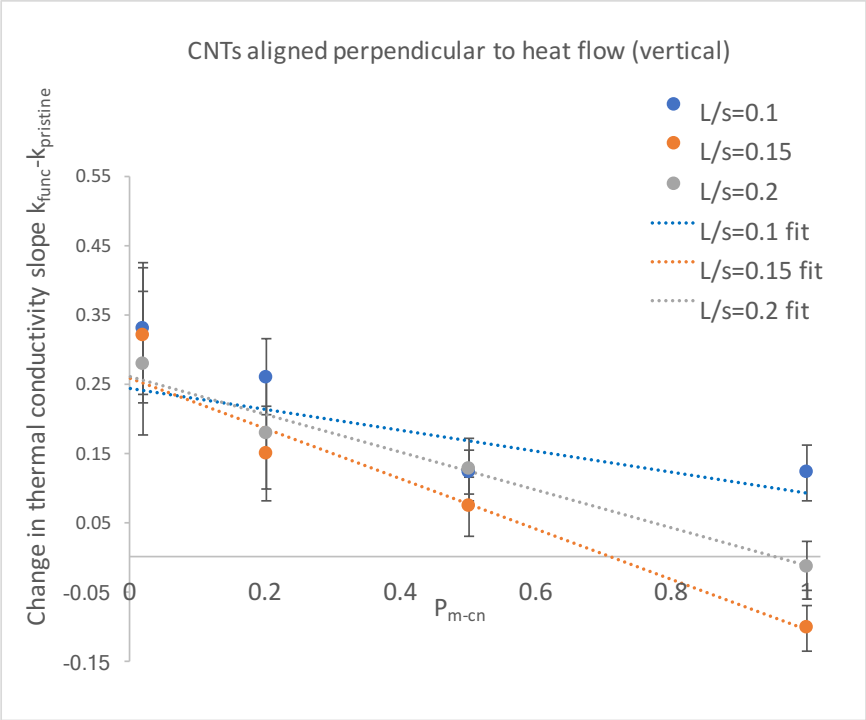

Figure 27: Change in thermal conductivity slope after CNT end functionalization vs. probability for a phonon (walker) to enter a CNT (P_{m-cn}), for tube lengths 10, 15, 20 in a 100x100x100 3D simulation box. CNTs aligned perpendicular to the heat flow (vertical WRT x-axis).

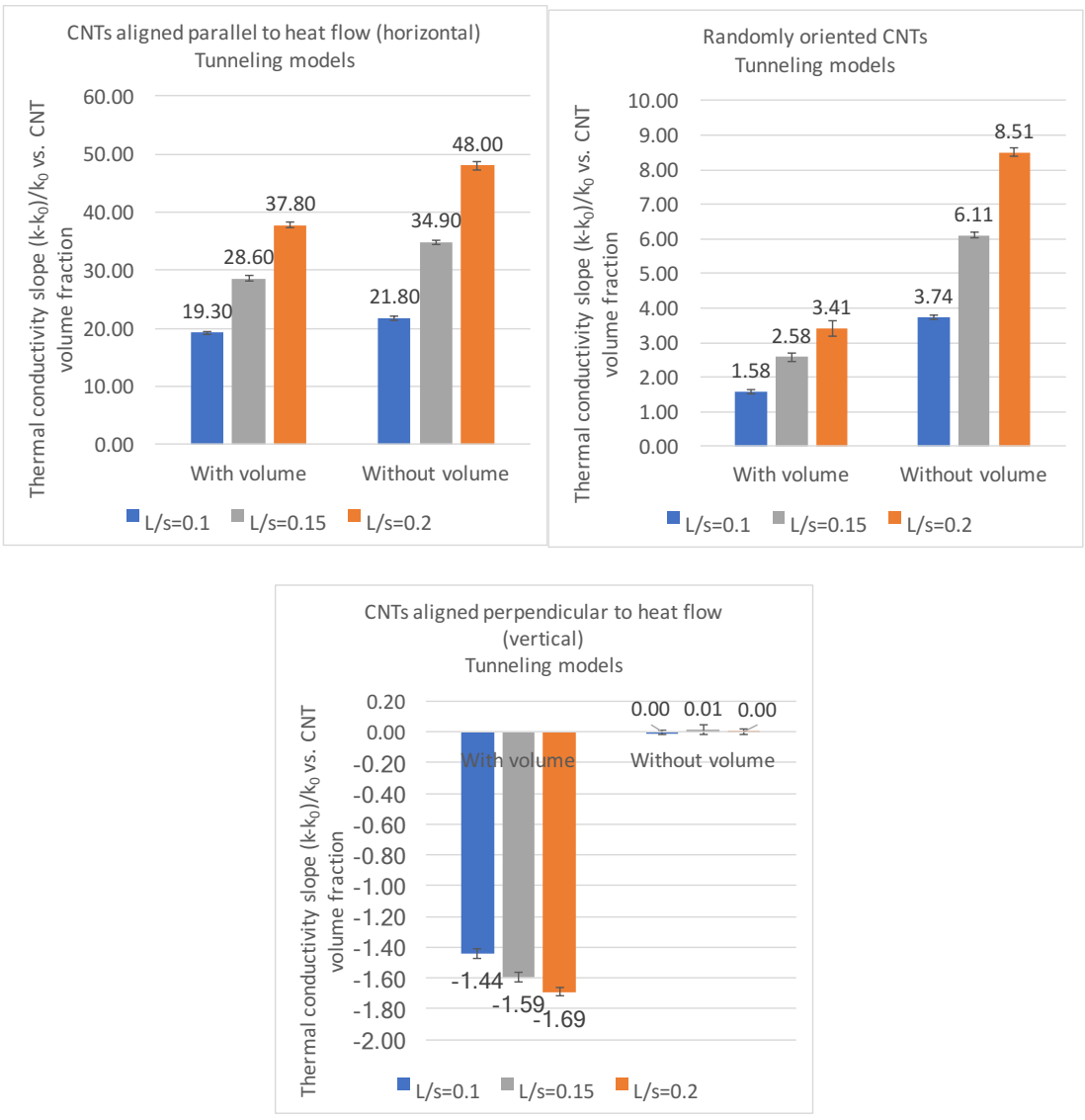

Figure 28: Slopes of linear fits to thermal conductivity (dimensionless) vs. CNT filling fraction plots for all orientations and tube lengths 10, 15, 20 in a 100x100x100 3D simulation box (tunneling models).

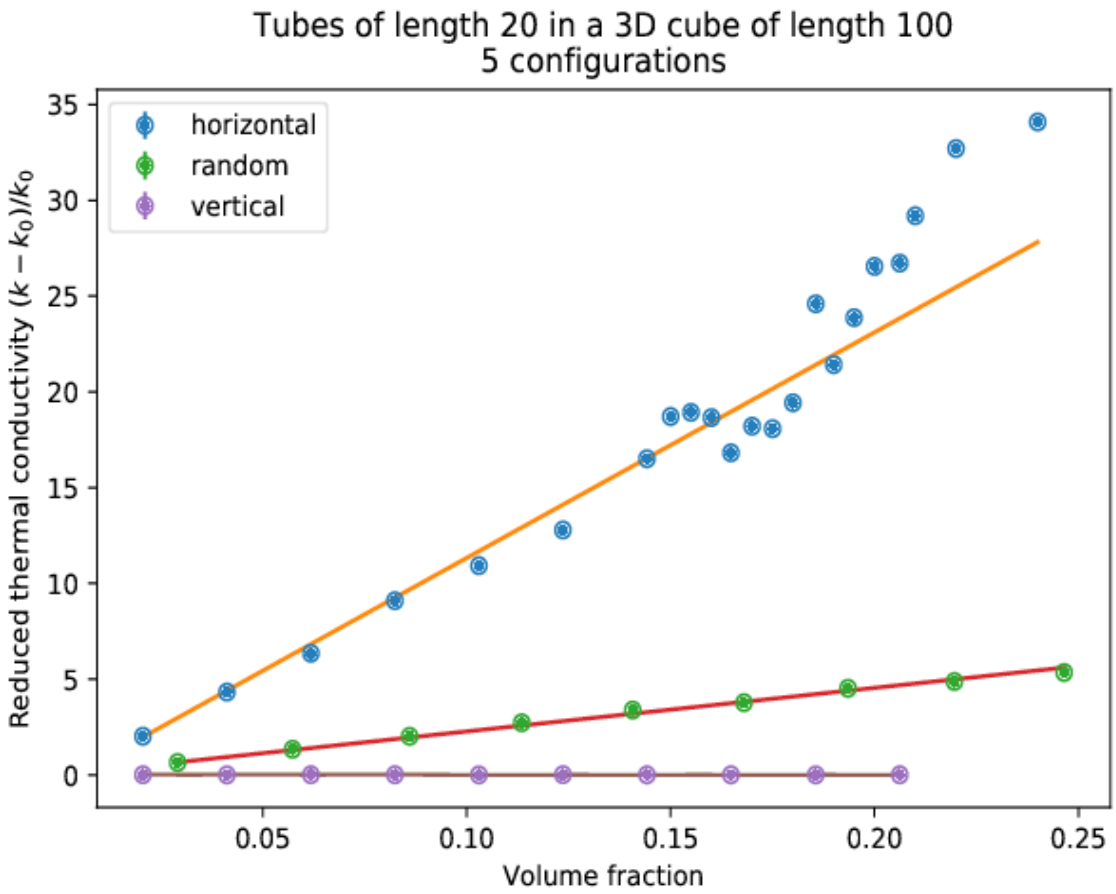

Figure 29: Plot of reduced thermal conductivity $(k-k_0)/k_0$ vs. volume fraction for 3D Kapitza model with functionalization, $P_{m-cn}=1$. Fits for CNTs randomly, horizontally, and vertically oriented to the direction of heat flow in a 100x100x100 simulation box are given. Error bars are too small to be seen. Notice the deviation of linear behavior for the horizontal orientation starting around 18%; this is phase transition like behavior.

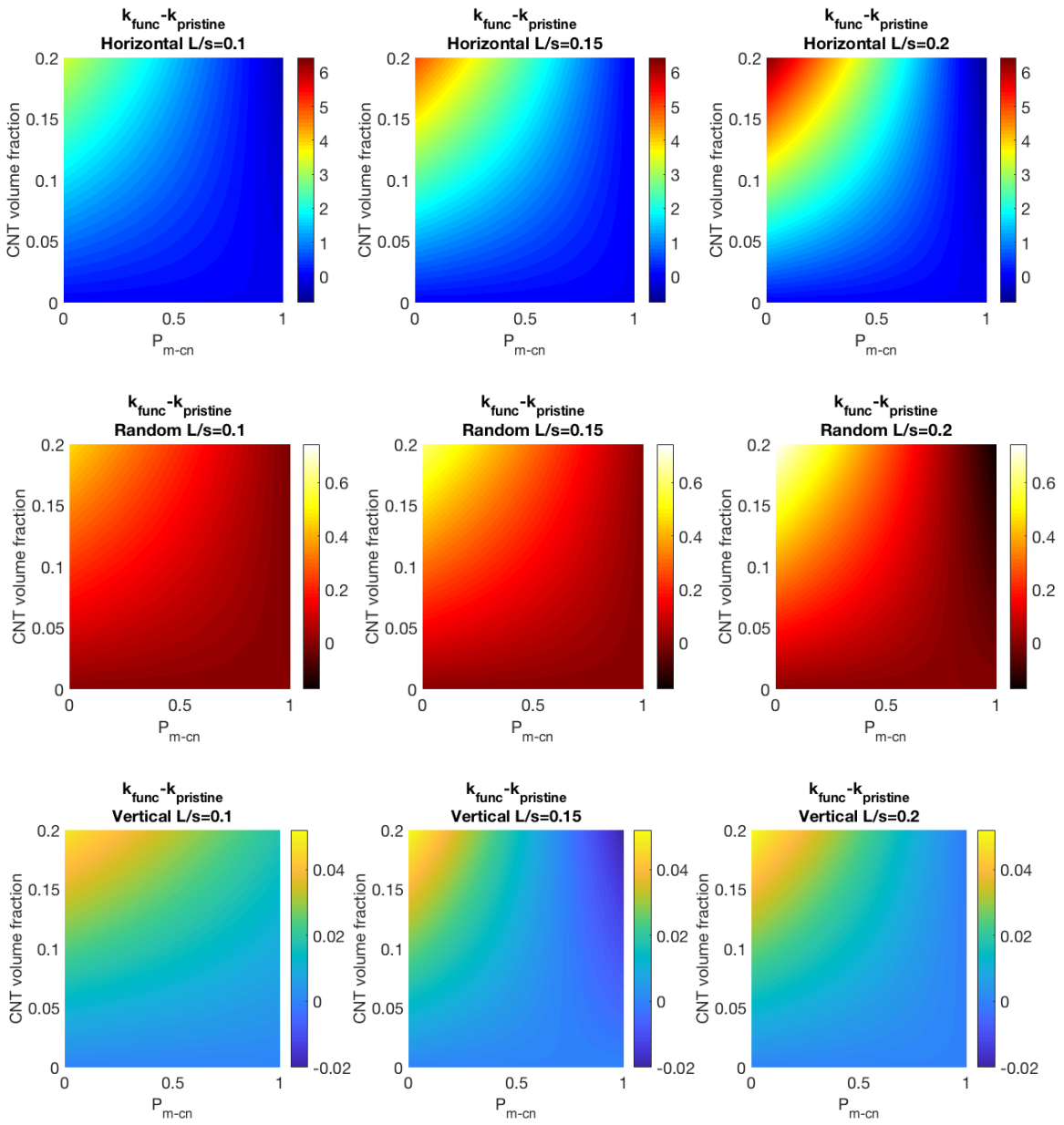

Figure 30: Colormaps for horizontal, random, and vertical orientations in 3D depecting the improvement of thermal conductivity after end functionalization as the color. Shown on the x-axis is $P_{m\text{-}cn}$, and shown on the y-axis is the CNT volume fraction. These follow what we would expect; if a CNT has a high Kapitza resistance, functionalizing the ends will help a lot, but if a CNT has a low Kapitza resistance, it will not help.

4.4 Discussion

First we see that the horizontal orientation, which is parallel to the heat flow, has the highest thermal conductivity k and the vertical has the lowest. In fact the vertical should not have any improvement which is what we see, and in some cases where Kapitza resistance is high ($P_{m\text{-}cn}$ is low) it actually decreases k. This is expected since the tubes occupy space and exclude volume, reducing free space for walkers or phonons to move. The random orientation is in the middle of both of those for almost all cases.

In Figure 23, Figure 24, and Figure 25 we can see bar graphs of the reduced thermal conductivity vs. CNT filling fraction. This allows the reader to view the improvement directly as a function of functionalizing the ends of the CNT by comparing models without end functionalization to ones with their ends functionalized. Immediately we see improvement after the ends are functionalized for low values of $P_{m\text{-}CN}$, as can be seen by direct comparison. However, this compares the thermal conductivity slope which is not the same as the thermal conductivity itself. Later we will see a more detailed & generalized plot comparing $P_{m\text{-}CN}$ to the CNT volume fraction (Figure 30).

Another important note to make is the absence of a percolation threshold, for all cases except for that seen in Figure 29, which is for a tube length of 20, Kapitza model, horizontal orientation (CNTs aligned parallel to heat flow), and for $P_{m\text{-}CN}=1$. This is not a practical model since this model has a physical value of $P_{m\text{-}CN}=1$. The AMM discussed in Chapter 2: Theory of heat transport gives a formula relating $P_{m\text{-}cn}$ to the thermal boundary resistance R_{bd},

$$P_{m-cn} = 4/\rho C C_m R_{bd} \quad (74)$$

with ρ the matrix density, C the matrix specific heat, and C_m the speed of sound in the matrix [48]. A value for the probability of a walker entering a CNT from the matrix can then be calculated if the thermal boundary resistance is known and simulations run at that value.

In Figure 29 we see a significant deviation in this linear behavior at around 15-20% CNT volume fraction. Extra data points were run at higher CNT volume fraction values to flush out the trend better, and it appears that there is a phase transition present. Since this is only visible for CNTs aligned parallel to the heat flow, and for CNTs without any Kapitza resistance ($P_{m\text{-}cn}$=1), this makes sense as the Kapitza resistance counters any phase transition we would see at a lower $P_{m\text{-}cn}$. Simulations were also run in a box with side lengths of 150 for the same tube lengths as before to see if the phase transition trend would be the same if the ratio of the tube length to box size was constant. It appears that while the phase transition becomes steeper as this ratio increases, plots having the same ratio approximately line up, as we would expect from the scaling hypothesis in phase transition theory.

Given in Appendix D: Experimental apparatuses are images of several laboratory tools used to measure k in the Glatzhofer lab.

Chapter 5: Molecular Dynamics

In this chapter I will explain what molecular dynamics (MD) simulations are, along with the appropriate mathematics, and how different transport properties (such as the thermal conductivity) can be calculated using this technique. Then I will discuss my research and simulation results as it relates to the subject. My MD simulations use the GROMACS (Groningen Machine for Chemical Simulations, http://www.gromacs.org) software package, a program called LAMMPS (Large-scale Atomic/Molecular Massively Parallel Simulator, http://lammps.sandia.gov) and for visualization I primarily use VMD (Visual Molecular Dynamics, http://www.ks.uiuc.edu/Research/vmd/).

5.1 Molecular dynamics (MD) theory

The goal of MD is quite simple: given a system of particles, all potential forces involved, and their positions in space and initial conditions, integrate Newton's equations of motion to compute future positions, velocities, and forces of each particle for as long as your computational resources allow.

$$\boldsymbol{f_i} = m_i \ddot{\boldsymbol{r}}_i \qquad \boldsymbol{f_i} = -\frac{\partial U}{\partial r_i} \tag{75}$$

f_i denotes the forces acting on particle I, U is the potential energy force field (model-dependent), and r_i is the position of particle i. Then by specifying a force field, the problem is in theory solved. By knowing these quantities, transport coefficients for the system can be calculated from statistical mechanics. These are very useful for the applied physicist or chemical engineer who wishes to run computational fluid dynamics (CFD) on the same system and lacks transport coefficients.

MD simulations allow for a bridge between theory and experiment; they fill in the gaps that experiment cannot easily access and vice versa. Note that this is known as *classical* MD. For systems with significant quantum effects (such as a low-temperature quantum harmonic oscillator), quantum MD or more rigorous methods such as time dependent (TD) Hartree-Fock or TD density functional theory (TDDFT) are needed.

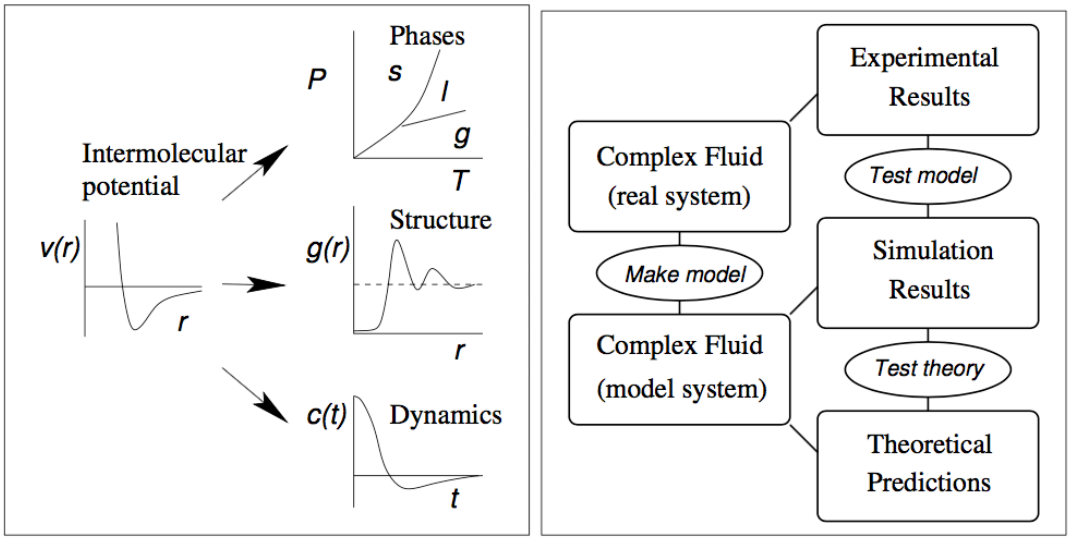

Figure 31: Left-MD simulations can relate macroscopic to microscopic quantities. Right-Theory and experiment working together to solve a research problem [51]**.**

A MD potential energy force field is built using both theory and experimental data. These are freely available for researchers in very diverse areas, from biophysics to polymer research. I use the AMBER force field for my simulations (http://www.ambermd.org). Next I will explain the common terms in one of these force fields.

A MD force field is made up of covalently bonded forces and non-covalently bonded forces.

$$U_{tot} = U_{non-bonded} + U_{bonded}$$

$$U_{non-bonded} = U_{LJ} + U_{Coulomb} \quad (76)$$

$$U_{bonded} = U_{bonds} + U_{angles} + U_{dihedrals}$$

THE GLOBAL MD ALGORITHM

1. Input initial conditions

Potential interaction V as a function of atom positions
Positions $\boldsymbol{r}$ of all atoms in the system
Velocities $\boldsymbol{v}$ of all atoms in the system

⇓

repeat 2,3,4 for the required number of steps:

2. Compute forces

The force on any atom

$$\boldsymbol{F}_i = -\frac{\partial V}{\partial \boldsymbol{r}_i}$$

is computed by calculating the force between non-bonded atom pairs:

$$\boldsymbol{F}_i = \sum_j \boldsymbol{F}_{ij}$$

plus the forces due to bonded interactions (which may depend on 1, 2, 3, or 4 atoms), plus restraining and/or external forces.
The potential and kinetic energies and the pressure tensor may be computed.

⇓

3. Update configuration

The movement of the atoms is simulated by numerically solving Newton's equations of motion

$$\frac{\mathrm{d}^2 \boldsymbol{r}_i}{\mathrm{d}t^2} = \frac{\boldsymbol{F}_i}{m_i}$$

or

$$\frac{\mathrm{d}\boldsymbol{r}_i}{\mathrm{d}t} = \boldsymbol{v}_i; \quad \frac{\mathrm{d}\boldsymbol{v}_i}{\mathrm{d}t} = \frac{\boldsymbol{F}_i}{m_i}$$

⇓

4. if required: **Output step**
write positions, velocities, energies, temperature, pressure, etc.

Figure 32: The global MD algorithm [52].

This is the most common way to define a force field. I will explain the non-bonded terms first. Non-bonded in this sense refers to interactions that apply to all atoms within a simulation. The Lennard-Jones (LJ) term accounts for the N-body potential, and is attractive beyond a defined radius and repulsive inside of that radius.

$$U_{LJ}(\boldsymbol{r_{ij}}) = 4\epsilon_{ij}\left(\left(\frac{\sigma_{ij}}{r_{ij}}\right)^{12} - \left(\frac{\sigma_{ij}}{r_{ij}}\right)^{6}\right) \quad \textbf{(77)}$$

ε is the well depth, and σ is the well diameter (see figure 34a), both determined empirically for the interaction between atoms i and j.

The Coulomb (electrostatic) interaction is given by

$$\boldsymbol{U_{Coulomb}} = {}^{1}\!/_{4\pi\epsilon_0}\frac{q_i q_j}{\epsilon_r r_{ij}^2}\frac{\boldsymbol{r_{ij}}}{r_{ij}} \quad \textbf{(78)}$$

This term is only present if there are ions or charges on any of the atoms or if modeling electrostatics is important.

The non-bonded terms apply to all atoms in a simulation (within a cutoff distance) and turn on and off throughout the simulation. The bonded terms are determined before the simulation starts by a cutoff parameter and do not turn off (5 Å is typical).

$$\begin{aligned} U_{bonded} = {} & \frac{1}{2}\sum_{bonds} k_{ij}^{r}\left(r_{ij} - r_{eq}\right)^2 \\ & + \frac{1}{2}\sum_{angles} k_{ijk}^{\theta}\left(\theta_{ijk} - \theta_{eq}\right)^2 \\ & + \frac{1}{2}\sum_{dihedrals}\sum_{m} k_{ijkl}^{\phi,m}\left(1 + \cos\left(m\phi_{ijkl}\right) - \gamma_m\right)\end{aligned} \quad \textbf{(79)}$$

The “bonds” reflect the structure of the system, and are the stretching terms between two atoms i and j. As one can see, the “harmonic” assumption has been made (only keep 2nd order term from the polynomial expansion) so the timescales must be appropriate to the distance between the atoms for it to yield correct results.

The “angles” occur between 3 atoms in the same plane. The angle is between atoms 1 and 3, with atom 2 defined as the origin for the calculation.

The “dihedrals” or torsion angles occur between 4 atoms, and it is the angle between two planes, as shown in Figure 33.

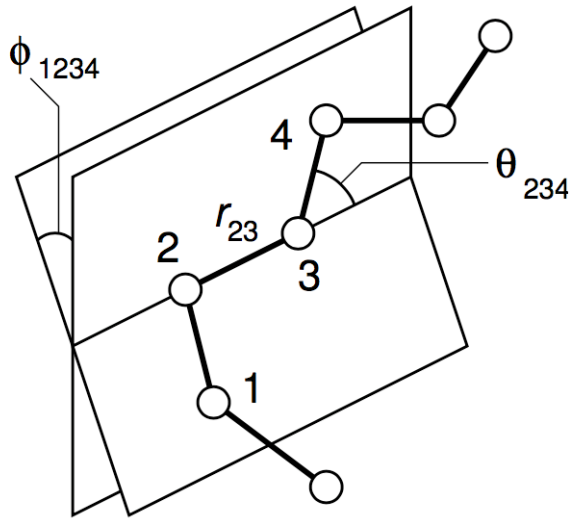

Figure 33: Picture showing the dihedral angle ϕ along with the atoms [51]**.**

They may be proper (most common) or improper dihedrals. Improper dihedrals may use a different expression than given above, as they are intended to keep planar groups linear (aromatic rings) or prevent a molecule from flipping over into its reverse image [52].

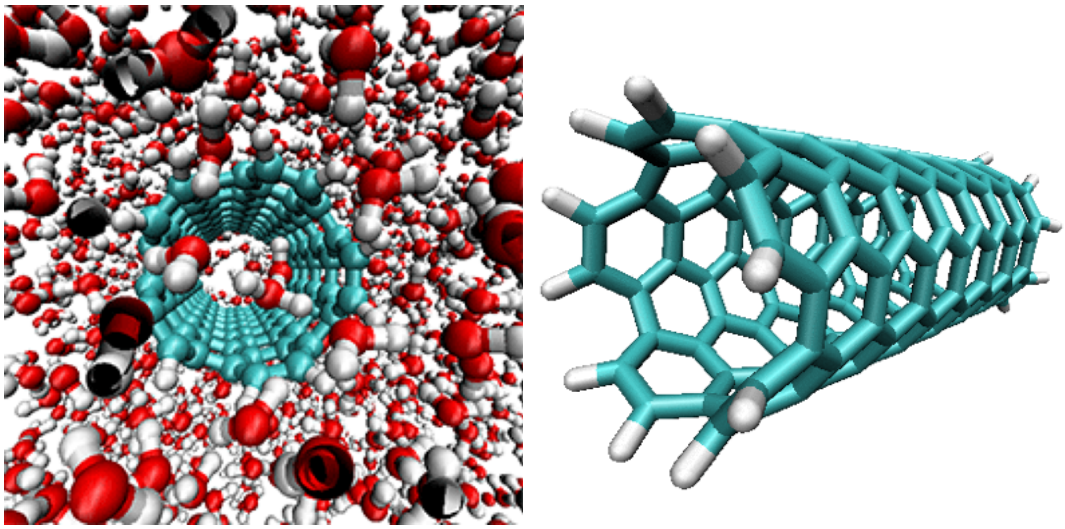

Figure 34: Left-Picture of a carbon nanotube-water nanofluid MD simulation, Right-"Armchair" CNT with hydrogen atoms attached to the ends. Both generated using VMD.

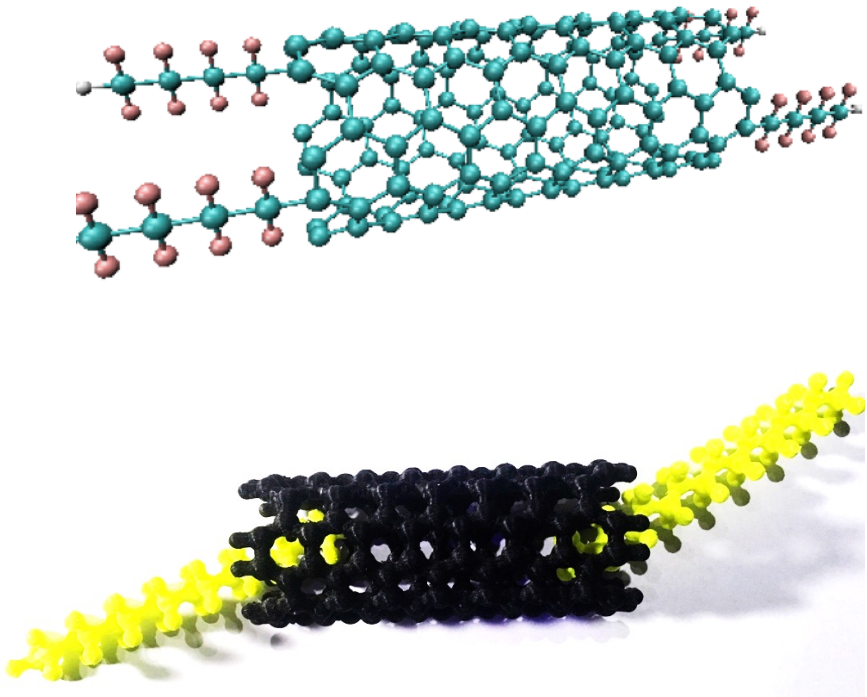

Figure 35: Carbon nanotube with Teflon™ (polytetrafluoroethylene) molecules attached to the ends. Above-unrelaxed MD structure. Generated using VMD. Below-3D printed model of same structure lacking one sidechain on each end.

Molecular dynamics is such a vast topic it would be impossible to cover all of it in a short introduction. As I explain how thermal conductivity calculations may be computed for my systems, I will introduce relevant terms & concepts.

5.2 Simulation methods

The specific details for how I implemented my MD simulations can be found in Appendix C: LAMMPS thermal conductivity code example. I begin by defining several variables for unit conversion, then I energy minimize the structure using the conjugate gradient method. Once that is performed I run the relaxed structure in the canonical ensemble (constant number of particles, temperature, and pressure (NVT)), with thermostats applied to all atoms in order to have the system in thermodynamic equilibrium. The specific method I use to integrate Newton's equations of motion (Langevin equation) is a standard velocity-Verlet numerical integrator [53]. The thermostats are Nose-Hoover type (non-Hamiltonian) which after integration generate positions and velocities appropriate to the canonical ensemble [54]. Specific details about these methods may be found in the LAMMPS documentation.

Once the system stabilizes I turn off the thermostats, thereby switching the ensemble to microcanonical (constant NVE). I then use equation (94) and the equilibrium MD Green-Kubo method I discuss in the next section to compute the thermal conductivity. After running the system and observing the dissipation of the fluctuations in the heat flux, the heat flux autocorrelation function converges to yield a

value for the thermal conductivity. A schematic of this process is shown in Figure 36.

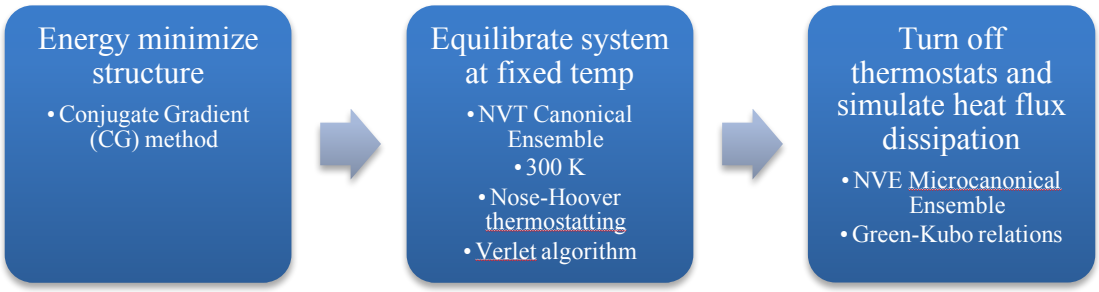

Figure 36: Diagram showing the process used in LAMMPS to compute thermal conductivity.

5.3 Using Green-Kubo relations to obtain thermal conductivity

The Green-Kubo relations (or method) relate a system's transport coefficients (such as thermal/electrical conductivity and viscosity) to integrals of time correlation functions [55].

$$\gamma = \int_0^\infty < \dot{A}(t)\,\dot{A}(0) > dt \qquad (80)$$

They were first derived by Green (in 1954) and Kubo (in 1957) [56], and I will derive these relations next.

If no velocity gradient exists, the internal energy per unit volume follows a continuity equation, $\frac{\rho dU}{dt} = -\nabla \cdot J_Q$. Fourier's law of heat conduction is $J_Q = -\lambda \nabla^2 T$, and combining these two equations together gives [57]

$$\rho \frac{dU}{dt} = \lambda \nabla^2 T \qquad (81)$$

A small perturbation on the left hand side of equation (81) can be written as $(\rho + \Delta\rho)d(< U > + \Delta U)/dt$. Since d <U>/dt=0, to first order we have $\frac{\rho d\Delta U}{dt}$, and the spatial gradient of <T> also doesn't contribute, so we can write

$$\rho \frac{d\Delta U}{dt} = \lambda \nabla^2 \Delta T \quad \textbf{(82)}$$

Now we will relate the temperature variation ΔT to the variation in energy per unit volume $\Delta(\rho U)$ using

$$\frac{1}{V}\frac{\partial E}{\partial t}|_V = \frac{\partial(\rho U)}{\partial t}|_V = \rho c_V \quad \textbf{(83)}$$

with c_V being the specific heat per unit mass. A slight variation of the temperature ΔT is equal to $\Delta(\rho U)/\rho c_V$. Then we can write

$$\rho \Delta U = \frac{\lambda}{\rho c_V} \nabla^2 \rho \Delta U \quad \textbf{(84)}$$

Letting $D_T \equiv \lambda/\rho c_V$ be the thermal diffusivity, the terms of the wave vector-dependent internal energy density equation become

$$\rho \Delta U(k,t) = -k^2 D_T \rho \Delta U(k,t) \quad \textbf{(85)}$$

Defining the wave vector dependent internal energy density autocorrelation function C(k,t) as

$$C(k,t) = < \rho \Delta U(k,t) \rho \Delta U(-k,0) > \quad \textbf{(86)}$$

The frequency and wave vector dependent diffusivity is the memory function of the autocorrelation function.

$$\tilde{C}(k,\omega) = C(k,0)/i\omega + k^2 \widetilde{D}_t(k,\omega) \quad \textbf{(87)}$$

This equation can be converted in terms of the diffusivity in terms of a current correlation function. If $\phi = -d^2C/dt^2$, we have

$$\phi(k,t) = k^2 < J_{Qx}(k,t) J_{Qx}(-k,0) > \quad \textbf{(88)}$$

and we can now write the expression as

$$k^2\widetilde{D}_T(k,\omega) = \frac{C(k,0) - i\omega\tilde{C}(k,\omega)}{\tilde{C}(k,\omega)} = \frac{\tilde{\phi}(k,\omega)}{C(k,0) - \frac{\tilde{\phi}(k,\omega)}{i\omega}} \qquad (89)$$

With the equation $\phi(k,t) = k^2 N_Q(k,t)$, the thermal diffusivity may be written as

$$\widetilde{D}_T(k,\omega) = \frac{\widetilde{N}_Q(k,\omega)}{C(k,0) - \frac{k^2}{i\omega}\widetilde{N}_Q(k,\omega)} \qquad (90)$$

We must obtain the zero wavevector limit before taking the zero frequency limit. The canonical ensemble fluctuation formula for specific heat is

$$\rho C_V = \frac{C(0,0)}{V k_B T^2} \qquad (91)$$

Using both of these equations, the Green-Kubo relation for thermal conductivity is finally obtained.

$$\kappa = \frac{V}{3k_B T^2}\int_0^\infty < \boldsymbol{J_Q}(0)\cdot\boldsymbol{J_Q}(t) > dt \qquad (92)$$

Deriving the Green-Kubo relation for viscosity is similar to the previous derivation.

$$\eta_V = \frac{1}{V k_B T}\int_0^\infty dt < [p(t)V(t) - < pV >]\,[p(0)V(0) - < pV >] > \qquad (93)$$

These relations have several implications. If we have a thermodynamic system in equilibrium, we may use these relations to obtain these values from molecular dynamics simulations. In order to practically use equation (92), the heat flux autocorrelation function $< \boldsymbol{J_Q}(0)\cdot\boldsymbol{J_Q}(t) >$ must be computed from an atom's forces, velocities, and positions if molecular dynamics is used. The heat flux J_Q can be calculated from the following formulas given from the LAMMPS documentation [58]:

$$J=\frac{1}{V}[\sum_i e_i \boldsymbol{v_i}-\sum_i \boldsymbol{S_i v_i}]$$
$$J=\frac{1}{V}[\sum_i e_i \boldsymbol{v_i}+\sum_{i<j}(\boldsymbol{f_{ij}}\cdot \boldsymbol{v_j})\boldsymbol{x_{ij}}] \quad (94)$$
$$J=\frac{1}{V}\left[\sum_i e_i \boldsymbol{v_i}+\frac{1}{2}\sum_{i<j}(\boldsymbol{f_{ij}}\cdot(\boldsymbol{v_i}+\boldsymbol{v_j}))\boldsymbol{x_{ij}}\right]$$

Where e_i is the per-atom kinetic and potential energy, V is the molecule's volume, v_i is the per-atom velocity, S_i is the stress tensor, f_{ij} is the force particle i exerts on particle j, and x_{ij} is the distance between particles i & j. The first term is a bulk transport term and the second term is due to the interaction force between the particles. Once the heat flux is obtained, the autocorrelation of the heat flux with itself can be computed, yielding the thermal conductivity after multiplying by constants and integrating [58].

It is reasonable due to the fact that Alex and myself use the same force field, we can assume that our results should be comparable. However it seems as though my derivative of the thermal conductivity turns out to be very similar to Alex Kerr's result for the thermal conductivity. It is also reasonable in that Alex's program only drives the last atom in the chain while the LAMMPS code couples to all of them. Therefore my results would be the sum of the thermal conductivity from Alex's Green's function calculation.

5.4 Results

I will now discuss how I used MD simulations to compare with another theoretical model. Alex Kerr, another member of my group, has developed a code package (https://github.com/ajkerr0/kappa) which calculates the thermal conductivity across molecular interfaces. Specific groups to functionalize the ends of a CNT, along with how many repeated units of the group to use, may be chosen and a molecular model built. The precise method is a Green's function method detailed in [59]. While

the method is a good approximation, it does not promise the same precision that MD results, or experimental results for that matter, can provide.

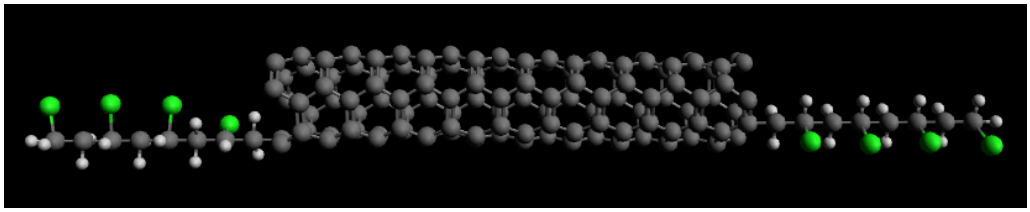

Figure 37: Image of functionalized CNT with Polyvinyl Fluoride (PVF) groups (4 units of the group on each end). Generated using VMD.

Specifically, only bond and angle interactions are used and there is no polymer matrix present. Adding Van der Walls (Lennard-Jones 12-10) interactions and a matrix medium is important as these dictate whether or not the functionalized ends will wrap around the CNT as well as the dynamics of the system.

In equation 93, the autocorrelation is used to compute the thermal conductivity. Autocorrelation is how alike a signal is to a delayed copy of itself as a function of the time lag between them [60]. It can be represented mathematically as

$$R(s,t) = \frac{E[(X_t - \mu_t)(X_s - \mu_s)]}{\sigma_t \sigma_s} \qquad (95)$$

Where E is the expected value operator, the process has mean μ at a time t or s, σ is the standard deviation of the set at time t, and X is a stochastic process at time t. If we allow X to be J (the heat flux), then we can obtain the following plots from simulation. Specifically, LAMMPS was used to obtain the thermal conductivities using the Green-Kubo method previously discussed [58].

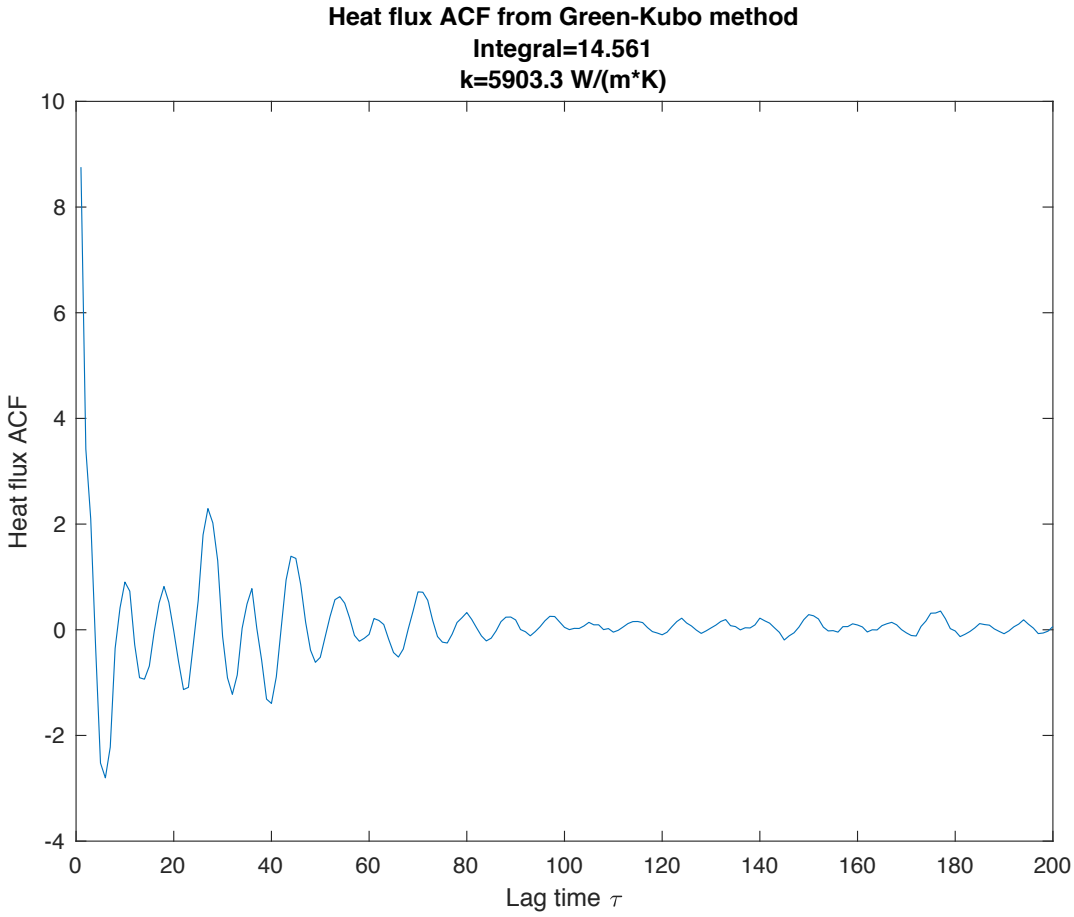

Figure 38: Heat flux autocorrelation function (ACF) vs. lag time for a functionalized CNT.

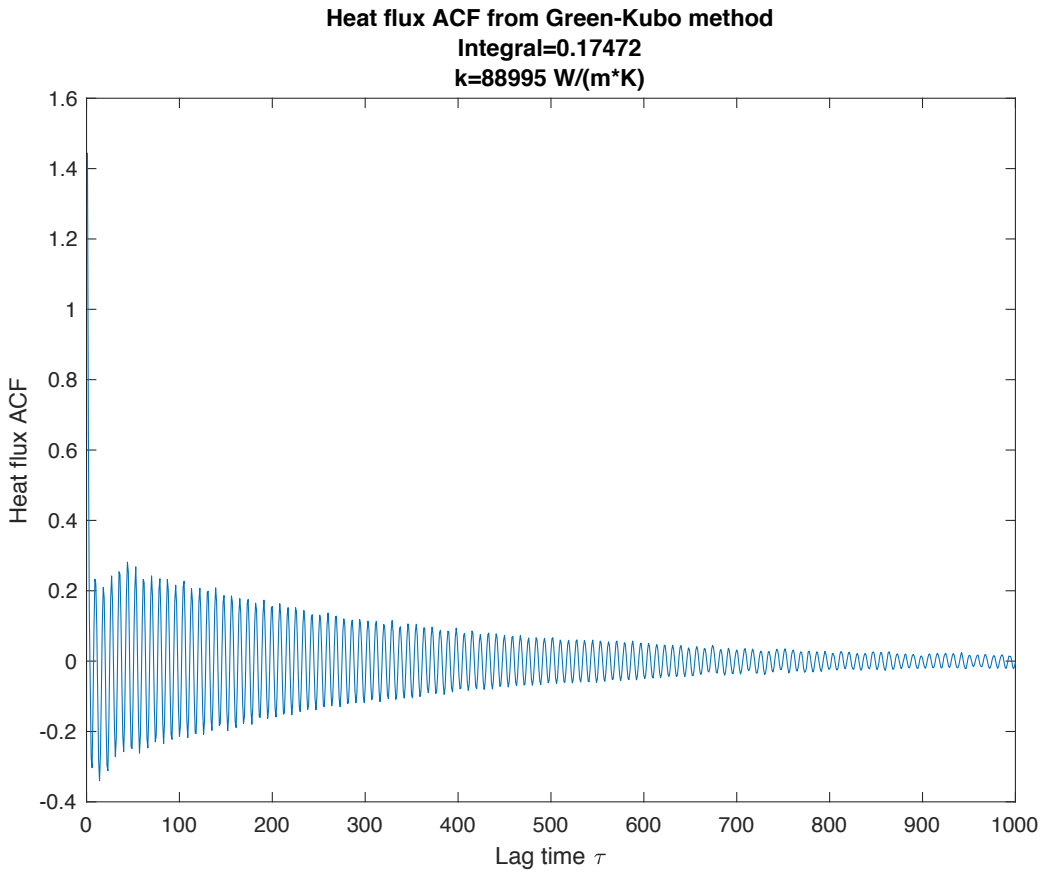

Figure 39: Heat flux ACF vs. lag time for a pristine CNT. Note the resonation at the resonant frequency for the CNT.

As opposed to the random walk method I discussed earlier, the MD method allows one to try exactly a specific group to functionalize a CNT with and compute the thermal conductivity. Figure 40 gives 5 specific groups I will run MD simulations on.

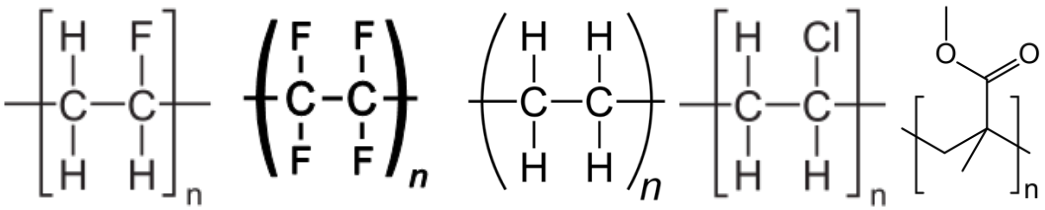

Figure 40: Lewis structures for (from left to right): Polyvinyl fluoride (PVF), Polytetrafluoroethylene (Teflon™), Polyethylene (PE), Polyvinyl chloride (PVC), Poly(methyl methacrylate) (PMMA).

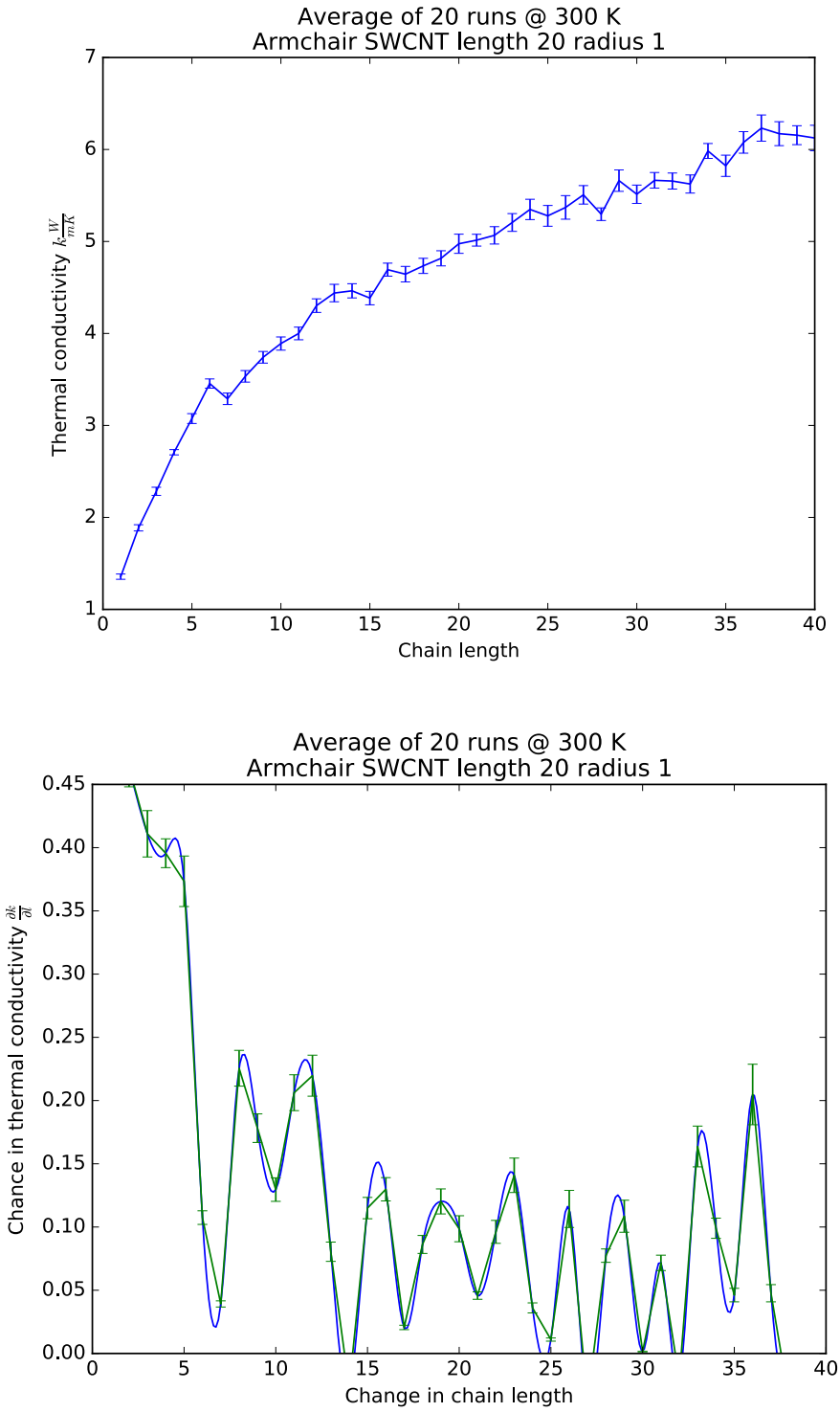

Figure 41: Above-Thermal conductivity measured at CNT interface vs. chain length. Below-Derivative of thermal conductivity measured at CNT interface vs. chain length. One sidechain of PMMA is affixed to each end of the CNT and the number of chains in the polymer are varied. Smoothing has been applied to highlight the oscillations present.

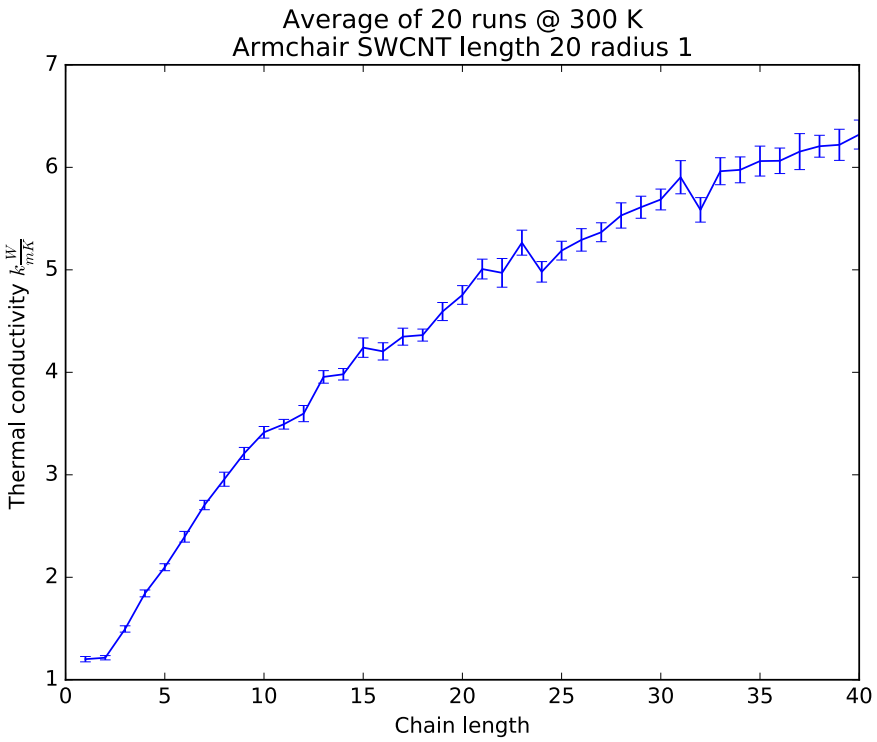

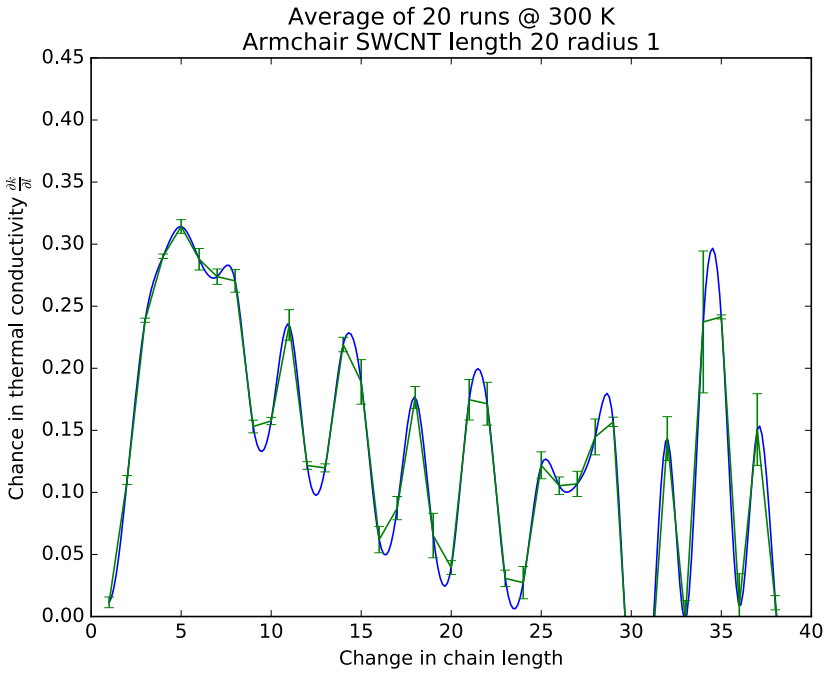

Figure 42: Above-Thermal conductivity measured at CNT interface vs. chain length. Below-Derivative of thermal conductivity measured at CNT interface vs. chain length. One sidechain of PE is affixed to each end of the CNT and the number of chains in the polymer are varied. Smoothing has been applied to highlight the oscillations present.

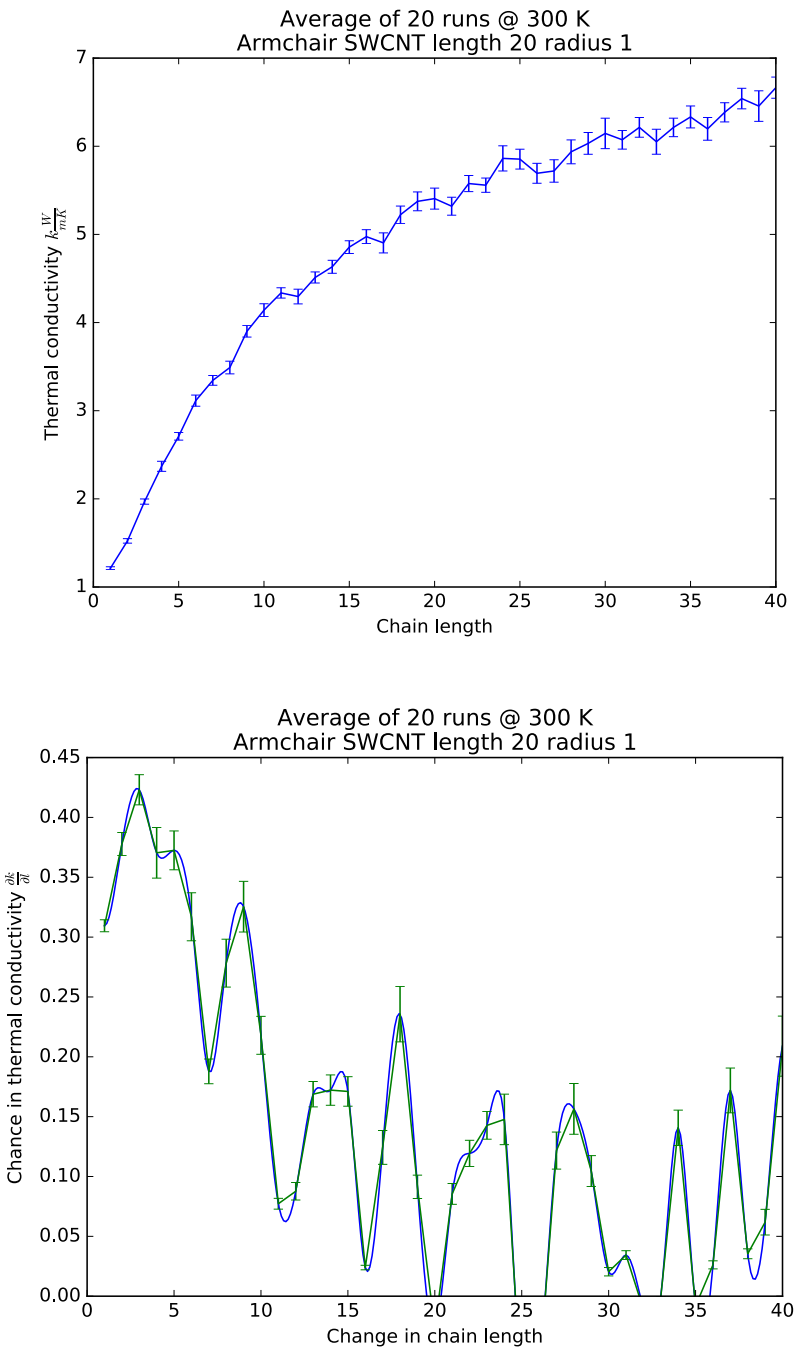

Figure 43: Above-Thermal conductivity measured at CNT interface vs. chain length. Below-Derivative of thermal conductivity measured at CNT interface vs. chain length. One sidechain of PVC is affixed to each end of the CNT and the number of chains in the polymer are varied. Smoothing has been applied to highlight the oscillations present.

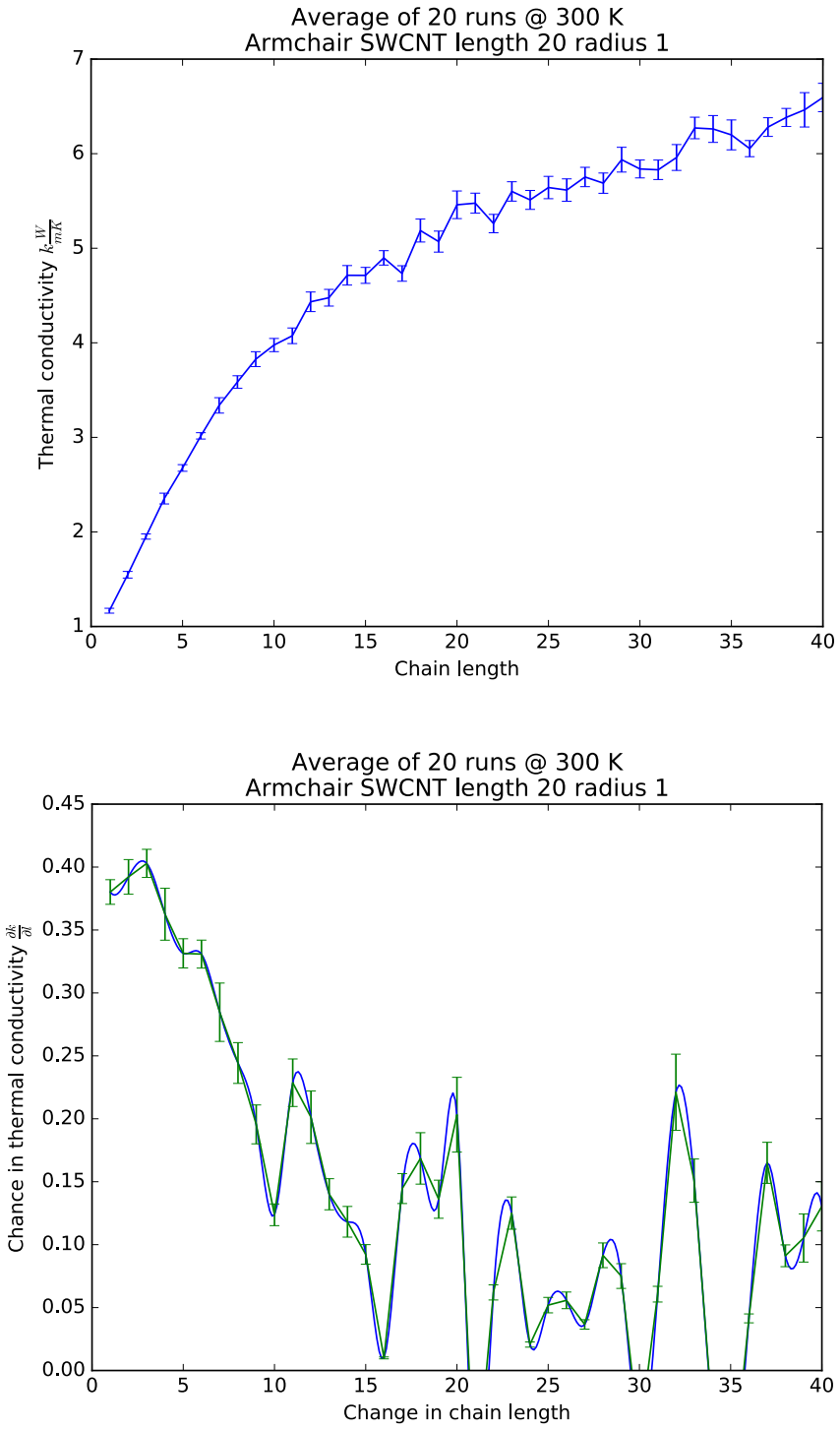

Figure 44: Above-Thermal conductivity measured at CNT interface vs. chain length. Below-Derivative of thermal conductivity measured at CNT interface vs. chain length. One sidechain of PVF is affixed to each end of the CNT and the number of chains in the polymer are varied. Smoothing has been applied to highlight the oscillations present.

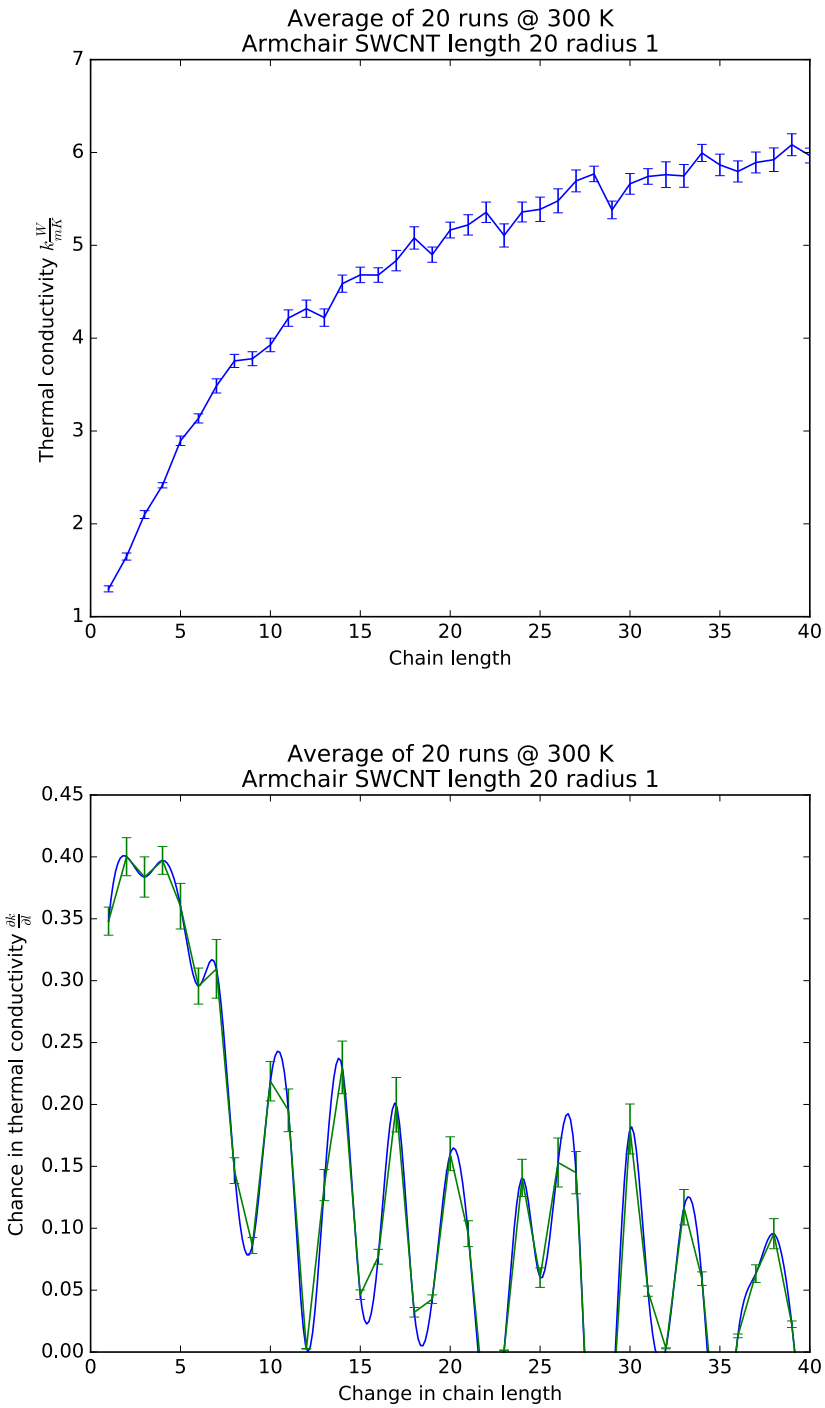

Figure 45: Above-Thermal conductivity measured at CNT interface vs. chain length. Below-Derivative of thermal conductivity measured at CNT interface vs. chain length. One sidechain of Teflon is affixed to each end of the CNT and the number of chains in the polymer are varied. Smoothing has been applied to highlight the oscillations present.

Twenty simulations were run for chains repeated from 1 to 40 on each end of a CNT (length 20 units, radius 1 Å). This means that every plot in Figure 45 required 800 individual simulations. The derivatives are also shown alongside of the thermal conductivity plots, noting an intriguing observation of oscillations present as the chain (or repeated unit) length increases. It's important to note that only the thermal conductivity between the 6 molecules that make up an interface on either end were considered in this calculation. This removes the factor of scaling chain lengths increasing as the thermal conductivity does. However, since it does not define a volume from the interface, the application of comparing the results directly to Alex Kerr's results is uncertain as his describe the total driving power (in force field units). At first glance comparing Figure 45 & Figure 46 show that my derivative for thermal conductivity looks similar to Alex Kerr's thermal conductivity vs. chain length results and his integral of those results match my thermal conductivity results.

It is important to note that both Alex and I use the same force field containing only bonds & angles, which is a good approximation for polymers. It may be the case that integrating Alex's driving power may be the right thing to do to make the proper comparison. However at this point, we are not sure. So far I have run a 1D toy model of balls and springs to compare with Alex's results and the numbers look similar which is promising. We are currently working on ensuring our results are comparable to each other.

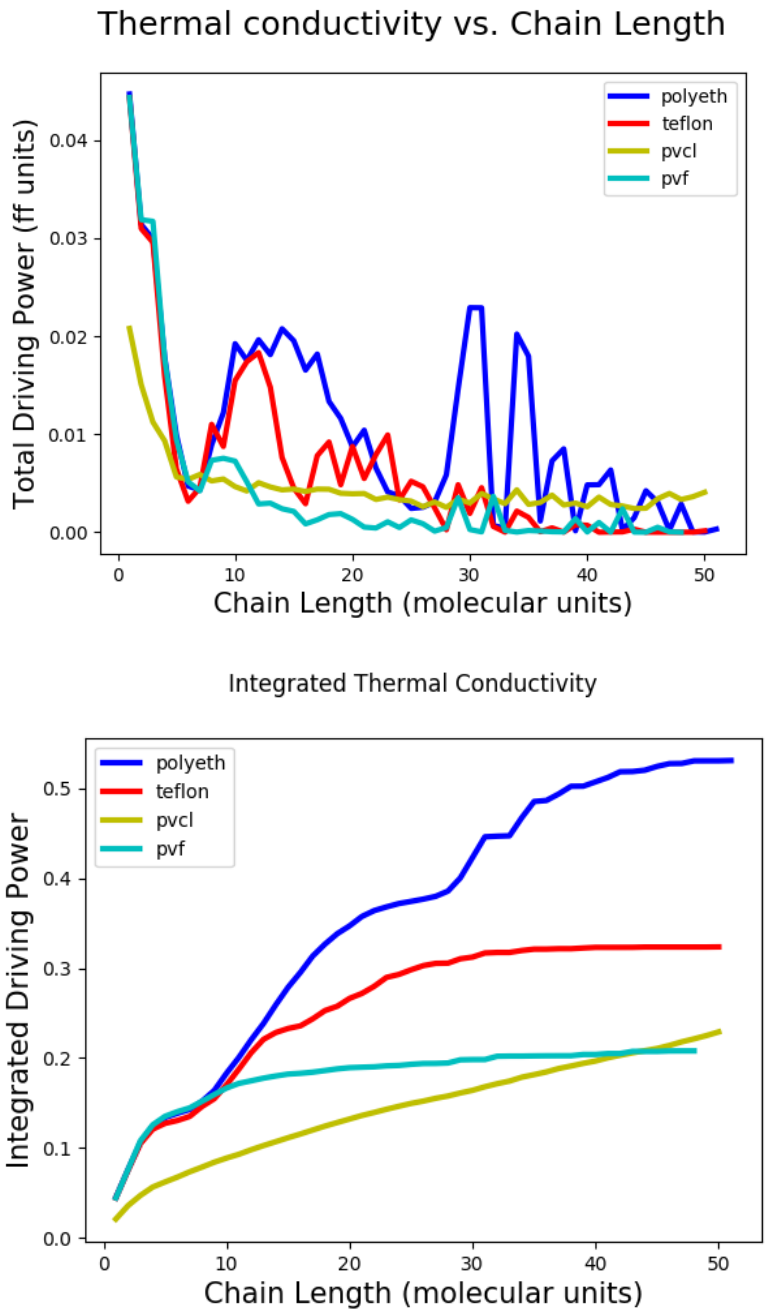

Figure 46: Plots showing Alex Kerr's Green's function method results, with thermal conductivity vs. chain length on the top and its integral on the bottom.

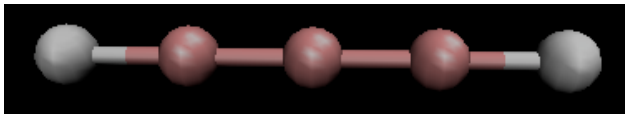

Figure 47: Example of ball & spring model used to compare my results to that of Alex Kerr's. Generated using VMD.

Chapter 6: Conclusion

In this thesis I have discussed a number of things. First I discussed the problem of interfacial, or Kapitza, resistance as well as the history, physics, and mathematics behind carbon nanotubes (CNTs). I then discussed thermal applications of CNTs and why they could be a "game-changer" in polymer research. Next I discussed phonon transport theory as well as Kapitza resistance models to give the reader a mathematical background of the phenomenon.

Next I discussed the main body of my research for this thesis; using a random walk method to estimate the thermal conductivity of end-functionalized CNT composites. In Chapter 5: Molecular Dynamics I outline the results from molecular dynamics simulations that do the same.

For my random walk project, there were a few unanswered questions. I used randomly dispersed CNTs throughout the polymer, however in higher concentrations CNTs tend to clump together or agglomerate. It would be wise to model this effect during the simulations and see how it affects the thermal conductivity. Another deficiency is using only a symmetric random walk to govern the walkers (phonons) motion throughout the polymer. Using another type of random walk to model the heat walker's motion, such as a non-Brownian model) is intriguing to research as well as important.

A Lévy flight (named after the French mathematician Paul Lévy) is another important random walk model, in which instead of Brownian motion the walkers have a step-length of a probability distribution with a substantial "tail" (non-Brownian motion) [61]. It follows the following piecewise equations ("survivor" function):

$$Prob(U > u) = \begin{cases} 1 & : u < 1 \\ u^{-d} & : u \geq 1 \end{cases} \quad \textbf{(96)}$$

where Prob is the probability of observing the walk step size U larger than u and D is related to the fractal dimension (a measure of how detailed a particular pattern changes with the scale it is measured with [62]). This statement holds for other similar functions that model random walks.

Far away from the center of the distribution it becomes stable (generalized Central Limit Theorem), allowing many physical models, such as my model, to incorporate this type of random walk.

For my molecular dynamics project, much was left open-ended. Ideally my MD results should have matched Alex Kerr's results; however time constraints proved that to be a challenge.

The numerical analysis of Chapter 3 can be supplemented by a theoretical analysis. For example, the effective thermal conductivity should be compared with the Maxwell formula for the effective properties of composites. It may also be possible to model the nano-composite as a two-step random walk, with small random steps representing the standard diffusion, & occasional large steps representing the CNTs. Finally, it would be useful to determine the "correlation volume" of the functionalized ends of the CNTs. This analysis assumes it is small – on the order of a CNT diameter. This can be tested using the molecular dynamics (MD) techniques of Chapter 5: Molecular Dynamics. If the correlation volume is large the simulation of Chapter 3: Phonon transport theory/Kapitza resistance models would have to be revisited.

References

[1] Wikipedia, “Order and disorder.” .

[2] Wikipedia, “Carbon Nanotube.” [Online]. Available: https://en.wikipedia.org/wiki/Carbon_nanotube.

[3] J. Che, T. Cagin, and W. A. Goddard III, “Thermal conductivity of carbon nanotubes,” *Nanotechnology*, vol. 11, no. 2, p. 65, 2000.

[4] E. S. Choi *et al.*, “Enhancement of thermal and electrical properties of carbon nanotube polymer composites by magnetic field processing,” *J. Appl. Phys.*, vol. 94, no. 9, pp. 6034–6039, 2003.

[5] SES research, “NANOTUBES.” [Online]. Available: https://www.sesres.com/nanotubes.asp.

[6] NIST, “TYPES OF NANOTUBES.” [Online]. Available: http://www.ncnr.nist.gov/staff/taner/nanotube/types.html.

[7] P. L. Kapitza, “Heat transfer and superfluidity of helium II,” *Phys. Rev.*, vol. 60, no. 4, pp. 354–355, 1941.

[8] L. De Bellis, P. E. Phelan, and R. S. Prasher, “Variations of Acoustic and Diffuse Mismatch Models in Predicting Thermal-Boundary Resistance,” *J. Thermophys. Heat Transf.*, vol. 14, no. 2, pp. 144–150, 2000.

[9] Wikipedia, “Carbon nanotube field-effect transistor.” [Online]. Available: https://en.wikipedia.org/wiki/Carbon_nanotube_field-effect_transistor.

[10] K. M. Razeeb, E. Dalton, G. L. W. Cross, and A. J. Robinson, “Present and future thermal interface materials for electronic devices,” *Int. Mater. Rev.*, vol. 0, no. 0, pp. 1–21, 2017.

[11] G. Gonzalez *et al.*, “Development of 3D printable formulations containing CNT with enhanced electrical properties,” *Polym. (United Kingdom)*, vol. 109, pp. 246–253, 2017.

[12] H. Chen, H. Wei, M. Chen, F. Meng, H. Li, and Q. Li, “Enhancing the effectiveness of silicone thermal grease by the addition of functionalized carbon nanotubes,” *Appl. Surf. Sci.*, vol. 283, pp. 525–531, 2013.

[13] Wikipedia, “Boltzmann equation.” [Online]. Available: https://en.wikipedia.org/wiki/Boltzmann_equation.

[14] S. Harris, *An Introduction to the Theory of the Boltzmann Equation*. Dover, 2004.

[15] Wikipedia, “Thermal diffusivity.” [Online]. Available: https://en.wikipedia.org/wiki/Thermal_diffusivity.

[16] Wikipedia, “Graphene.” [Online]. Available: https://en.wikipedia.org/wiki/Graphene.

[17] S. Berber, Y.-K. Kwon, and D. Tomanek, “Unusually high thermal conductivity of carbon nanotubes,” *Phys. Rev. Lett.*, vol. 84, no. 20, pp. 4613–4616, 2000.

[18] J. Hone, “Quantized Phonon Spectrum of Single-Wall Carbon Nanotubes,” *Science (80-.).*, vol. 289, no. 5485, pp. 1730–1733, 2000.

[19] C. Dekker, “Conference on Disorder and Interaction Quantum Hall and Mesoscopic Systems,” 1998.

[20] V. Popov and P. Lambin, *Carbon Nanotubes: From Basic Research to Nanotechnology*, vol. 53, no. 9. 2006.

[21] M. Pakkhesal and R. Ghayour, “Electronic Band Structure of Carbon Nanotubes in Equilibrium and None-Equilibrium Regimes,” in *Electronic Properties of Carbon Nanotubes*, J. M. Marulanda, Ed. InTech, 2011, pp. 391–408.
[22] E. Pop, “Summary of boundary resistance,” *ECE 598EP: Hot Chips class notes*, 2008. [Online]. Available: http://poplab.stanford.edu/files/ece598/L12L13_TBR_Thermometry.pdf.
[23] Wikipedia, “Debye model.” [Online]. Available: https://en.wikipedia.org/wiki/Debye_model.
[24] HyperPhysics, “Law of Dulong and Petit.” [Online]. Available: http://hyperphysics.phy-astr.gsu.edu/hbase/thermo/Dulong.html.
[25] Wikipedia, “Bulk Modulus.” [Online]. Available: https://en.wikipedia.org/wiki/Bulk_modulus.
[26] J. M. Ziman, *Electrons and Phonons*. Oxford: Clarendom Press, 1960.
[27] A. C. Sparavigna and A. Carolina, “The Boltzmann Equation Of Phonon Thermal Transport Solved In the Relaxation Time Approximation – I – Theory,” *Mech. Mater. Sci. Engi-neering J.*, 2016.
[28] A. A. Maznev and O. B. Wright, “Demystifying umklapp vs normal scattering in lattice thermal conductivity,” *Am. J. Phys.*, vol. 82, no. 11, pp. 1062–1066, 2014.
[29] D. Schwen and Wikipedia, “Umklapp scattering.” [Online]. Available: https://en.wikipedia.org/wiki/Umklapp_scattering.
[30] a. Ward and D. a. Broido, “Intrinsic phonon relaxation times from first-principles studies of the thermal conductivities of Si and Ge,” *Phys. Rev. B*, vol. 81, no. 8, p. 85205, 2010.
[31] J. Callaway, “Low-temperature lattice thermal conductivity,” *Phys. Rev.*, vol. 122, no. 3, pp. 787–790, 1961.
[32] W. Dreyer and H. Struchtrup, “Heat pulse experiments revisited,” *Contin. Mech. Thermodyn.*, vol. 5, no. 1, pp. 3–50, 1993.
[33] I. M. Khalatnikov, “No Title,” *Zh. Eksp. Teor. Fiz. (in Russ.*, no. 22, p. 687, 1952.
[34] E. T. Swartz and R. O. Pohl, “Thermal boundary resistance,” *Rev. Mod. Phys.*, vol. 61, no. 3, pp. 605–668, 1989.
[35] P. E. Phelan, “Application of Diffuse Mismatch Theory to the Prediction of Thermal Boundary Resistance in Thin-Film High-Tc Superconductors,” *J. Heat Transfer*, vol. 120, no. 1, p. 37, 1998.
[36] A. Majumdar, “Effect of Interfacial Roughness on Phonon Radiative Heat-Conduction,” *J. Heat Transf. Asme*, vol. 113, no. 4, pp. 797–805, 2007.
[37] A. C. Anderson, J. I. Connolly, and J. C. Wheatley, “Thermal boundary resistance between solids and helium below 1K,” *Phys. Rev.*, vol. 135, no. 4A, 1964.
[38] A. R. Boccaccini, J. Cho, J. A. Roether, B. J. C. Thomas, E. Jane Minay, and M. S. P. Shaffer, “Electrophoretic deposition of carbon nanotubes,” *Carbon N. Y.*, vol. 44, no. 15, pp. 3149–3160, 2006.
[39] W. B. Choi *et al.*, “Electrophoresis deposition of carbon nanotubes for triode-type field emission display,” *Appl. Phys. Lett.*, vol. 78, no. 11, pp. 1547–1549, 2001.
[40] W. Francisco, F. V. Ferreira, E. V. Ferreira, L. de S. Cividanes, A. dos R.

Coutinho, and G. P. Thim, “Functionalization of multi-walled carbon nanotube and mechanical property of epoxy-based nanocomposite,” *J. Aerosp. Technol. Manag.*, vol. 7, no. 3, pp. 289–293, 2015.
[41] P. Bonnet, D. Sireude, B. Garnier, and O. Chauvet, “Thermal properties and percolation in carbon nanotube-polymer composites,” *Appl. Phys. Lett.*, vol. 91, no. 20, pp. 2005–2008, 2007.
[42] M. B. Bryning, D. E. Milkie, M. F. Islam, J. M. Kikkawa, and A. G. Yodh, “Thermal conductivity and interfacial resistance in single-wall carbon nanotube epoxy composites,” *Appl. Phys. Lett.*, vol. 87, no. 16, pp. 1–3, 2005.
[43] K. M. Lee, L. Li, and L. Dai, “Asymmetric end-functionalization of multi-walled carbon nanotubes,” *J. Am. Chem. Soc.*, vol. 127, no. 12, pp. 4122–4123, 2005.
[44] M. Mir, E. Ebrahimnia-Bajestan, H. Niazmand, and M. Mir, “A novel approach for determining thermal properties of single-walled carbon nanotubes,” *Comput. Mater. Sci.*, vol. 63, pp. 52–57, 2012.
[45] K. Bi, Y. Chen, J. Yang, Y. Wang, and M. Chen, “Molecular dynamics simulation of thermal conductivity of single-wall carbon nanotubes,” *Phys. Lett. A*, vol. 350, no. 1–2, pp. 150–153, 2006.
[46] S. Rouhi, Y. Alizadeh, and R. Ansari, “On the interfacial characteristics of polyethylene/single-walled carbon nanotubes using molecular dynamics simulations,” *Appl. Surf. Sci.*, vol. 292, pp. 958–970, 2014.
[47] Q. Li, G. He, R. Zhao, and Y. Li, “Investigation of the influence factors of polyethylene molecule encapsulated into carbon nanotubes by molecular dynamics simulation,” *Appl. Surf. Sci.*, vol. 257, no. 23, pp. 10022–10030, 2011.
[48] H. M. Duong, D. V. Papavassiliou, L. L. Lee, and K. J. Mullen, “Random walks in nanotube composites: Improved algorithms and the role of thermal boundary resistance,” *Appl. Phys. Lett.*, vol. 87, no. 1, 2005.
[49] K. G. S. H. Gunawardana, K. Mullen, and D. V Papavassiliou, “Efficient Random Walk Algorithm for Simulating Thermal Transport in Composites With High Conductivity Contrast,” *East*, p. 16, 2009.
[50] H. M. Duong, D. V Papavassiliou, K. J. Mullen, and S. Maruyama, “Computational modeling of the thermal conductivity of single-walled carbon nanotube-polymer composites.,” *Nanotechnology*, vol. 19, no. 6, p. 65702, 2008.
[51] M. Allen, “Introduction to molecular dynamics simulation,” *Comput. Soft Matter From Synth. Polym. to …*, vol. 23, no. 2, pp. 1–28, 2004.
[52] GROMACS, “GROMACS Reference Manual 2016.3,” 2016.
[53] “LAMMPS documentation: run_style.” [Online]. Available: http://lammps.sandia.gov/doc/run_style.html.
[54] “LAMMPS documentation: fix nvt command.” [Online]. Available: http://lammps.sandia.gov/doc/fix_nh.html.
[55] Wikipedia, “Green-Kubo relations.” [Online]. Available: https://en.wikipedia.org/wiki/Green–Kubo_relations.
[56] G. A. Pavliotis, “Linear Response Theory, The Green-Kubo formula and Langevin Dynamics,” 2015. [Online]. Available: http://www.complexfluids.ethz.ch/images/iwnet2015/lecture-03-pavliotis.pdf.
[57] L. Landau, “Chapter 4. The Green-Kubo Relations,” *Zhurnal Eksp. i Teor. Fiz.*, pp. 1–21, 1937.

[58] LAMMPS, “compute heat/flux command.” [Online]. Available: http://lammps.sandia.gov/doc/compute_heat_flux.html.
[59] A. Ait Moussa and K. Mullen, “Using normal modes to calculate and optimize thermal conductivity in functionalized macromolecules,” *Phys. Rev. E - Stat. Nonlinear, Soft Matter Phys.*, vol. 83, no. 5, pp. 1–8, 2011.
[60] Wikipedia, “Autocorrelation.” [Online]. Available: https://en.wikipedia.org/wiki/Autocorrelation.
[61] Wikipedia, “Lévy flight.” [Online]. Available: https://en.wikipedia.org/wiki/Lévy_flight.
[62] M. L. Lapidus and M. van Frankenhuijsen, “Fractal Geometry, Complex Dimensions and Zeta Functions: Geometry and Spectra of Fractal Strings,” *Springer Monogr. Math.*, vol. 166, 2013.

Appendix A: Random walk simulation rules

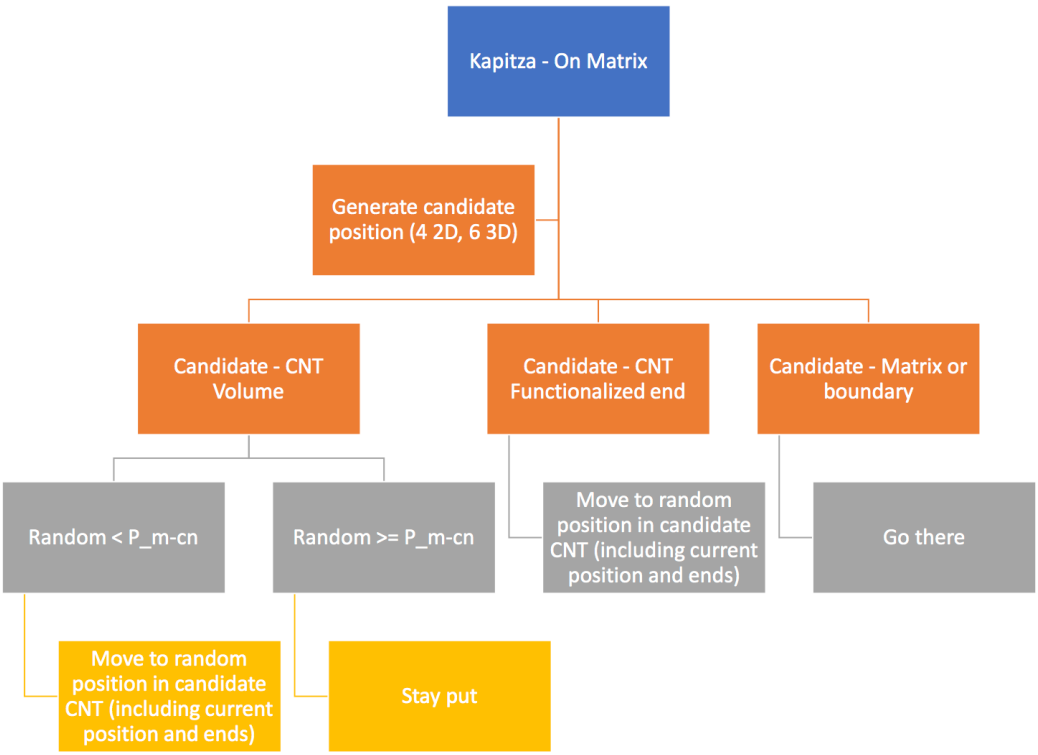

Figure 48: Walker rules for Kapitza model – on matrix elements.

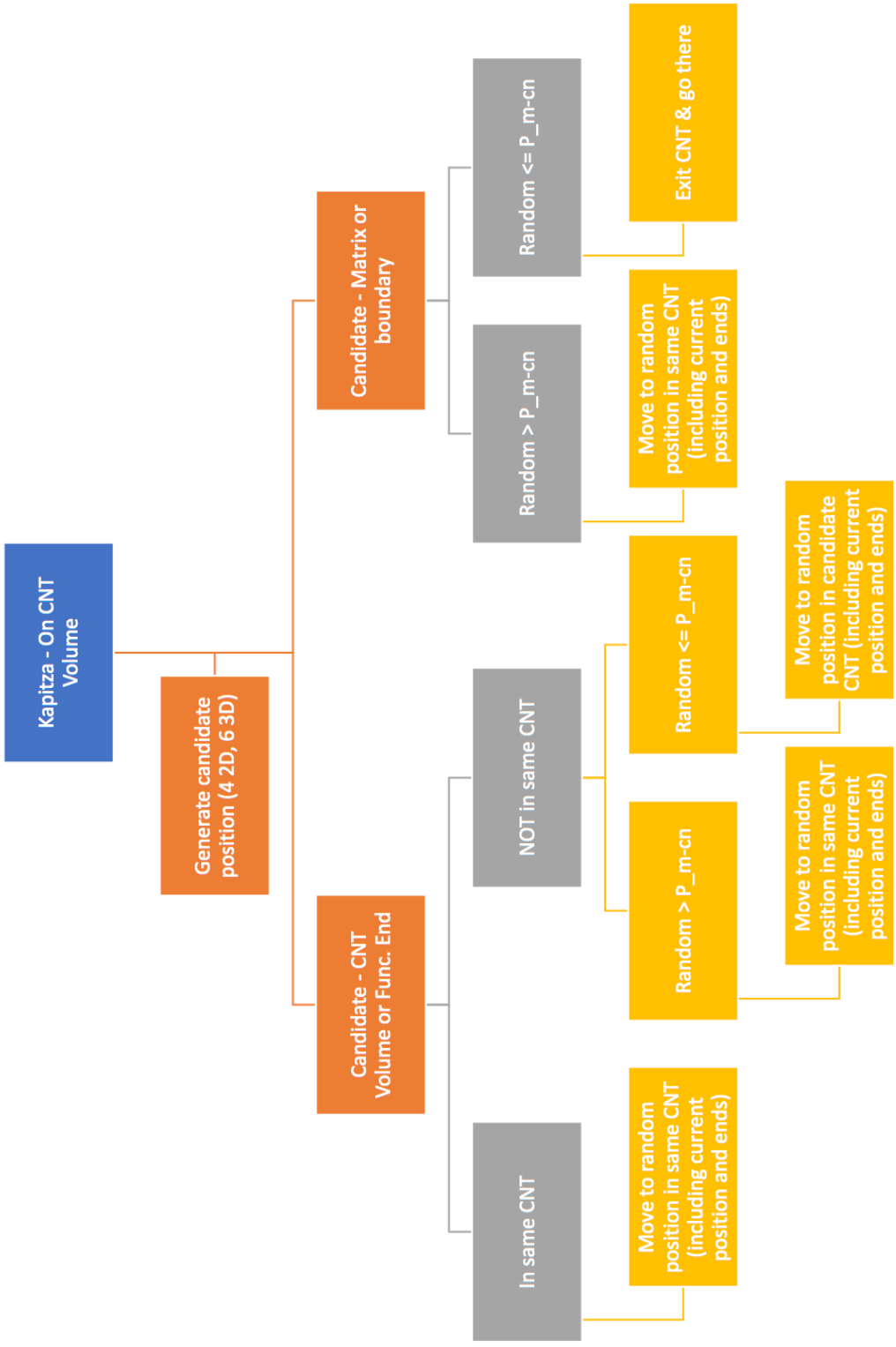

Figure 49: Walker rules for Kapitza model – on CNT volume.

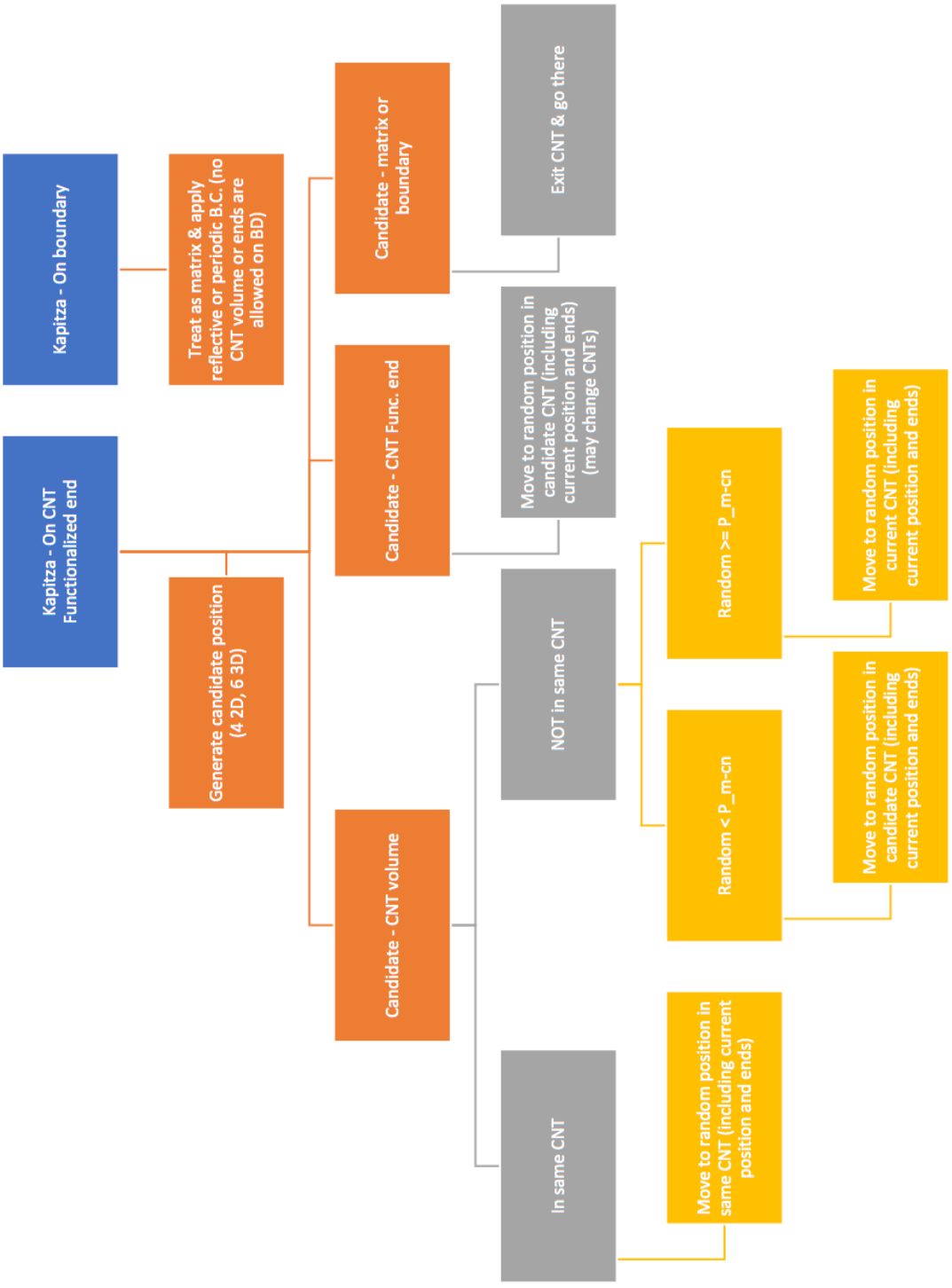

Figure 50: Walker rules for Kapitza – on CNT functionalized end and Kapitza – on boundary of simulation.

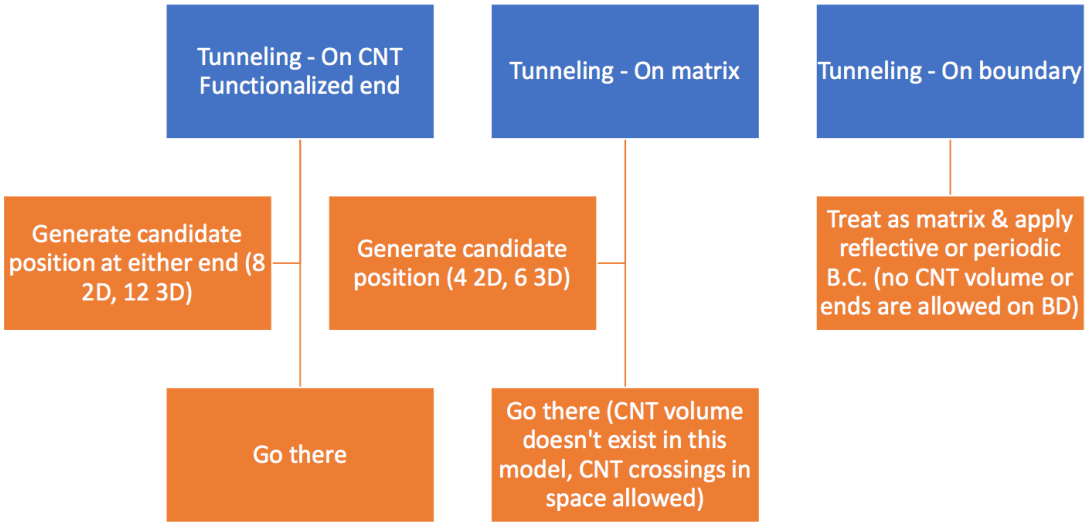

Figure 51: Walker rules for all tunneling models.

Appendix B: 2D random walk results

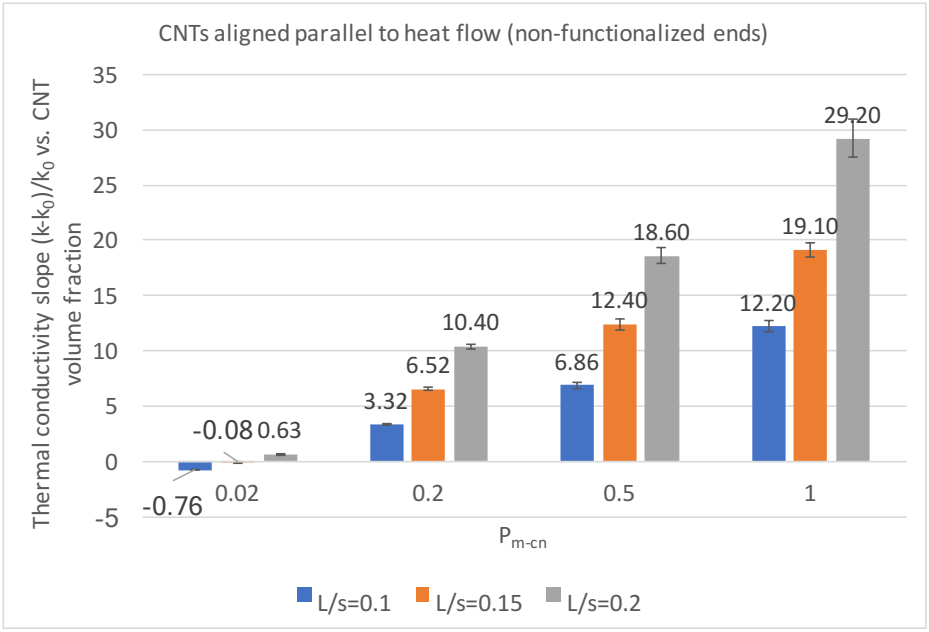

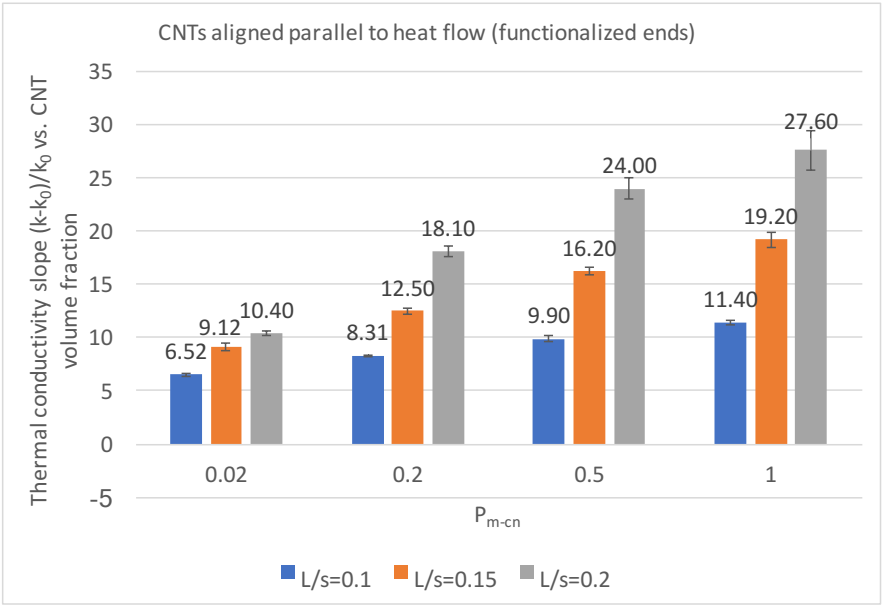

Figure 52: Slopes of linear fits to thermal conductivity (dimensionless) vs. CNT filling fraction plots for CNTs aligned parallel to heat flow (horizontal WRT x-axis) for $P_{m\text{-}cn}$=0.02, 0.2, 0.5, 1.0 and tube lengths 10, 15, 20 in a 100X100 2D simulation box. Top-CNTs without end functionalization. Bottom-CNTs with end functionalization.

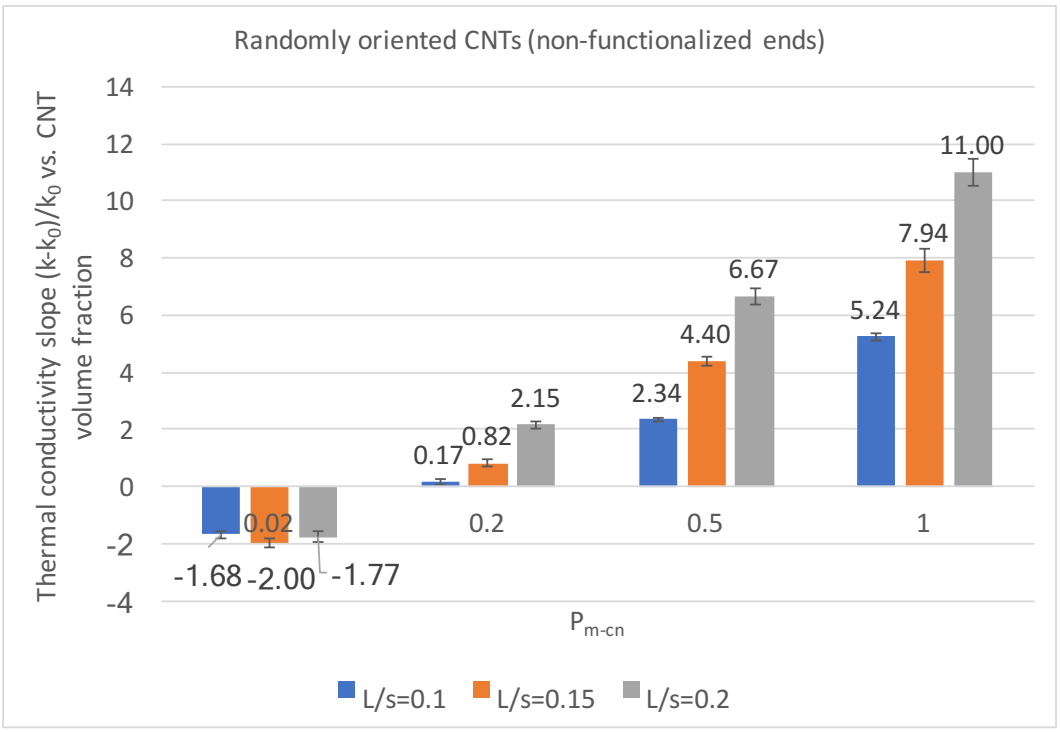

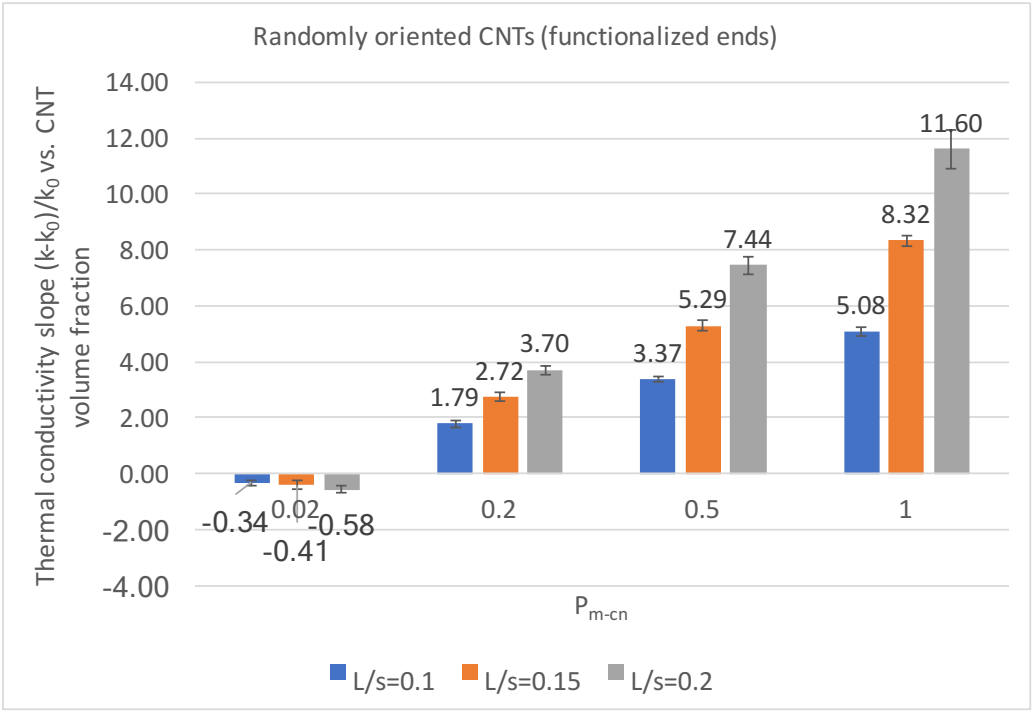

Figure 53: Slopes of linear fits to thermal conductivity (dimensionless) vs. CNT filling fraction plots for CNTs aligned randomly to heat flow for P_{m-cn}=0.02, 0.2, 0.5, 1.0 and tube lengths 10, 15, 20 in a 100X100 2D simulation box. Top-CNTs without end functionalization. Bottom-CNTs with end functionalization.

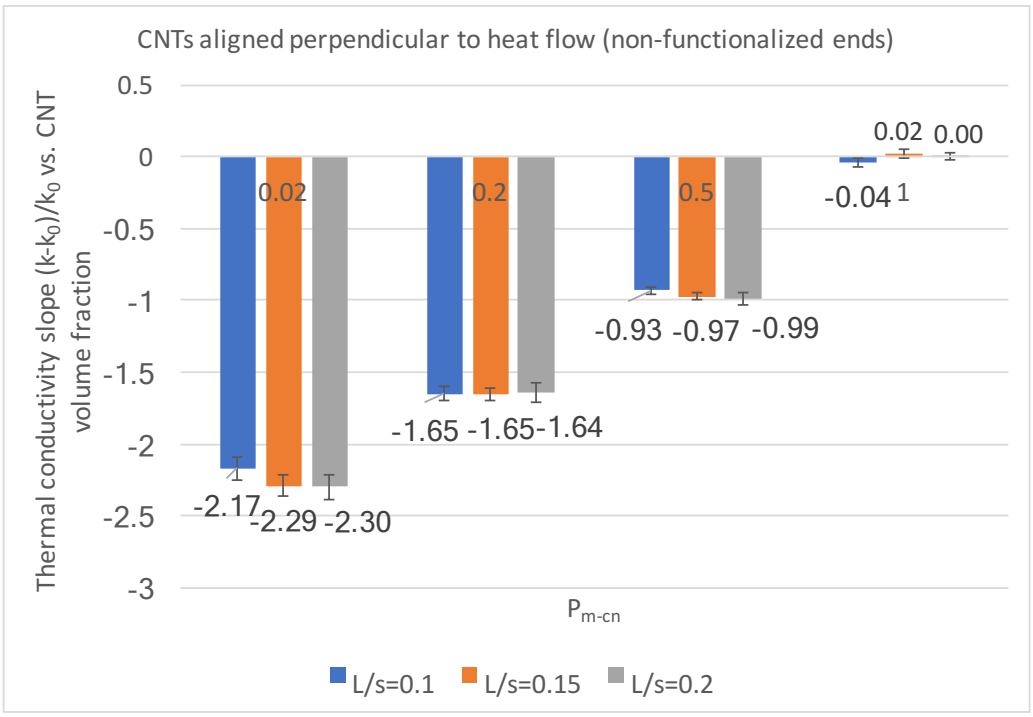

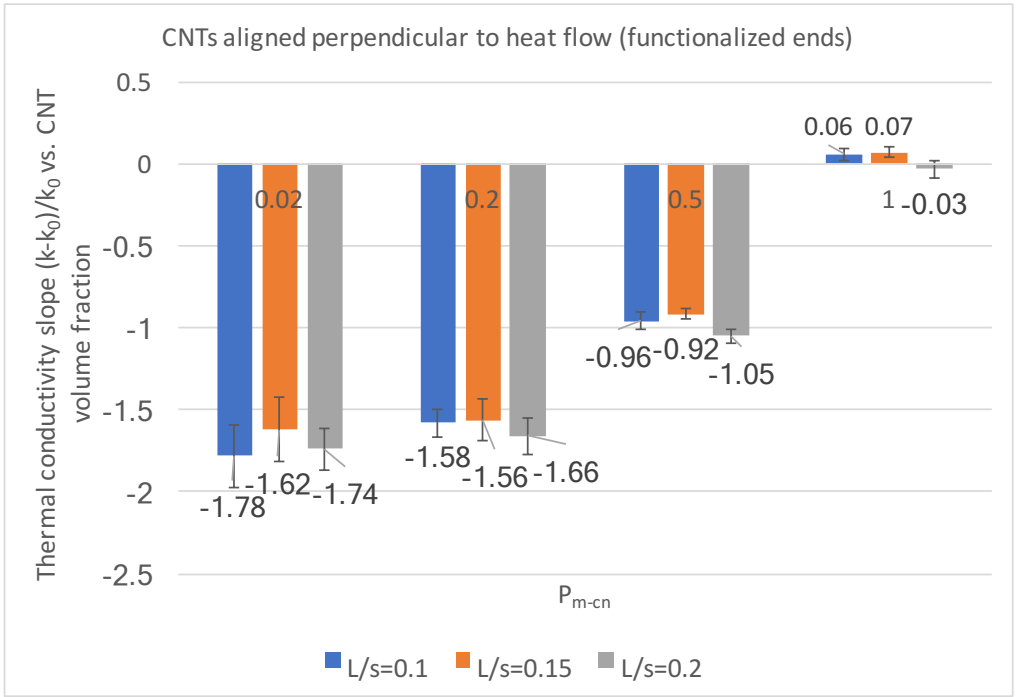

Figure 54: Slopes of linear fits to thermal conductivity (dimensionless) vs. CNT filling fraction plots for CNTs aligned perpendicular to heat flow (vertical WRT x-axis) for P_{m-cn}=0.02, 0.2, 0.5, 1.0 and tube lengths 10, 15, 20 in a 100X100 2D simulation box (Kapitza models). Top-CNTs without end functionalization. Bottom-CNTs with end functionalization.

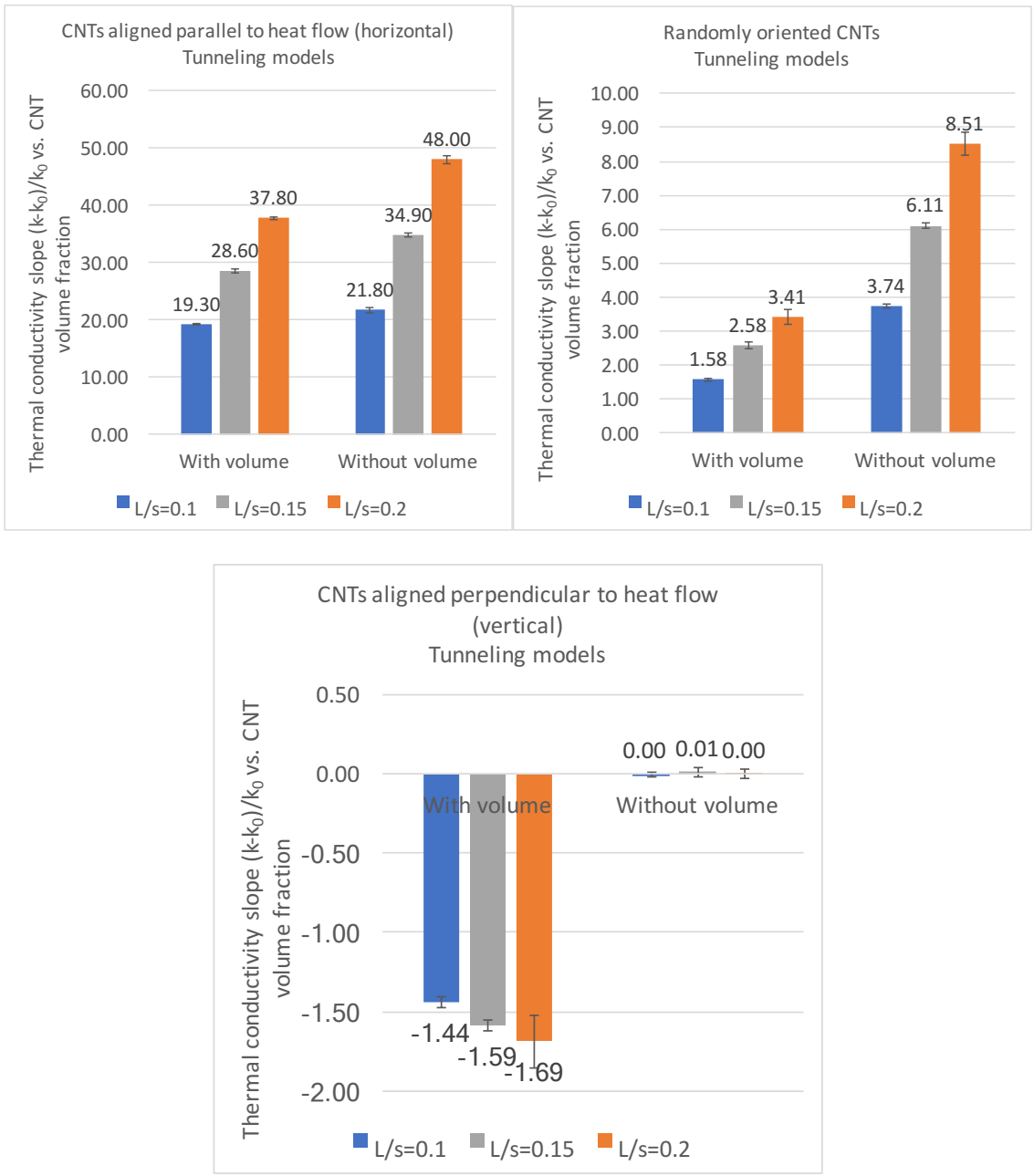

Figure 55: Slopes of linear fits to thermal conductivity (dimensionless) vs. CNT filling fraction plots for all orientations and tube lengths 10, 15, 20 in a 100x100 2D simulation box (tunneling models).

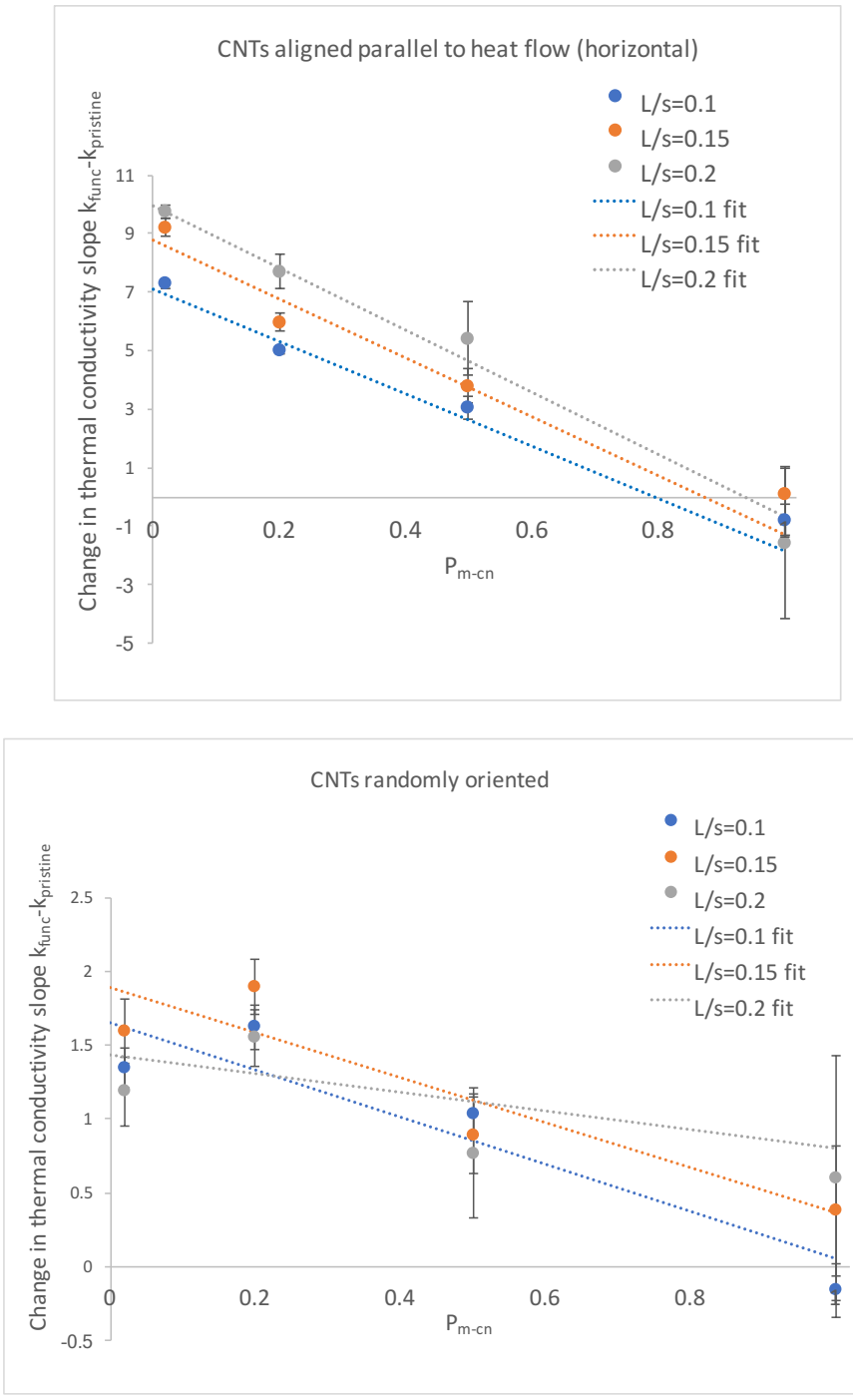

Figure 56: Change in thermal conductivity slope after CNT end functionalization vs. probability for a phonon (walker) to enter a CNT (P_{m-cn}), for tube lengths 10, 15, 20 in a 100X100 2D simulation box. Above-CNTs aligned parallel to the heat flow (horizontal WRT x-axis). Below-CNTs aligned randomly to the heat flow.

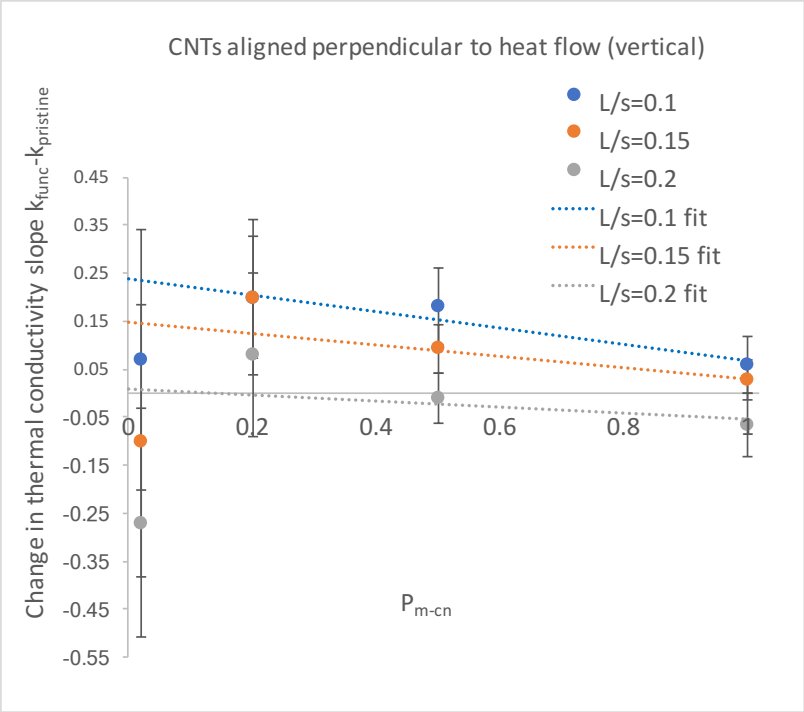

Figure 57: Change in thermal conductivity slope after CNT end functionalization vs. probability for a phonon (walker) to enter a CNT (P_{m-cn}), for tube lengths 10, 15, 20 in a 100X100 2D simulation box. CNTs aligned perpendicular to the heat flow (vertical WRT x-axis).

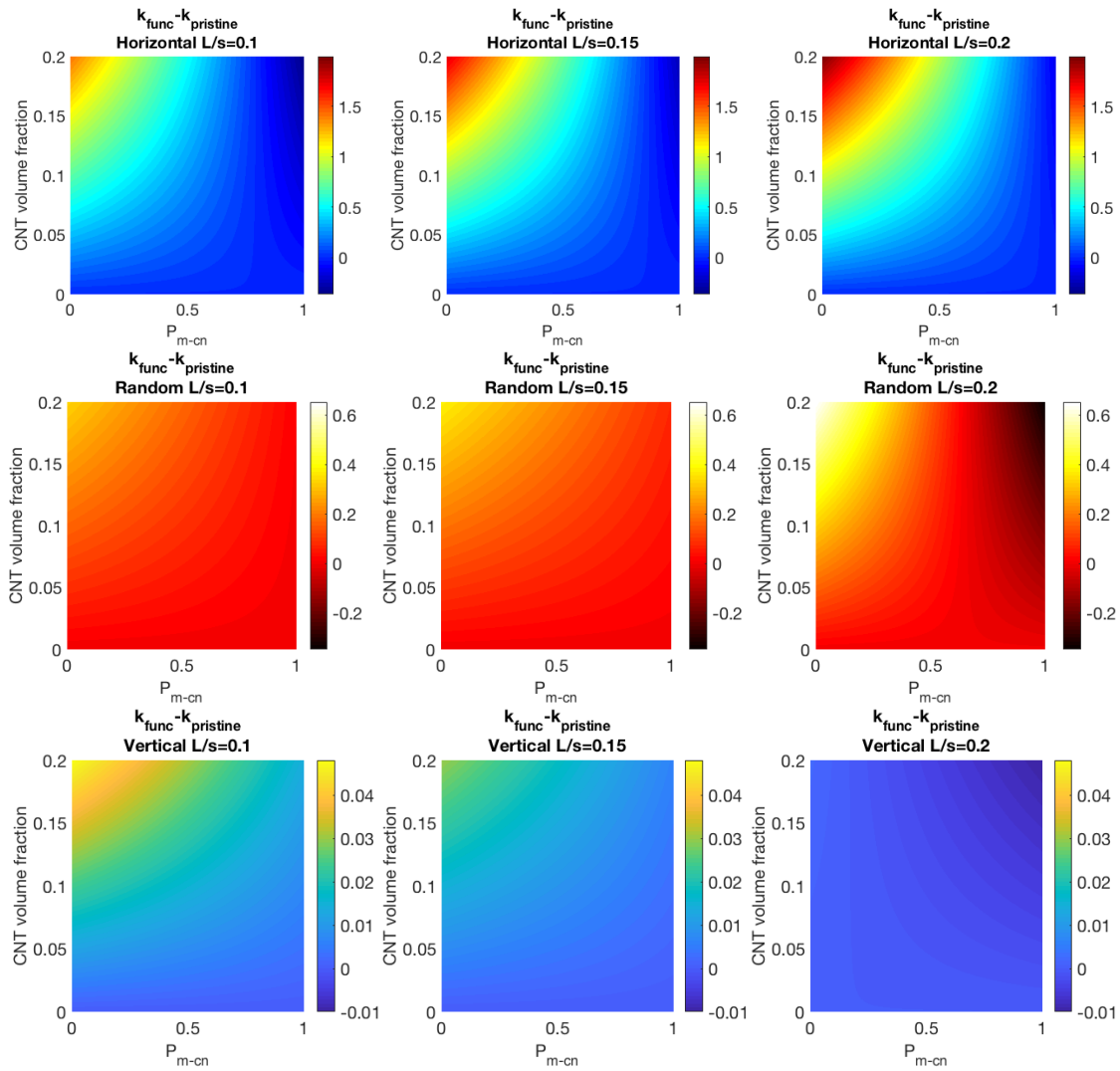

Figure 58: Colormaps for horizontal, random, and vertical orientations in 2D depecting the improvement of thermal conductivity after end functionalization as the color. Shown on the x-axis is P_{m-cn}, and shown on the y-axis is the CNT volume fraction. These follow what we would expect; if a CNT has a high Kapitza resistance, functionalizing the ends will help a lot, but if a CNT has a low Kapitza resistance, it will not help.

Appendix C: LAMMPS thermal conductivity code example

```
# Green-Kubo method via compute heat/flux and fix ave/correlate
# LAMMPS script
# Tim Burt 9/28/2017

# settings

#variable       name equal X
variable        rho equal 0.6
variable        t equal 7.5
variable        rc equal 5.0

variable    p equal 400     # correlation length of J output  (make sure heat flux ACF
dissipates to zero within this window)
variable    s equal 10     # sample interval
variable    d equal $p*$s   # dump interval

variable    equil_timesteps equal 2500000
variable    thermo_timesteps equal 50000000

# convert from LAMMPS real units to SI

variable    kB equal 1.3806504e-23    # [J/K] Boltzmann
variable    kCal2J equal 4186.0/6.02214e23
variable    A2m equal 1.0e-10
variable    fs2s equal 1.0e-15
variable    convert equal ${kCal2J}*${kCal2J}/${fs2s}/${A2m}
variable    dt equal 0.01
variable    V equal 1.0

units real

log          dummy5.log

# setup problem

atom_style      angle  # bonds angles only
bond_style      harmonic
angle_style     harmonic
dimension       3
atom_modify     sort 1000 2.0
read_data       dummy10.lammps
group           1 molecule 1
group           2 molecule 2
#group          3 molecule 3
```

```
velocity        all create $t ${random} mom yes rot yes dist uniform units box loop all

neighbor        2.0 bin
neigh_modify    delay 0 every 1

pair_style       none
#pair_style     lj/cut ${rc}
#pair_coeff     * * 1E-4 1.52

fix             1 all momentum 1 linear 1 1 1 angular

# energy minimize structure

min_style       cg
dump            m1 all movie 100 simulation.m4v type type zoom 2.5 adiam 0.2 size
1280 720
#dump                   m0 all image 1000 pic.*.png type type zoom 4 size 1280 720
minimize        1.0e-4 1.0e-6 1000 10000

# 1st equilibration run

fix             2 all nvt temp $t $t ${dt}
thermo          100
dump            positions all xyz 100 step1_nvt.xyz
run_style       verlet
timestep        ${dt}

run             ${equil_timesteps}

velocity        all scale $t

unfix           2

# thermal conductivity calculation

reset_timestep  0

compute         myKE 2 ke/atom
compute         myPE 2 pe/atom
compute         myStress 2 stress/atom NULL virial
compute         flux 2 heat/flux myKE myPE myStress
variable        Jx equal c_flux[1]/$V
variable        Jy equal c_flux[2]/$V
variable        Jz equal c_flux[3]/$V
```

```
fix             3 all nve
fix            JJ 2 ave/correlate $s $p $d &
              c_flux[1] c_flux[2] c_flux[3] type auto &
                file dummy5.heatflux ave running

#variable      scale equal $s*dt/$t/$t/$V
variable       scale equal ${convert}/${kB}/$t/$t/$V*$s*${dt}
#variable        scale equal (${convert})/(${kB}*$V*$s*dt)
variable       k11 equal trap(f_JJ[3])*${scale}
variable       k22 equal trap(f_JJ[4])*${scale}
variable       k33 equal trap(f_JJ[5])*${scale}

thermo         $d
thermo_style    custom step temp v_Jx v_Jy v_Jz v_k11 v_k22 v_k33

run            ${thermo_timesteps}

variable       k equal (v_k11+v_k22+v_k33)/3.0
variable          ndens equal count(all)/$V
print             "average conductivity: $k[W/mK] @ $t K, ${ndens} /A^3"
print             "$k" file dummy5.k screen yes
```

Appendix D: Experimental apparatuses used to measure k

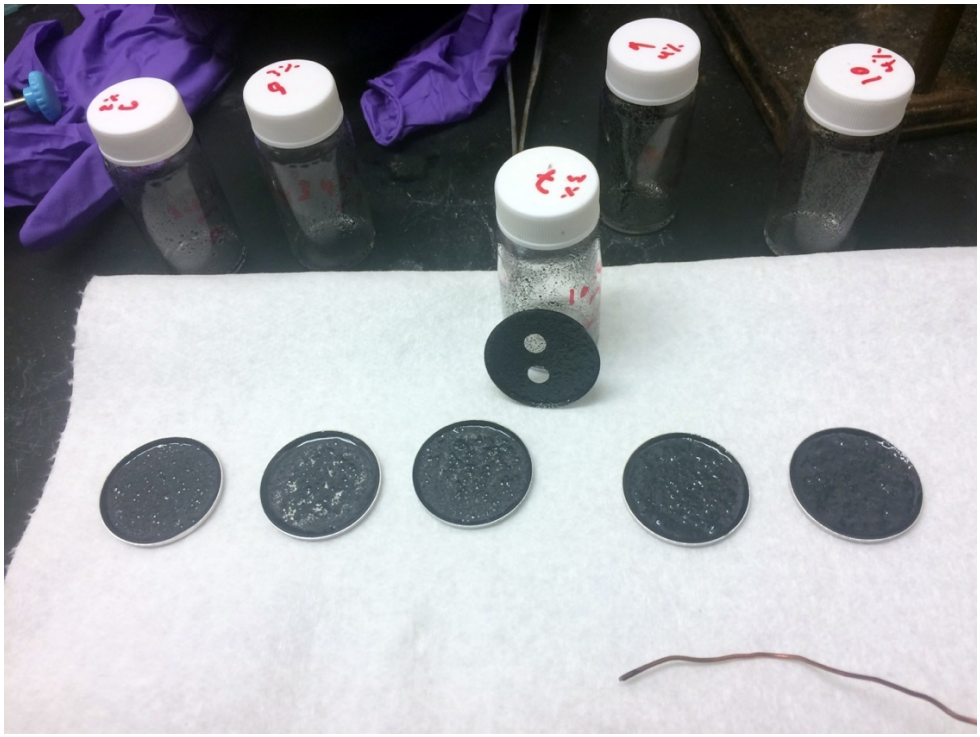

Figure 59: Image of baked CNT polymer composites synthesized in the Glatzhofer lab, showing dye punchouts from one of the samples which are then placed in the differential scanning calorimeter (DSC) to experimentally measure k. CNTs are known to agglomerate or clump together as the CNT volume fraction increases in a sample, and the method used in the Glatzhofer lab disperses the CNTs well within the polymer matrix to avoid this.

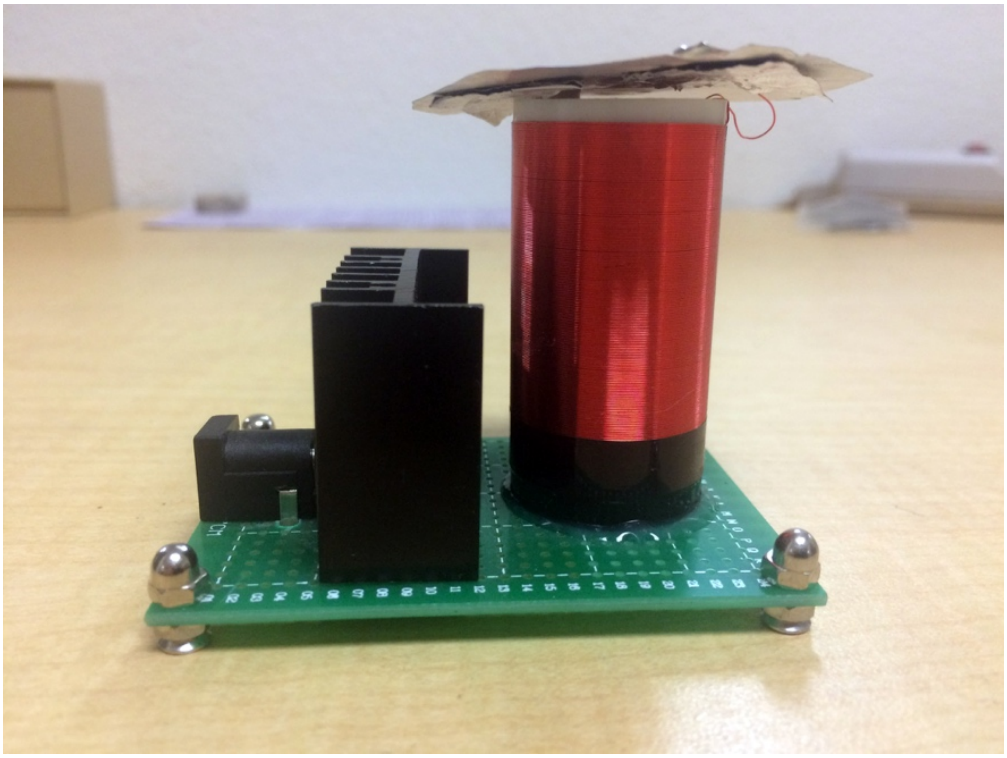

Figure 60: Image of a copper-wound coil (electromagnet) created in the Glatzhofer lab which creates an electric field which may then be applied to a CNT polymer composite (which is still viscous) in order to align the CNTs (electrophoresis).

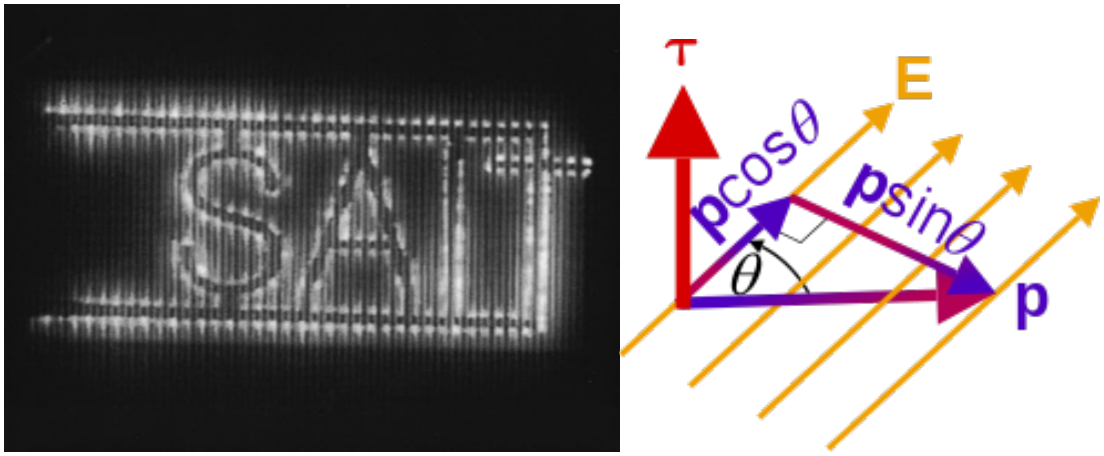

Figure 61: Left-emission image of CNTs aligned and deposited using electrophoresis [39]**. Right-Drawing of vectors relating momentum and electric field to torque.**

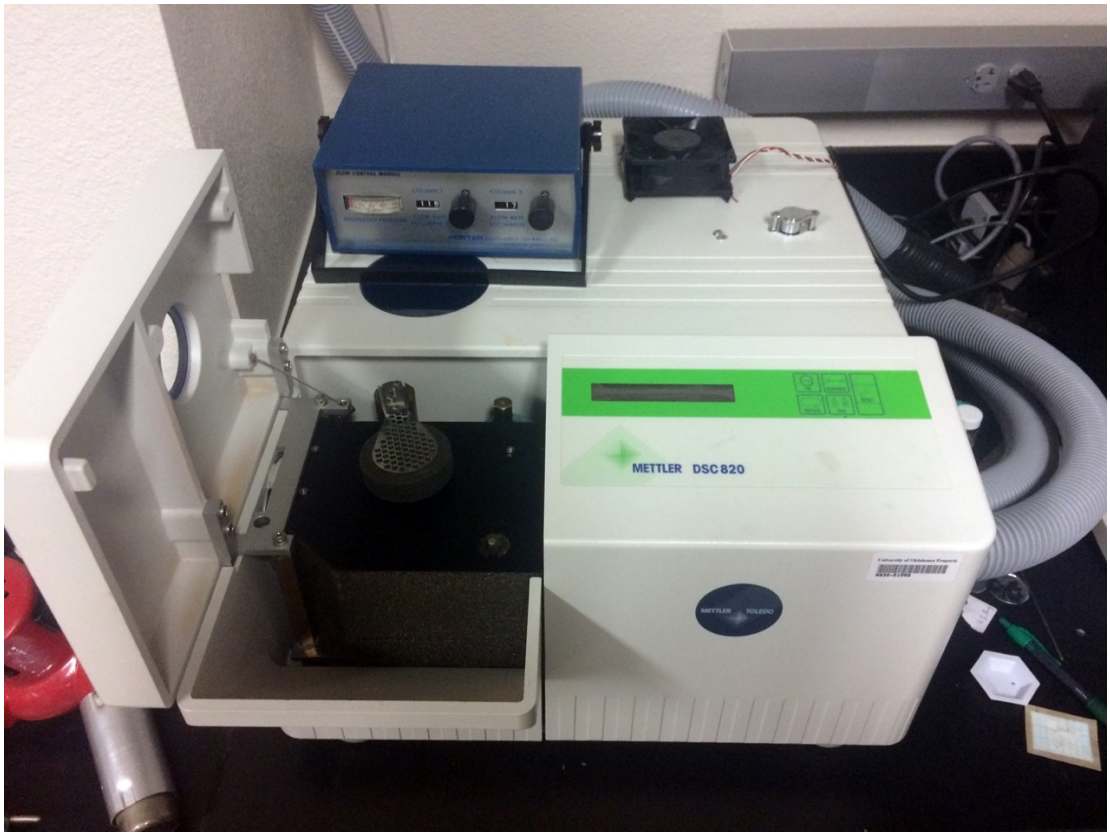

Figure 62: Image of the differential scanning calorimeter used in the Glatzhofer lab to experientially measure the thermal conductivity of the CNT-polymer composites (Mettler DSC830).